Proceedings

of the Second Seminar on

THE MECHANICS OF MULTIFUNCTIONAL MATERIALS

J. Schröder, D.C. Lupascu, M.-A. Keip, D. Brands (Eds.)

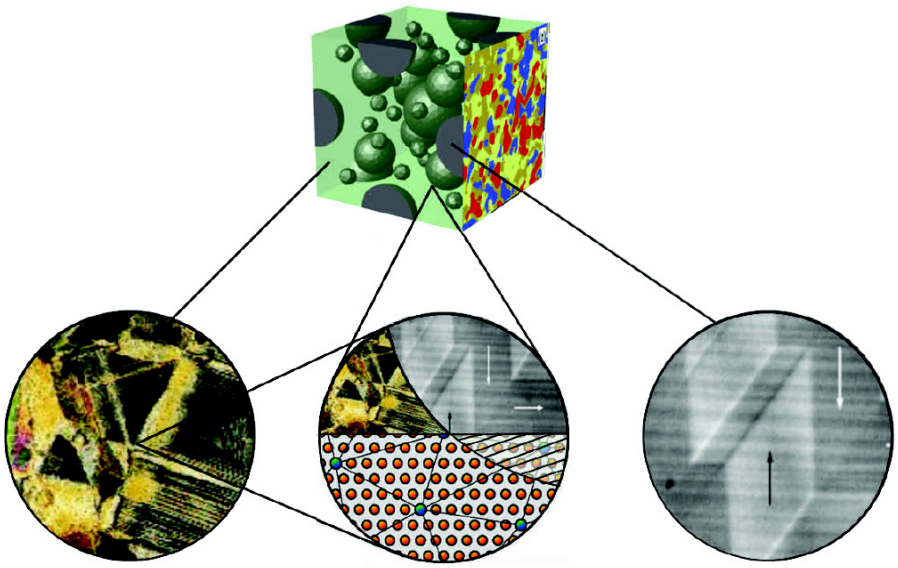

Physikzentrum Bad Honnef

May 5 - 9, 2014

Report No. 12
Institute of Mechanics
Department of Civil Engineering
Faculty of Engineering
University of Duisburg-Essen

Editors:

Prof. Dr.-Ing. habil. Jörg Schröder
University of Duisburg-Essen
Faculty of Engineering
Department of Civil Engineering
Institute of Mechanics
Universitätsstr. 15
D-45141 Essen

Prof. Dr. rer. nat. Doru C. Lupascu
University of Duisburg-Essen
Faculty of Engineering
Institute for Materials Science and Center for Nanoengineering Duisburg-Essen (CENIDE)
Universitätsstr. 15
D-45141 Essen

Jun.-Prof. Dr.-Ing. Marc-André Keip
University of Stuttgart
Institute of Applied Mechanics (CE), Chair I
Pfaffenwaldring 7
D-70569 Stuttgart

Dr.-Ing. Dominik Brands
University of Duisburg-Essen
Faculty of Engineering
Department of Civil Engineering
Institute of Mechanics
Universitätsstr. 15
D-45141 Essen

ISBN-10 3-9809679-8-0
ISBN-13 978-3-9809679-8-3
EAN 9783980967983

Preface

Multifunctional materials are key ingredients in many modern technical devices ranging from consumer market items to applications in high-end equipment for automobile, aircraft, spacecraft, and information technology. The understanding and development of multifunctional materials is based on a comprehensive understanding of both the experimental and the theoretical details of these materials. Thus, we are delighted to welcome in this seminar national and international experts in continuum mechanics, applied mathematics, and materials science. The topics addressed in the lectures will span modeling, simulation, and experiments in fields ranging from ferroelectrics and -magnets, multiferroics and multiferroic composites, magnetorheological and electroactive elastomers, lithium ion batteries, to polymer blends, alloys, and porous media. This great range of inherently allied fields allows for a broad and deep insight into the scientific activities and advancements of all the reasearch disciplines involved.
Thus, we are happy to welcome more than 50 attendees to this seminar which takes place at the *Physikzentrum* Bad Honnef. The *Physikzentrum* has been serving as the main meeting point of the German Physical Society since 1976. Located close to Germany's oldest nature preserve with beautiful views on the Rhine river the place offers a perfect platform for intensive discussions. Therefore, we hope that the seminar will be successful in fostering greater interactions among all the scientific disciplines involved as well as between young and established researchers.
The proceedings at hand provide the extended abstracts of 33 lectures presented at the seminar. We would like to heartily thank all authors and participants for their kind cooperation and contribution to this workshop. We wish all participants a fruitful seminar and a nice stay at the *Physikzentrum*.

Sincerely,
The organizers

Jörg Schröder,
Doru C. Lupascu,
Marc-André Keip,
Dominik Brands

Acknowledgement

The financial support through the *Deutsche Forschungsgemeinschaft* in the framework of the Research Unit 1509 “Ferroic Functional Materials – Multiscale Modeling and Experimental Characterization” is gratefully acknowledged.

Sincerely,
The organizers

Extended Abstracts

A PRECISE FORMULA FOR THE PROPAGATION SPEED OF DIFFUSIVE INTERFACES IN THE ALLEN-CAHN PHASE FIELD MODEL FOR PHASE INTERFACES IN SOLIDS.

H.-D. Alber[1]

[1] TU Darmstadt, Department of Mathematics,
Schlossgartenstr. 7, Darmstadt, Germany
e-mail: alber@mathematik.tu-darmstadt.de

Abstract.

Standard phase field models for the evolution of phase states in solids are based on the Allen-Cahn phase field equation. To model the phase evolution precisely, it is necessary to know the dependence of the propagation speeds of the phase interfaces on the stress field, on the curvature properties of the interface, on the transformation strain and on other material parameters. In multifunctional materials the propagation speed depends in addition on other physical fields. In sharp interface models the relation between the physical fields and the propagation speed of the interface is called kinetic relation.

In the talk we present a formula, which approximates the kinetic relation for the propagation speed of a level set of the order parameter modeling a diffuse interface in the Allen-Cahn phase field model for phase evolution in elastic solids. In our model the order parameter S varies between 0 and 1 and we consider the level set $S = \frac{1}{2}$. The error between the propagation speed given by the formula and the exact propagation speed can be estimated by $C\mu^2$, where μ is the width of the diffusive interface in the phase field model.

The formula is derived by construction of an asymptotic solution to the model equations.

NONLINEAR FERROELECTRIC-FERROMAGNETIC BEHAVIOR OF MULTIFERROIC COMPOSITES

A. Avakian[1], R. Gellmann[2], and A. Ricoeur[3]

[1,2,3] Institute of Mechanics, Chair of Engineering Mechanics / Continuum Mechanics, University of Kassel
Moenchebergstrae 7, 34125 Kassel, Germany
e-mail: artjom.avakian@uni-kassel.de

Abstract. *In this paper, the theoretical background of linear and nonlinear constitutive multifield behavior as well as the Finite Element implementation are presented. The developed tools enable the prediction of the electromagnetomechanical properties of materials and structures and supply useful tools for the optimization of multifunctional composites. Both linear and nonlinear magnetoelectric models are presented within the context of a Finite Element implementation. A homogenization technique is applied to describe the macroscopic behavior. Numerical examples focus on the poling process and the magnetoelectric coupling.*

1 Introduction

Multiferroic magnetoelectric materials, which simultaneously exhibit ferroelectricity and ferromagnetism, have recently stimulated a sharply increasing number of research activities. These materials are much desired, because of the presence of the interaction between electric and magnetic fields. It is important to note, that this interaction appears as a material property (*ME-effect*) and is not following from the Maxwell-equations (*EM-effect*). The coupling of magnetic and electrical fields may occur due to the physical properties of a crystal or can be artificially produced in a smart composite. The multiferroic composites, which incorporate both ferroelectric and ferromagnetic phases, typically yield much larger magnetoelectric coupling response at room temperature [4]. In composites, the ME-effect is induced by the strain field converting electrical and magnetic energies based on the piezoelectric and magnetostrictive effects.

2 Theoretical Framework

2.1 Linear magnetoelectroelastic behavior

The scalar electric and magnetic potentials are motivated from the Maxwell-equations for the electrostatical and magnetostatical cases, such that $E_i = -\varphi^{el}_{,i}$ and $H_i = -\varphi^{m}_{,i}$. With the help of these equations, the constitutive law of quasistatic magnetoelectroelasticity is formulated on the basis of the thermodynamic potential $\Psi(\varepsilon_{ij}, E_i, H_i) = (\sigma_{ij}\varepsilon_{ij} - D_i E_i - B_i H_i)/2$. The constitutive equations of linear magnetoelectroelasticity in compressed notation are then obtained as

$$\sigma_q = c_{qp}\varepsilon_p - e_{lq}E_l - q_{lq}H_l, \quad D_i = e_{ip}\varepsilon_p + \kappa_{il}E_l + g_{il}H_l, \quad B_i = q_{ip}\varepsilon_p + g_{il}E_l + \mu_{il}H_l \quad (1)$$

The application of approximate methods requires the formulation of field equations in the weak form. This formulation is obtained e.g. from the generalized Hamiltons variational prin-

ciple. In connection with the constitutive Eqs. (1) the generalized matrices of an isoparametric finite element formulation [1], [2] are derived. Based on these equations, the boundary value problem is formulated as an algebraic system of equations $[K]\{U\} = \{R\}$. Here, the generalized displacement vector $\{U\}$ and the generalized force vector $\{R\}$ incorporate displacements, electric and magnetic potentials as well as nodal forces and generalized charges: $\{\{u_i\}, \{\phi^{el}\}, \{\phi^m\}\}^T$ and $\{\{F_s\}, \{Q_s^{el}\}, \{Q_s^m\}\}^T$.

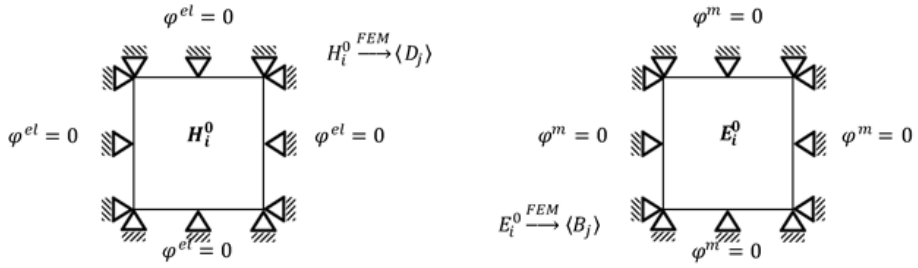

Figure 1: Boundary conditions for the calculation of the effective magnetoelectric tensor

On the macroscopic scale, the relations between the effective material tensors and the averaged fields are formulated as $\langle \Sigma \rangle = L^* \langle Z \rangle$ where Σ stands for (σ_q, D_i, B_i); L^* contains all of the material constants and Z stands for $(\varepsilon_p, E_i, H_i)$. To calculate the effective material tensors, generalized periodic boundary conditions are applied in connection with constant strain ε_{ij}^0 and constant electric and magnetic fields E_i^0, H_i^0 which are applied to an RVE: $u_i^+ - u_i^- = \varepsilon_{ij}^0 (x_i^+ - x_i^-)$, $\phi^{el+} - \phi^{el-} = -E_i^0 (x_i^+ - x_i^-)$, $\phi^{m+} - \phi^{m-} = -H_i^0 (x_i^+ - x_i^-)$. The magnetoelectric tensor can be calculated either from the ratio between the averaged electric displacement and the applied magnetic field or from the averaged magnetic induction and the applied electric field as shown in Eq. (2). The corresponding magnetoelectric constant in x_1-direction g_{11} is calculated as shown in Fig. 1.

$$g_{ij}^* = \left. \frac{\langle D_j \rangle}{H_i^0} \right|_{\varepsilon_p, E_j = \text{const}} = \left. \frac{\langle B_i \rangle}{E_j^0} \right|_{\varepsilon_p, H_i = \text{const}} . \tag{2}$$

2.2 Nonlinear magneto-ferroelectric constitutive behavior

Ferroelectric materials exhibit nonlinear remanent effects, significantly influencing the properties of multifunctional composites. Simulation of the poling process inevitably requires nonlinear constitutive modeling. As a simplified approach, the magnetostrictive phase is assumed to behave linearly, whereas the piezoelectric phase exhibits a ferroelectric nonlinearity and linear diamagnetic properties. In ferroelectric material, the strain ε_p and electric displacement D_i are additively decomposed into reversible and irreversible parts: $\varepsilon_p = \varepsilon_p^r + \varepsilon_p^{irr}$, $D_i = D_i^r + P_i^{irr}$. The irreversible parts are due to polarization switching on the microlevel or domain wall motion on the mesoscopic level. The magneto-ferroelectric model is based on a thermodynamical potential:

$$\Psi(\varepsilon_p, E_i, H_i) = \frac{1}{2} c_{qp} \varepsilon_q \varepsilon_p - e_{ip} \varepsilon_p E_i - \frac{1}{2} \kappa_{ij} E_i E_j - \frac{1}{2} \mu_{ij} H_i H_j - c_{qp} \varepsilon_q^{irr} \varepsilon_p + e_{ip} \varepsilon_p^{irr} E_i - P_i^{irr} E_i \tag{3}$$

The corresponding constitutive equations are then obtained as

$$\sigma_q = c_{qp} (\varepsilon_p - \varepsilon_p^{irr}) - e_{lq} E_l, \quad D_i = e_{ip} (\varepsilon_p - \varepsilon_p^{irr}) + \kappa_{il} E_l + P_i^{irr}, \quad B_i = \mu_{il} H_l. \tag{4}$$

On the macroscopic scale, the changes in irreversible strain and polarization evolve as:

$$\dot{\varepsilon}_{ij}^{irr} = \sum_{n=1}^{4} \overset{(n)}{\varepsilon}{}^{sp}_{ij} \dot{\nu}_n, \qquad \dot{P}_i^{irr} = \sum_{n=1}^{4} \Delta \overset{(n)}{P}{}^{sp}_{i} \dot{\nu}_n. \tag{5}$$

They are described by internal variables ν_n, for plain problems associated with the four possible orientations of unit cells in a grain [5]. Here $\overset{(n)}{\varepsilon}{}^{sp}_{ij}$ and $\Delta \overset{(n)}{P}{}^{sp}_{i}$ represent the spontaneous strain and change of spontaneous polarization for the domain n, respectively. The evolution of the internal variables ν_n within a domain structure is controlled by an energetic criterion.

The corresponding stiffness matrices as well as the mechanical, electric and magnetic nodal loads are derived in analogy to the approach outlined in section 2.1. The following additional terms

$$\{F_e\} = \int_V [B_u]^T [c]\{\varepsilon^{irr}\} dV, \qquad \{Q_e^{el}\} = \int_V [B_{el}]^T ([e]\{\varepsilon^{irr}\} - \{P^{irr}\}) dV, \tag{6}$$

account for the nonlinear contributions. The terms $[c]\{\varepsilon^{irr}\}$ and $([e]\{\varepsilon^{irr}\} - \{P^{irr}\})$ in the above equation have to be interpreted as intrinsic stresses and polarization due to domain wall motion.

3 Results

3.1 Perfectly poled linear piezoelectric-magnetostrictive composite

A magnetoelectric particle composite of 20% $CoFe_2O_4$ and 80% $BaTiO_3$ is considered. It has a piezoelectric matrix ($BaTiO_3$) with embedded magnetostrictive particles ($CoFe_2O_4$) and is perfectly poled in the x_1 direction. The model has been generated automatically, accounting for a statistical distribution of particle location, size and ellipticity. The effective magnetoelectric constant in x_1-direction is obtained as the arithmetical average of the two approaches shown in Eq. (2) yielding $g_{11}^* = 70.3E-12$[Ns/VC]. Comparing the numerical result with an experimental value [3] $g_{11}^* = 4.4E-12$[Ns/VC] the large difference is obvious. This is due to the assumption of a perfect poling state which cannot be achieved experimentally. A reasonable comparison of theoretical and experimental data is only possible, if the nonlinear poling process is included in the numerical simulation.

3.2 Diamagnetic-ferroelectric simulation of the poling process

A composite of $CoFe_2O_4$ particles embedded into a $BaTiO_3$ matrix is investigated. The local polarization and maximum principle stresses are illustrated on the left and right hand sides of Fig. 2. The electric loads were applied incrementally up to $E_2 = 5E_c$ followed by an incremental unloading process. As shown in the left figure, the local polarization is not perfectly aligned with the electric poling field as assumed in linear calculations. It is worth noting that for a magneto-electric composite a pre-magnetization is performed in addition to the electric polarization. It is expected that the local magnetization will not be aligned parallel to external magnetic field, similar to local polarization. Further, the magnetization will influence the parallel alignment of the local electric polarization which was an assumption in section 3.1. We therefore conclude that the assumed parallel alignment of the local polarization and the local magnetization of a linear magneto-electroelastic composite is not realistic.

As shown in the right figure, there is a considerable mechanical stress going along with the poling procedure leading to maximum principle stresses of up to 44 MPa after unloading. The

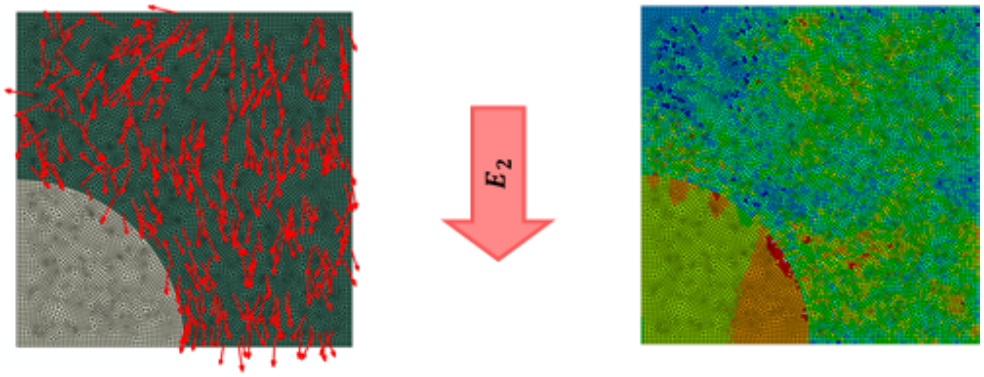

Figure 2: Results of the simulation of the polarization process for a magneto-electric particle composite (matrix: $BaTiO_3$, particles: $CoFe_2O_4$), left: local polarization, right: maximum principle stress

maximal stress of approximately 57 MPa is observed at $E_2 = 5E_c$. This will certainly lead to the initiation of many microcracks. The maximum principle stress at different load states is observed at interfaces between matrix and inclusion. On his part, this phenomenon influences the effective material parameters of the composite, which has not yet been considered in the calculations.

4 Conclusions

A subroutine USER-Element (UEL) for linear magneto-electro-elastic behavior has been developed and implemented in a commercial FEM software ABAQUS. Homogenization procedures are applied to calculate the effective magneto-electric coupling. Further, nonlinear magneto-ferroelectric behavior is included into the model. It is shown that the poling process has a significant influence on the coupling behavior of a ME-composite. Mechanical stresses during the ferroelectric poling process are obtained from the simulations indicating crack formation at the interfaces between matrix and particles. The final goal of the investigations is to optimize multiferroic composites with respect to functionality and strength.

REFERENCES

[1] A. Avakian, A. Ricoeur. Enhancement of magnetoelectric coupling in multiferroic composites via FEM simulation, Proceedings in *Advances in Structural Engineering and Mechanics*, 2013.

[2] A. Avakian, A. Ricoeur. Linear and nonlinear Finite Element modeling of coupled electro-magneto-mechanical multifield problems, in *Proc.Appl.Math.Mech.*, 13 (1), 203-204, 2013.

[3] M. Etier, Y. Gao, V. V. Shvartsman, D. C. Lupascu, J. Landers and H. Wende. Magnetoelectric properties of $02.CoFe_2O_4$ - $0.8BaTiO_3$ composite prepared by organic method, *Joint 21st IEEE ISAF/11th IEEE ECAPD/IEEE PFM (ISAF/ ECAPD/PFM)*, 1-4, 2012.

[4] M. Fiebig. Revival of the magnetoelectric effect, *J. Phys. D: Appl. Phys.*, 38 (8), R123-R152, 2005.

[5] J. E. Huber, N. A. Fleck, C. M. Landis and R. M. McMeeking. A constitutive model for ferroelectric polycrystals, *J. Mech. Phys. Solids*. 47 (8), 1663-1697, 1999.

MODELING OF SINGLE CRYSTAL MAGNETOSTRICTION BASED ON NUMERICAL ENERGY RELAXATION TECHNIQUES

K. Buckmann[1], B. Kiefer[1], T. Bartel[1] and A. Menzel[1,2]

[1] Institute of Mechanics, Department of Mechanical Engineering, TU Dortmund
Leonhard-Euler-Str. 5, 44227 Dortmund, Germany
e-mail: karsten.buckmann@udo.edu, bjoern.kiefer@udo.edu,
thorsten.bartel@udo.edu, andreas.menzel@udo.edu

[2] Division of Solid Mechanics, Lund University
P.O. Box 118, SE-221 00 LUND, Sweden

Abstract. *This work is concerned with the modeling of the influence of microstructure evolution on the macroscopic response of single-crystalline magnetostrictive materials based on numerical energy relaxation. As a starting point, the DeSimone and James [1] constrained theory of magnetoelasticity is reviewed and applied to the prediction of magnetic shape memory behavior under complex magnetomechanical loading. An extended modeling approach is subsequently presented in which the original constraints regarding infinite elastic and magnetocrystalline anisotropy energies are alleviated. In this case, elastic deformations and the rotations of magnetic moments away from easy axes represent additional degrees of freedom for the energy relaxation. Moreover, hysteretic effects are taken into account by reformulating the problem in form of an incremental variational minimization problem for standard dissipative materials. Representative numerical examples illustrating the improved modeling accuracy for magnetic shape memory response are presented.*

1 Motivation and Description of the Extended Modeling Concept

Giant magnetostrictives, such as Terfenol-D or Galfenol, and ferromagnetic shape memory alloys (MSMA) have received much attention due to their unique magnetomechanical coupling properties that potentially enable novel active material-based applications, e.g. as sensors, actuators, transducers or energy harvesters. The modeling of nonlinear magnetostrictive response is typically based either on phenomenological macroscale approaches, see e.g. [2–4], or alternatively on the variational theory of *micromagnetics* [5]. The latter predicts the evolution of magnetic microstructures under the influence of mechanical and magnetic fields, but requires simulations on very small time and length scales. Due to the complexity of realistic microstructures, it is then generally not feasible to simulate the response of samples of technologically-relevant size. In light of this, DeSimone and James developed the *constrained theory of magnetoelasticity* [1], which is capable of predicting many relevant features of the macroscopic magnetomechanical response, without requiring the detailed knowledge of the underlying domain structure. This micromechanically-motivated variational theory was derived from micromagnetics and is valid for phase changing materials whose free energy densities grow steeply away from its minima. The set of admissible macroscopic states can in this case be constructed through the convex combination of the local deformation and magnetization states associated

with the energy wells. For the modeling of effective single crystal MSMA response under external stress $\overline{\boldsymbol{\sigma}}$ and magnetic field $\overline{\boldsymbol{h}}$ loading, the energy relaxation problem in the context of the constrained theory then reduces to the *quadratic optimization problem* [1,6]

$$\min_{\boldsymbol{\alpha}\in\mathcal{A}} \Pi'_{av}(\boldsymbol{\alpha}) = \min_{\boldsymbol{\alpha}\in\mathcal{A}} \left\{ \frac{1}{2}\langle \boldsymbol{m}\rangle(\boldsymbol{\alpha}) \cdot \boldsymbol{D}\langle \boldsymbol{m}\rangle(\boldsymbol{\alpha}) - \overline{\boldsymbol{h}} \cdot \langle \boldsymbol{m}\rangle(\boldsymbol{\alpha}) - \overline{\boldsymbol{\sigma}} : \langle \boldsymbol{\varepsilon}\rangle(\boldsymbol{\alpha}) \right\} V \,, \tag{1}$$

in which Π'_{av} is the system energy functional, $\langle \boldsymbol{\varepsilon}\rangle$ and $\langle \boldsymbol{m}\rangle$ are the volume averaged strains and magnetization, $\boldsymbol{D}$ the shape-dependent demagnetization tensor, and V the sample volume. Here, the domain/variant volume fractions $\boldsymbol{\alpha} = [\alpha_1, \ldots, \alpha_6]^T$ are the only remaining unknowns, which are restricted to evolve within the admissible set $\mathcal{A} := \{\boldsymbol{\alpha} \,|\, \alpha_i \geq 0, \sum_{i=1}^{6} \alpha_i = 1\}$.

The presented approach builds on the *constrained theory* and aims to overcome some of its limitations, particularly that (i) dissipation is not considered, (ii) elastic strains are omitted and (iii) the magnetizations are rigidly attached to easy axes, which, as evident from experimental observations, are clearly to restrictive for the case of MSMA modeling. Limitations (ii) and (iii) are due to the assumption of the *(infinitely) high anisotropy limit*. In the first step of extending the approach, the hysteretic nature of the response is accounted for by introducing an appropriate dissipation functional in an incremental variational setting. Secondly, the infinite anisotropy constraints are removed to allow for "non-energy-well"-states with respect to local deformations and magnetization orientations. The associated incorporation of elastic strains necessitates assumptions about the total strains in each of the martensitic variants. Furthermore, a magnetocrystalline anisotropy energy contribution is added to the incremental potential, whose zeros define the easy axes. The evolution of variant strains and local magnetization orientations, that represent additional microstructural degrees of freedom, are determined via minimization of the extended incremental energy potential. In this manner, a relaxed energy density is obtained, which serves as an approximation of the mathematically and physically desired quasi-convex hull. In the results presented here, we restrict our attention to *convexification*, since it offers the possibility of accounting for multiple martensitic phases in a straightforward manner and yields numerically robust algorithms.

2 Numerical Results

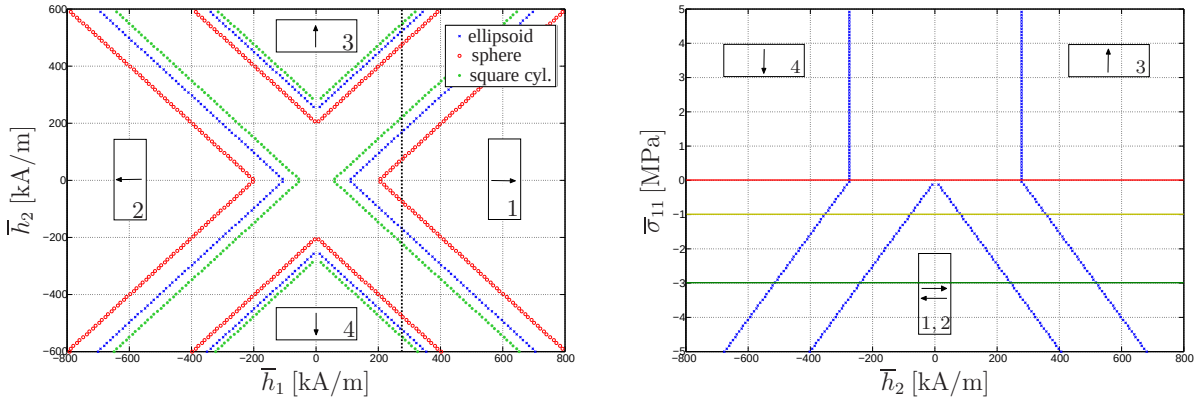

Figure 1: Phase diagrams based on the constrained theory [1,6]: a) in planar applied magnetic field $\overline{h}_1$-$\overline{h}_2$ space for three different sample geometries ; b) in applied axial stress $\overline{\sigma}_{11}$-magnetic field $\overline{h}_2$ space for a square cylinder sample. Representative loading paths under variable $\overline{h}_2$ at constant $\overline{h}_1$ and $\overline{\sigma}_{11}$, respectively, are indicated.

Figures 1–3 show preliminary results that compare predictions of magnetic field-induced martensitic variant reorientation in MSMA via the DeSimone and James theory, i.e. the con-

strained minimization problem (1), with those of the partially extended modeling approach accounting for dissipation. Figure 1 depicts phase diagrams computed on the basis of the constrained theory, see [7]. Figure 2a) presents the simulated sample geometry-dependent field-induced straining curves corresponding to the loading path indicated in Figure 1a). Figure 2 b) shows the simulation of the corresponding response curves with dissipation, for which the transformation is delayed and hysteresis is observable in the dissociation of the loading and unloading response paths. Analogous response simulations for magnetic field-induced straining at the three constant stress levels indicated in Figure 1b) are depicted in Figure 3, for the experimentally most relevant square cylinder sample geometry. It is interesting to note that at (axial) compressive stress levels of 1 and $3\ \mathrm{MPa}$ the response is characterized by a complete switching between the *stress-favored* (1,2) and *magnetic field-favored* variants (3,4). In the absence of stress, the external field stimulus can be accommodated by pure magnetic domain switching, so that the applied field does not induce variant reorientation and consequently no macroscopic straining occurs. It is also observed that the stress level-dependence of the inducible reorientation strain, which is characteristic of MSMA response, can not be predicted by the constrained theory, since the limiting mechanism of magnetization rotation is inhibited under the infinite magnetocrystalline anisotropy assumption. It will be demonstrated, that the extended model is capable of properly capturing this effect.

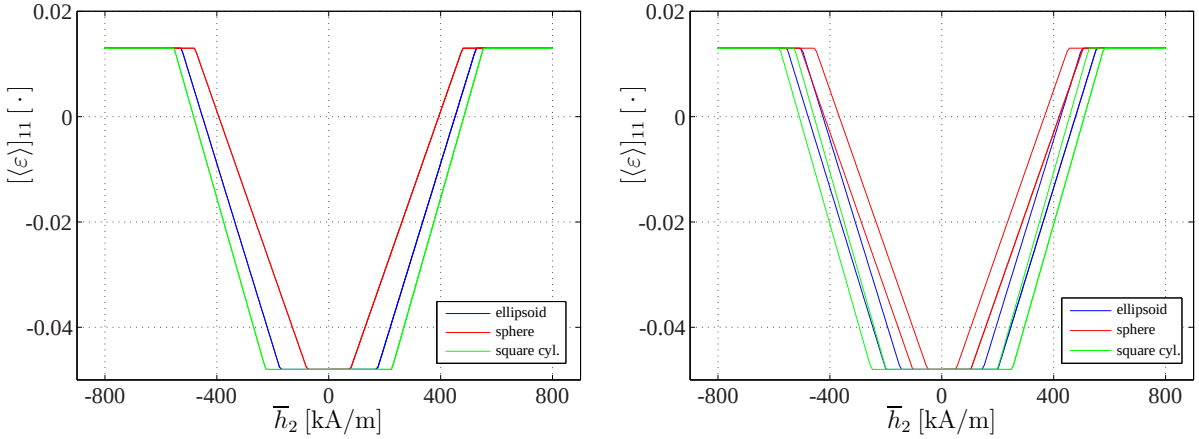

Figure 2: Prediction of field-induced straining under $\overline{h}_2$ application at constant $\overline{h}_1 = 278.0\ \mathrm{kA/m}$ (cf. Figure 1a): a) constrained theory [1,6], b) dissipation enhanced model.

3 Outlook

On-going work is concerned with extending existing numerical relaxation techniques based on a rank-one convexification with respect to first and second-order laminates, that have successfully been employed in the context of conventional shape memory response [8–10], to the magnetomechanically-coupled case.

REFERENCES

[1] A. DeSimone, R. D. James, A constrained theory of magnetoelasticity, *Journal of Mechanics and Physics of Solids*, 50(2):283–320, 2002.

[2] B. Kiefer, D. C. Lagoudas, Magnetic field-induced martensitic variant reorientation in magnetic shape memory alloys, *Philosophical Magazine*, 85(33-35):4289–4329, 2005.

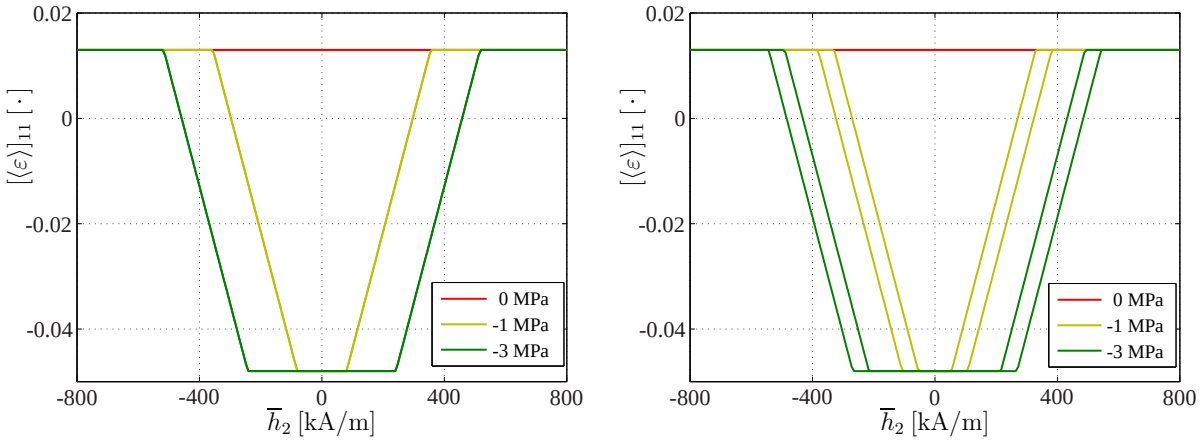

Figure 3: Prediction of field-induced straining under $\overline{h}_2$ application at three different levels of applied stress $\overline{\sigma}_{11}$ (cf. Figure 1b): a) constrained theory [1,6], b) dissipation enhanced model.

[3] B. Kiefer, D. C. Lagoudas, Modeling the coupled strain and magnetization response of magnetic shape memory alloys under magnetomechanical loading, *Journal of Intelligent Material Systems and Structures*, 20(2):143–170, 2009.

[4] C. Miehe, B. Kiefer, D. Rosato, An incremental variational formulation of dissipative magnetostriction at the macroscopic continuum level, *International Journal of Solids and Structures*, 48(13):1846–1866, 2011.

[5] W. F. Brown, Jr., *Magnetoelastic interactions*, Springer-Verlag, *Tracts in Natural Philosophy 9*, 1966.

[6] A. DeSimone, Coarse-grained models of materials with non-convex free-energy: Two case studies, *Computer Methods in Applied Mechanics and Engineering*, 193:5129–5142, 2004.

[7] L. Sprave, R. Schulte, *Implementation of a FE-based algorithm for the computation of energy minimizing microstructures in magnetostrictive materials*. Project report (supervised by B. Kiefer and A. Menzel), Institute of Mechanics, TU Dortmund, February 2013.

[8] T. Bartel, K. Hackl, A micromechanical model for martensitic phase-transformations in shape-memory alloys based on energy-relaxation, *Zeitschrift für Angewandte Mathematik und Mechanik*, 89:792–809, 2009.

[9] T. Bartel, A. Menzel, B. Svendsen, Thermodynamic and relaxation-based modeling of the interaction, *Journal of the Mechanics and Physics of Solids*, 59(5):1004–1019, 2011.

[10] T. Bartel, K. Buckmann, B. Kiefer, A. Menzel, An advanced energy relaxation scheme for the modeling of displacive phase transformations,*Proceedings of ASME-SMASIS 2013*, paper 3041, 2013.

FREE ENERGY MODELS FOR FERROELECTRIC MATERIALS WITH APPLICATION TO RATE-DEPENDENT SWITCHING

D. K. Dusthakar[1], B. Svendsen[2], and A. Menzel[1,3]

[1] Institute of Mechanics, Department of Mechanical Enginnering, TU Dortmund
Leonhard-Euler-Strasse 5, 44227 Dortmund, Germany
e-mail: dinesh.dusthakar@tu-dortmund.de
e-mail: andreas.menzel@udo.edu

[2] Chair of Material Mechanics, RWTH Aachen University
Schinkel strasse 2, 52062 Aachen, Germany
e-mail: bob.svendsen@rwth-aachen.de

[3] Division of solid mechanics, Lund university
P.O. Box 118, SE-221 00 Lund, Sweden
e-mail: andreas.menzel@solid.lth.se

Abstract. *The purpose of the work is the thermodynamic modeling of the energetics and kinetics of ferroelectric materials. The physical model formulation is carried out in the framework of continuum thermodynamics for quasi-static electromechanical processes. Building on previous work, this framework is used to formulate different models for the free energy and dissipation potential. The corresponding initial boundary-value problems are formulated with the help of rate-variational methods. This approach is then applied in particular to model the evolution of the domain microstructure and rate-dependent switching behavior in such materials.*

1 Introduction

A number of modeling approaches have been proposed for the material behavior of, and the evolution of the strain-polarization domain microstructure in, ferroelectric materials. In particular, these include models focusing on the material behavior and evolution of the strain-polarization domain microstructure; the latter include Landau-Devonshire-type phase-field-based approaches e.g., [1, 2, 6] and multi-rank-laminate-based ones e.g., [7, 8]. Building on this previous work, the current work focuses on the formulation of models for the energetics and kinetics of ferroelectric materials and their application to the modeling of the behavior of such systems including for example rate-dependent switching.

2 Model formulation

Consider a ferroelectric single-crystal occupying the spatial configuration $\mathcal{B}$ with boundary $\partial\mathcal{B}$ containing a microstructure consisting of strain-polarization domains separated by a network S of domain walls. Given that the materials of interest are generally ceramics or ceramic-like, a geometric linear model formulation is justified. For simplicity, free charges, electrostatic forces, and defects, are neglected, and the temperature is assumed constant. In this context, the energetics of the material are modeled by a free energy density ψ, and the kinetics by a dissipation potential χ. Two types of models for these are considered here. The first is based on the

phenomenological approach of [5] in which $\psi(\boldsymbol{\varepsilon}, \boldsymbol{E}, \boldsymbol{P})$ and $\chi(\dot{\boldsymbol{P}})$ hold. Here, $\boldsymbol{\varepsilon} := [\nabla \boldsymbol{u}]^{\mathrm{sym}}$ is the strain, $\boldsymbol{u}$ is the displacement, $\boldsymbol{E} := -\nabla\phi$ is the electric field, ϕ is the electrostatic potential, and $\boldsymbol{P}$ is the polarization. The second type is based on multi-rank laminate approach of [7] in which $\psi(\boldsymbol{\varepsilon}, \boldsymbol{E}, \boldsymbol{P}, \boldsymbol{\mu})$ and $\chi(\dot{\boldsymbol{\mu}})$ hold, where $\boldsymbol{\mu}$ is the array of laminate volume fractions in the variants. In this context, two models for the free energy are formulated; the first is based on volume-averaged material properties e.g., [7, 8], and the second on volume-averaged energy (current work).

3 Variational principle for initial-boundary-value problem

Given such physical model formulations, one can formulate initial boundary-value problems for the displacement $\boldsymbol{u}$ and electrostatic potential ϕ fields of the material subject to history-dependent, rate-dependent processes. To this end, it proves useful to work with rate-variational methods e.g., [5, 9]. The corresponding variational principle is based on a rate functional R and corresponding bulk density $r = \zeta + \chi$ determined by energy storage rate density $\zeta \equiv \dot{\psi}$ and dissipation potential χ. This goes beyond existing purely-energetic variational principles for ferroelectrics e.g., [4, 7] in that both energetics and kinetics are accounted for in the variational principle. The stationarity conditions of R with respect to $\mathcal{B}$, $\partial\mathcal{B}$ and S then yield the field relations, jump and boundary conditions of the model. In particular, this approach is applied to the modeling of domain microstructure evolution and rate-dependent switching. Examples will be given.

REFERENCES

[1] S. Choudhury, Y. L. Li, C. E. Krill III, and L.-Q. Chen. Phase-field simulation of polarization switching and domain evolution in ferroelectric polycrystals, *Acta Materialia*, 53: 1415–1426, 2005.

[2] M. Kamlah, A. C. Liskowsky, R. M. McMeeking, and H. Balke. Finite element simulation of a polycrystalline ferrorelectric based on a multidomain single crystal switching model, *International Journal of Solids and Structures*, 42: 2949–2964, 2005.

[3] J. Y. Li, and D. Li. On ferroelectric crystals with engineered domain configurations, *Journal of the Mechanics and Physics of Solids*, 52: 1719–1742, 2004.

[4] R. M. McMeeking, C. M. Landis, and S. M. A. Jimenez. A principle of virtual work for combined electrostatics and mechanical loading of materials, *Internaltional Journal of Non-Linear Mechanics*, 42: 831–838, 2007.

[5] C. Miehe, and D. Rosato. A rate-dependent incremental variational formulation of ferroelectricity, *International Journal of Engineering Science*, 49: 466–496, 2011.

[6] D. Schrade, R. Müller, B. X. Xu, and D. Gross. Domain evolution in ferroelectric materials: A continuum phase field model and finite element implementation, *Computer Methods in Applied Mechanics and Engineering*, 196: 4365–4374, 2007.

[7] Y. C. Shu, and K. Bhattacharya. Domain patterns and macroscopic behavior of ferroelectric materials, *Philosophical Magazine B*, 81: 2021–2054, 2001.

[8] Y. C. Shu, J. H. Yen, H. Z. Chen, J. Y. Li, and L. J. Li. Constrained modeling of domain patterns in rhombohedral ferroelectrics, *Applied Physics Letters*, 92: 0529091–0529093 2008.

[9] B. Svendsen. On the thermodynamic- and variational-based formulation of models for inelastic continua with internal lengthscales, *Computer Methods in Applied Mechanics and Engineering*, 48: 5429–5452, 2004.

[10] J. H. Yen, Y. C. Shu, J. Shieh, and J. H. Yeh. A study of electromechanical switching in ferroelectric single crystals, *Journal of the Mechanics and Physics of Solids*, 56: 2117–2135, 2008.

STRAIN-TUNING IN MULTIFERROICS

B. Dkhil[1], A. Barthélémy[2], M. Bibes[2]

[1] Laboratoire Structures, Propriétés ete Modélisation des Solides
UMR8580 CNRS – Ecole Centrale Paris
Grande voie des vignes, 92290 Châtenay-Malabry, France
email: brahim.dkhil@ecp.fr

[2] Unité Mixte de Physique CNRS / Thales & Université Paris-Sud
1 av. Fresnel, 91767 Palaiseau & 91405 Orsay, France

Abstract. *The field of multiferroics i.e. materials possessing simultaneously elastic, polar/electric and/or magnetic orders has known a rapid progress punctuated by the discovery of many new physical phenomena. Among their various physical properties, multiferroics have attracted much attention for their potential magnetoelectric properties related to the coupling between magnetization and polarization. Multiferroics are either intrinsic i.e. both magnetization and polarization coexist within the same materials, or extrinsic and then referred as hybrid or artificial multiferroics as they are constituted by two different materials, one having magnetization and the other one the polarization and the coupling is mediated at the interface through both strain and charge effects. Actually strain is revealed to be, in both systems, a key driving force allowing to tune the multiferroics properties. In this talk, I will illustrate this remarkable feature using two examples, namely the intrinsic model multiferroic compound $BiFeO_3$ and a hybrid multiferroic based on the heterostructure composed of $BaTiO_3$ and FeRh.*

1 Strain driving of $BiFeO_3$ ferroic orders

Tremendous efforts were recently devoted to study $BiFeO_3$ the model multiferroic system as thin film form because of its strain sensitivity. Indeed, epitaxial strain has recently emerged as a powerful way to tune the various remarkable physical properties of such perovskite oxide thin films. The strong coupling of ferroic orders (elastic, electric and magnetic) with the various structural degrees of freedom (notably polar and antiferrodistortive) provides multiferroic $BiFeO_3$ with very rich phase diagrams, as well as with a highly tunable, multifunctional character. Combining advanced characterization techniques (X-ray and neutron diffraction, Mössbauer and Raman spectroscopy and piezoresponse force microscopy) and *ab initio*, first-principles and phenomenological calculations, we have shown [1-6] how misfit strain can 1) affect $BiFeO_3$ phases allowing original mixed-phase state; 2) tune the critical temperatures of antiferromagnetic and ferroelectric transitions until bringing both close together; 3) modify the ferroelectric, dielectric and piezoelectric properties; and 4) control the magnetic properties and spin arrangements.I will show through some of these striking results how it is possible to strain-drive easily the whole ferroic features of this model multiferroic.

2 Tuning magnetic transition using an electric field via strain

Controlling magnetism by electric fields is a key issue for the future development of low-power spintronics. Progress has been made in the electrical control of magnetic anisotropy, domain structure, spin polarization or critical temperatures. However, the ability to turn on and off robust ferromagnetism at room temperature and above has remained elusive. Here we use ferroelectricity in $BaTiO_3$ crystals to tune the sharp metamagnetic transition temperature of epitaxially grown FeRh films and electrically drive a transition between antiferromagnetic and ferromagnetic order with only a few volts, just above room temperature. The detailed analysis of the data in the light of first-principles calculations indicate that the phenomenon is mediated by both strain and field-effect from the $BaTiO_3$. Our results correspond

to a magnetoelectric coupling larger than previous reports by at least one order of magnitude and open new perspectives for the use of ferroelectrics in magnetic storage and spintronics.

REFERENCES

[1] B. Dupé *et al*., Phys. Rev B **81**, 144128 (2010)
[2] I.C Infante *et al.*, Phys. Rev. Lett. **105**, 057601 (2010)
[3] B. Dupé *et al.*, Phys. Rev. Lett. **106**, 237601 (2011)
[4] I.C Infante *et al.*, Phys. Rev. Lett. **107**, 2376011 (2011)
[5] C. Daumont *et al.*, J. Phys. : Condens. Matter **24**, 162202 (2012)
[6] D. Sando *et al.*, Nat. Mat. **12**, 641 (2013)
[7] R.O. Cherifi *et al.*, Nat. Mat. **13**, 345 (2014)

ON AN ATOMISTIC SCALE FINITE ELEMENT METHOD FOR THE SIMULATION OF FERROELECTRIC FUNCTIONAL MATERIALS

Florian Endres[1] **and Paul Steinmann**[1]

[1] Chair of Applied Mechanics, University of Erlangen - Nuremberg
Egerlandstrasse 5, 91058 Erlangen, Germany
e-mail: florian.endres@ltm.uni-erlangen.de

Abstract. *Molecular dynamics (MD) simulations of ferroelectric materials improved over the last decades and are an indispensable tool in order to predict the behaviour of materials on an atomistic level. Especially the core-shell model has been used for the simulation of ferroelectric materials. However the computational costs of MD calculations are significant. In this work molecular statics has been implemented as a finite element method using the core-shell model. For validation of the molecular statics algorithm barium titanate has been simulated. Furthermore periodic boundary conditions have been applied in order to simulate bulk material.*

1 Introduction

Ferroelectric functional materials are simulated on different length scales between the electron structure and the continuum description. Especially models and algorithms on the atomistic level have been developed further in the last decades and not only predict materials behaviour but also help understanding material behaviour in general. At the atomistic length scale molecular dynamics is the most used algorithm for the simulation of discrete particle systems. Classical MD methods do not explicitly include quantum mechanical information and solve Newton's equations of motion using potentials in order to calculate interactions between particles [1]. For the simulation of ferroelectric materials especially the core-shell model renders reasonable results because of its ability to describe ionic and electronic polarization. Core-shell potential parameters are determined by ab initio first principles calculations. However MD simulations are costly in terms of time and for macroscopic descriptions a lot of different constitutive models are aviable using continuum approaches like e.g. phase field algorithms [2]. Continuum approaches have benefits especially in terms of calculation effort but the calculation of nanofilms and material behaviour inside a domain wall are difficult to predict by continuum approaches since the length scales of such phenomena e.g. a domain wall are only very few Ångstrom (Å) in size. On such small length scales material is not behaving like a continuum and particle based methods must be applied. For the sake of computational efficiency molecular statics has been implemented in the sense of a finite element method using the core-shell model. The interpretation of molecular statics as FEM algorithm is discussed in section 2. The used core-shell model is presented in section 3. For validation of the algorithm barium titanate ($BaTiO_3$) has been simulated and a numerical example is shown in section 4. Conclusions are finally drawn in section 5.

2 Molecular statics

The minimization of the discrete atomistic potential energy in molecular statics is analoguos to the finite element method applied to nonlinear trusses. Considering a discrete atomistic system of N particles the total energy of the system is given by

$$E^{tot} = \Phi^{int}(\mathbf{r}) + \Phi^{ext}(\mathbf{r}) = \frac{1}{2}\sum_{i=1}^{N}\sum_{j\neq i}^{N}\Phi^{int}(\mathbf{r}_{ij}) + \sum_{i=1}^{N}\mathbf{f}_i \cdot \mathbf{r}_i. \tag{1}$$

Minimization of the total potential energy leads to

$$\frac{\partial E^{tot}}{\partial \mathbf{r}} = \mathbf{0}. \tag{2}$$

Solving these nonlinear equations upon Newton iteration and in analogy to the finite element method the system of linearized equation reads as

$$\mathbf{K} \cdot \mathrm{d}\mathbf{r} = \mathbf{f}^{ext}(\mathbf{r}) - \mathbf{f}^{int}(\mathbf{r}). \tag{3}$$

Thereby the internal force and the local stiffness matrix of an interaction e between two particles i and j with $\mathbf{r}_{ij} := \mathbf{r}_j - \mathbf{r}_i$ are calculated in terms of the interaction potentials Φ_{ij} by

$$\mathbf{f}^e := \frac{\partial \Phi_{ij}}{\partial \mathbf{r}_{ij}}, \quad \mathbf{K}^e := \frac{\partial^2 \Phi_{ij}}{\partial \mathbf{r}_{ij}^2}. \tag{4}$$

Therefore the easiest interpretation of a molecular statics algorithm is a nonlinear truss network of one dimensional finite elements.

3 $BaTiO_3$ core-shell model

One of the most investigated ferroelectric materials is barium titanate. $BaTiO_3$ has a Perowskit crystal structure and 8 different spontaneous polarization directions in the rhombohedral phase. Every unit cell contains 15 ions. Using the core shell model every ion is represented by two particles. The first particle represents the atom core of an ion. The second particle represents the electron shell. Thus not only ionic but also electronic polarization is considered. Three different energy potentials are used to model the particle interactions within a ferroelectric crystal. First of all ions interact by long range Coulomb potential

$$V_{\mathbf{r}_{ij}}^{Coulomb} = \frac{q_i q_j}{4\pi\epsilon_0 \left|\mathbf{r}_{ij}\right|}. \tag{5}$$

Furthermore electron shells interact by a Buckingham potential

$$V_{\mathbf{r}_{ij}}^{Buck} = A \exp\left(\frac{\left|\mathbf{r}_{ij}\right|}{\rho}\right) - \frac{c}{\left|\mathbf{r}_{ij}^6\right|}. \tag{6}$$

The third interaction potential represents the bonding between the atom core and the electron shell of an ion using a nonlinear spring potential

$$V_{\mathbf{r}_{ij}}^{Spring} = \frac{1}{2}k_2\left|\mathbf{r}_{ij}^2\right| + \frac{1}{24}k_4\left|\mathbf{r}_{ij}^4\right|. \tag{7}$$

The used parameters are shown in table 1 and fit ab initio total energy calculations [3, 4].

Atom	Core charge ($\|e\|$)	Shell charge ($\|e\|$)	k_2(eVÅ^{-2})	k_4(eVÅ^{-4})
Ba	5.62	-3.76	251.80	-
Ti	4.76	-1.58	322.0	-
O	0.91	-2.59	31.0 ($\|\|$)101.27($\perp$)	3000($\perp$)
Short-range	A (eV)	ρ (Å)	c (eVÅ^6)	
Ba-O	864.536	0.38729	0.0	
Ti-O	4526.635	0.25239	0.0	
O-O	4102.743	0.29581	300.0	

Table 1: Symbol * means that the Ti core charge is obtained with a neutrality condition. The symbol $||$ and $\perp$ indicate directions of the Ti-O bond [3].

4 Numerical examples

For the numerical examples barium titanate has been simulated since it is one of the most investigated ferroelectric materials [5]. As an initial configuration a cubic $BaTiO_3$ lattice with 5x5x5 unit cells and 3750 particles has been simulated. The lattice constant has been chosen as 4Å. Furthermore a cut-off radius $R_c = 9.999$Å and periodic boundary conditions have been applied in order to reduce the calculation effort. The boundaries of the simulation box have been fixed. For the calculation of the dielectric hysteresis behaviour an electric field has been applied in $[1\ 1\ 1]^T$ direction. For the sake of numerical stability the Wolf summation has been used to calculate long range Coulomb interactions. For a detailed description of the Wolf summation technique we refer to [6].

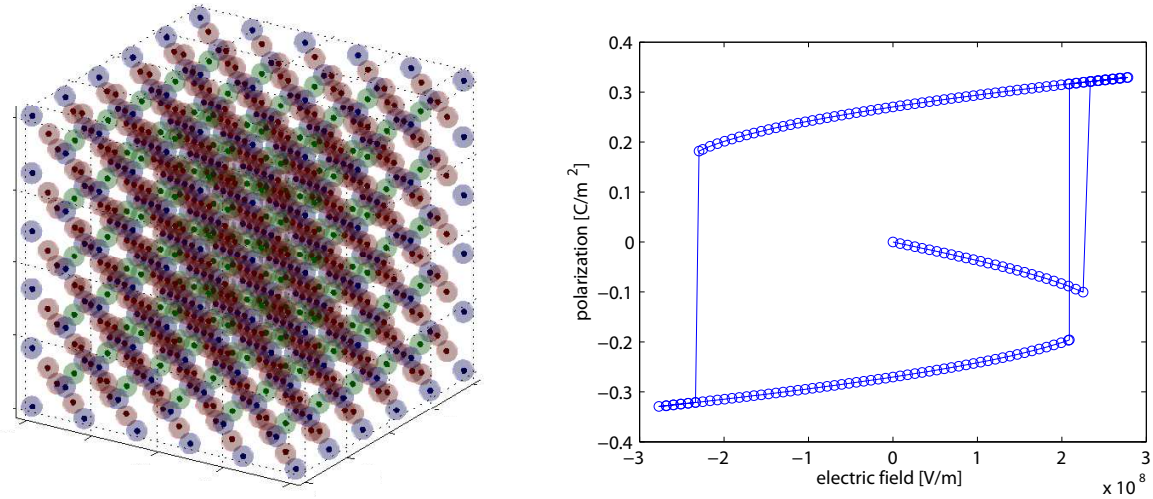

Figure 1: 5x5x5 $BaTiO_3$ system and dielectric hysteresis loops

Figure 1 depicts the simulated particle system and the calculated dielectric hysteresis loop. The polarization is evaluated along the diagonal $[1\ 1\ 1]^T$ direction.

5 Conclusion

This study discusses an algorithm for the calculation of ferroelectric hysteresis behaviour of functional materials using an atomistic finite element method. Considering the computational

costs of ab initio and MD simulations molecular statics has advantages especially in the calculation of equilibrium configurations. Therefore the coupling of molecular statics and continuum mechanics is a promising future application.

Acknowledgements

The authors would like to thank the German Research Foundation (DFG) for the financial support of this project under the research group project FOR 1509 Ferroische Funktionsmaterialien.

REFERENCES

[1] Ellad B. Tadmor and Ronald E. Miller. Continuum,Atomistic and Multiscale Techniques, *Modeling Materials*, Cambridge University Press New York, 2011.

[2] M. Kamlah. Ferroelectric and ferroelastic piezoceramics - modeling of electromechanical hysteresis phenomena, *Continuum Mechanics and Thermodynamics*, 13 : 219-268, 2001.

[3] S. Tinte, M. G. Stachiotti, M. Sepliarsky, R. L. Migoni, C. O. Rodriguez. Atomistic modelling of $BaTiO_3$ based on first-principles calculations, *Journal of Physics: Condensed Matter*, 11 : 9679-9690, 1999.

[4] D. Khatib, R. Migoni, G. E. Kugel and L. Godfroy. Lattice dynamics of $BaTiO_3$ in the cubic phase, *Journal of Physics: Condensed Matter*, 1 : 9811-9822, 1989.

[5] G. H. Kwei, A. C. Lawson, S. J. L. Billinge. Structures of Ferroelectric Phase of Barium Titanate, *Journal of Physical Chemistry*, 97 : 2368-2377, 1993.

[6] D. Wolf, P. Keblinski, S. R. Phillpot and J. Eggebrecht. Exact method for the simulation of Coulombic systems by spherically truncted, pairwise r-1 summation, *Journal of Chemical Physics*, 110 : 266-267, 1999.

MICROMECHANICALLY-BASED MODELING FOR MAGNETO-VISCO-ELASTICITY OF MAGNETO-SENSITIVE ELASTOMERS

Gautam Ethiraj, Dominic Zäh, and Christian Miehe[1]

[1] Institute of Applied Mechanics (CE), Chair 1, University of Stuttgart
Pfaffenwaldring 7, 70569 Stuttgart, Germany
e-mail: christian.miehe@mechbau.uni-stuttgart.de

Abstract. *Over the last two decades a variety of magnetorheological elastomers (MREs) and devices utilizing them, have been patented and developed by scientists and engineering companies such as Ford Co., Toyota and Lord Co. Such materials with tunable mechanical properties find use in controllable stiffness devices for the active control of structural components eg. in engine mounts and automotive bushings. Thus there is an added need to model such materials in a manner that is convenient for structural and modal analysis ie. within a FEM framework. In this work we present the modular construction and FEM implementation of a MRE material model that is firmly rooted in micromechanics and is tested against experimental data. Keeping in mind the composite nature at the microscale, we develop a constitutive formulation based on a multiplicative magneto-mechanical split of the deformation gradient. We consider both Lee- and Clifton-type right and left decompositions, where the latter seems more appropriate due to its dependence on the true magnetic field. In contrast to recent formulations like [6] and [7] this general approach allows the use of micromechnically-based network models for polymers in a modular format and to extend its application for coupled magnetomechanical response.*

1 Introduction and Physical Background of MREs

MREs are a class of composite materials consisting of rigid, magnetizable iron particles embedded in a viscoelastic rubber matrix. In the microscale picture below it can be shown that the tangential component of the total force between two magnetic dipoles with arbitrary magnetic moments $\boldsymbol{\mathcal{F}}_\theta = 2(\boldsymbol{m}\cdot\boldsymbol{e}_r)(\boldsymbol{m}\cdot\boldsymbol{e}_\theta)\boldsymbol{e}_\theta$ always acts in such way so as to *align the magnetic moments*. This key factor motivates us to consider a multiplicative split of the deformation gradient into elastic and magnetic parts.

2 Rate-type Variational Principle for Multiplicative Magneto-Visco-Elasticity

The magneto-visco-elastic boundary value problem is governed by the rate-type variational principle

$$\{\dot{\boldsymbol{\varphi}}, \dot{\phi}, \dot{\mathcal{I}}\} = \arg\Big\{ \inf_{\dot{\boldsymbol{\varphi}}} \sup_{\dot{\phi}} \inf_{\dot{\mathcal{I}}} \int_{\mathcal{B}} \big[\frac{d}{dt}\Psi(\boldsymbol{F}, \boldsymbol{H}, \mathcal{I}; \boldsymbol{X}) + \Phi^v(\dot{\mathcal{I}})\big]\, dV - \Pi_{ext} \Big\} \tag{1}$$

where $\Pi_{ext} = \int_{\mathcal{B}} \bar{\boldsymbol{\gamma}}\cdot\dot{\boldsymbol{\varphi}}\, dV + \int_{\partial\mathcal{B}_t} \bar{\boldsymbol{t}}\cdot\dot{\boldsymbol{\varphi}}\, dA + \int_{\partial\mathcal{B}_b} \bar{B}\dot{\phi}\, dA$. The necessary condition of the saddle point principle gives the equilibrium condition $\mathrm{Div}[\boldsymbol{P}] = \boldsymbol{0}$, Gauss's law $\mathrm{Div}[\boldsymbol{B}] = 0$, Biot

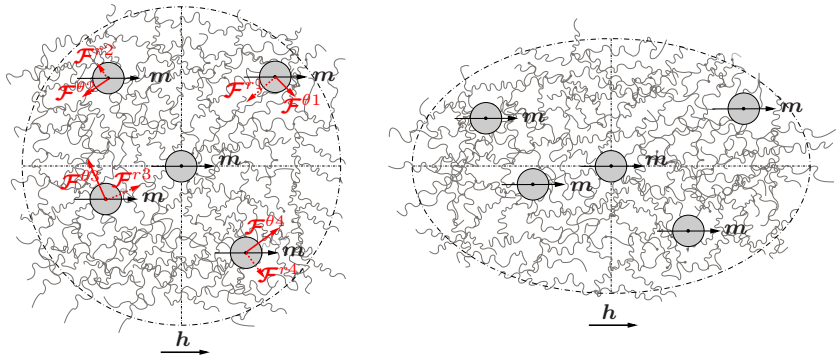

Figure 1: Schematic representation of the deformation of the magnetorheological elastomer at the microscale.

equation for the evolution of the internal variables $\partial_{\mathcal{I}}\Psi + \partial_{\dot{\mathcal{I}}}\Phi^v = 0$ and boundary conditions as the Euler equations. For more advanced concepts on variational frameworks for coupled electro-magneto-mechanical problems, see [1], [2] and [3].

Ingredient 1: Additive split of energy-enthalpy density. We assume an additive decomposition of the total enthalpy function per unit volume of the reference configuration into a mechanical part Ψ_{mech}, including visco-elastic contributions due to micromechanically-based network models of polymers, and a *magnetostatic part* Ψ_{mag}. Thus $\Psi = \Psi_{mech} + \Psi_{mag}$.

Ingredient 2: Volumetric-isochoric split of local deformation. The mechanical contribution to the enthalpy function is assumed to decompose

$$\Psi_{mech}(\boldsymbol{F}, \boldsymbol{H}, \mathcal{I}) = U(J) + \bar{\Psi}^e(\bar{\boldsymbol{F}}, \boldsymbol{H}) + \bar{\Psi}^v(\bar{\boldsymbol{F}}, \boldsymbol{H}, \mathcal{I}) \tag{2}$$

into a volumetric contribution and a viscous and elastic isochoric part. The viscous internal variable is determined by an additional evolution equation explained below.

Ingredient 3: Local magnetically-induced deformation. The modular approach relies on a kinematic assumption for a local homogeneous magnetostrictive deformation, depending on the material or spatial magnetic field $\mathbb{x} := \{\boldsymbol{H}, \boldsymbol{h}\}$, respectively. We obtain a closed-form expression for the inverse isochoric stretch $\bar{\boldsymbol{\mathcal{E}}}(\mathbb{x}) = (1+f)^{-2/3}\big[(1+f)\boldsymbol{1} - f\,\mathbb{n}\otimes\mathbb{n}\big]$, where $\mathbb{n} = \mathbb{x}/|\mathbb{x}|$. Thus we define an elastic network deformation $\bar{\boldsymbol{F}}_{net}$

$$\bar{\boldsymbol{F}}_{net} := \begin{cases} \bar{\boldsymbol{F}} & \text{- case 1: total isochoric deformation,} \\ \bar{\boldsymbol{F}}\bar{\boldsymbol{\mathcal{E}}}(\boldsymbol{H}) & \text{- case 2: right multiplicative decomposition,} \\ \bar{\boldsymbol{\mathcal{E}}}(\boldsymbol{h})\bar{\boldsymbol{F}} & \text{- case 3: left multiplicative decomposition.} \end{cases} \tag{3}$$

Ingredient 4: Local isochoric elastic network kernel. The current framework allows us to include micromechanically-based network models for polymers in a modular manner. In particular, we use the model in [4]. The micromechanical kernel defines the elastic network storage energy $\bar{\Psi}^e = \langle \bar{\psi}^e(\lambda_{net}) \rangle$ and the viscous network storage function $\bar{\Psi}^v = \langle \bar{\psi}^v(\lambda_{net}, \varepsilon^i) \rangle$ with branch number $i = 1...s$. The macro-dissipation is obtained by a homogenization procedure as $\Phi^v = \langle \phi^v(\dot{\varepsilon}^i) \rangle$ in terms of the micro-dissipation functions of the form

$$\phi^v = \sum_{i=1}^{s} \frac{\delta^i}{\eta^i(1+\delta^i)} (\eta^i |\dot{\varepsilon}^i|)^{\frac{1+\delta^i}{\delta^i}} \,. \tag{4}$$

Ingredient 5: Local magnetostatic contribution to the energy. We outline a purely phenomenological structure of the magnetostatic contribution to the enthalpy function

$$\hat{\Psi}_{mag} = -\frac{\mu_0}{2} J(\boldsymbol{h}\otimes\boldsymbol{h}) - \mu_0 m_s \eta \, \ln(\cosh(\boldsymbol{h}\cdot\boldsymbol{h}/\eta)) \,. \tag{5}$$

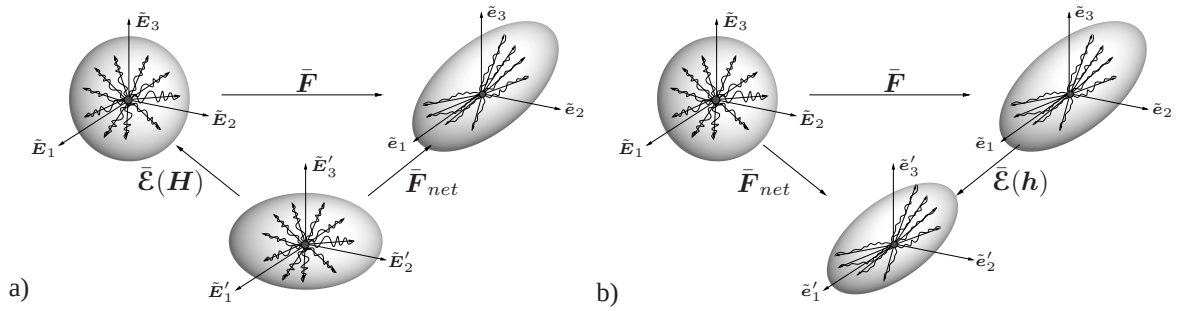

Figure 2: Multiplicative decompositions: a) *Lee-type:* $\bar{\boldsymbol{F}}_{net} = \bar{\boldsymbol{F}}\bar{\mathfrak{E}}(\boldsymbol{H})$ and b) *Clifton-type:* $\bar{\boldsymbol{F}}_{net} = \bar{\mathfrak{E}}(\boldsymbol{h})\bar{\boldsymbol{F}}$.

This relatively simple constitutive ansatz aims to capture the free space contribution as well as the magnetic energy stored in the material by virtue of its magnetization.

3 Representative Numerical Examples

We present some simulations to display the salient eatures of our modeling approach. For all simulations we have used the viscoelastic microsphere model in [4] which is based on [5].

3.1 Dynamic Compression Test

This simulation compares the results of our model with the experimental data. Here we compare the force vs. displacement of an MRE sample in an applied magnetic field. The magnetic field is applied on an MRE block in the direction of the deformation. We apply a sinusoidal displacement and plot the corresponding reaction force. The results of the model show a good

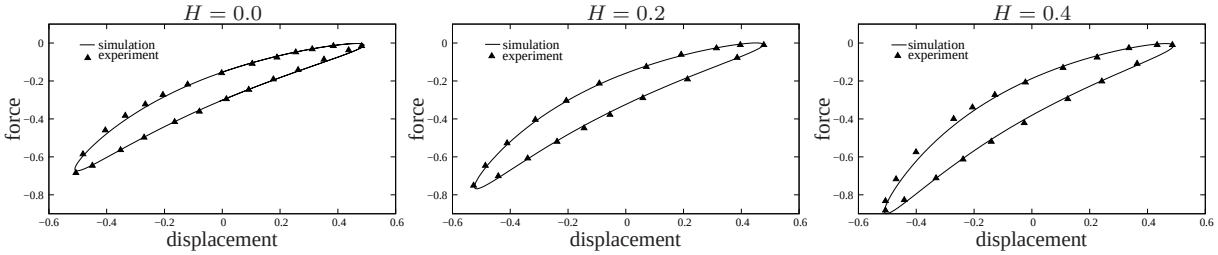

Figure 3: Experimental data and the numerical results compared for different magnetic fields.

match with the experimental data which is attributed in no small way to the highly predictive microsphere model that resides in the isochoric kernel. This fact also favors the presented modular approach.

3.2 MRE Block with Stiff Inclusion

In this example we consider a cubic block of the MRE with a stiff non-magnetic spherical inclusion. A monotonically increasing magnetic potential difference is applied parallel to one of the edges. Due to symmetry, only $1/8^{th}$ of the geometry is used. A mesh consisting of 783 elements is used to discretize the domain. As expected, there is a deformation of the matrix in the direction of the magnetic field. The stiff inclusion however, causes an inhomogeneous deformation around it. The pole figures show the stereographic projection of the stretch at specific material points in the vicinity of the stiff inclusion.

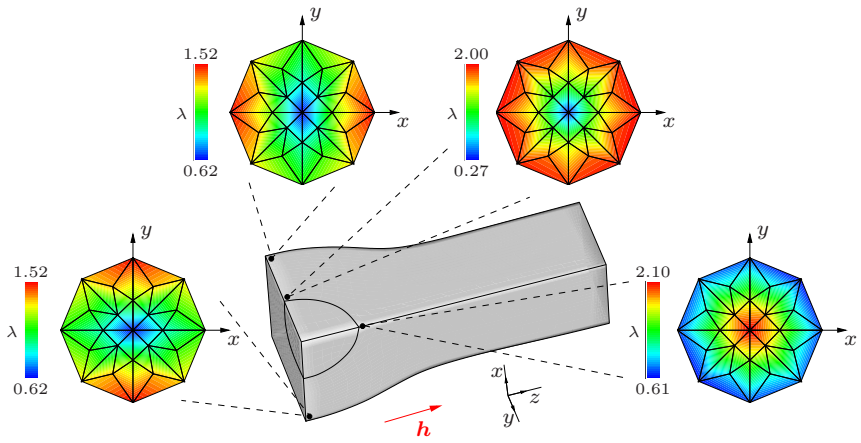

Figure 4: Deformed geometry with pole figures to indicate the stretch λ at chosen points.

4 Conclusion

We have presented a highly predictive material model for isotropic MREs, as well as a modular framework for the construction of MRE material models that use micromechanically-based network kernels. The material model presented performs well against experiment. The modular construction of the model presents a framework for the construction of more complex models. Additionally, we have presented FEM simulation of boundary value problems.

REFERENCES

[1] C. Miehe, B. Kiefer, and D. Rosato. An incremental variational formulation of dissipative magnetostriction at the macroscopic continuum level, *International Journal of Solids and Structures*, 48: 1846–1866, 2011.

[2] C. Miehe, and D. Rosato, and B. Kiefer. Variational principles in dissipative electro-magneto-mechanics: A framework for the macro-modeling of functional materials, *International Journal for Numerical Methods in Engineering*, 86: 1225–1276, 2011.

[3] C. Miehe, and G. Ethiraj. A Geometrically Consistent Incremental Variational Formulation for Phase Field Models in Micromagnetics, *Computer Methods in Applied Mechanics and Engineering*, 245–246, 331–347, 2012.

[4] C. Miehe, and S. Göktepe. A Micro-Macro Approach to Rubber-Like Materials. Part II: The Micro-Sphere Model of Finite Rubber Viscoelasticity, *Journal of the Mechanics and Physics of Solids*, 53, 2231–2258, 2005.

[5] C. Miehe, S. Göktepe, and F. Lulei. A Micro-Macro Approach to Rubber-Like Materials. Part I: The Non-Affine Micro–Sphere Model of Rubber Elasticity, *Journal of the Mechanics and Physics of Solids*, 52, 2617–2660, 2004.

[6] K. Danas, S. V. Kankanala, and N. Triantafyllidis. Experiments and modeling of iron-particle-filled magnetorheological elastomers, *Journal of the Mechanics and Physics of Solids*, 60, 120–138, 2012.

[7] P. Saxena, M. Hossain, and P. Steinmann. A theory of finite deformation magneto-viscoelasticity, *International Journal of Solids and Structures*, 50, 3886–3897, 2013.

MAGNETOELECTRIC (0-3) COBALT FERRITE BARIUM TITANATE COMPOSITES, A NANOSCALE TO MACROSCALE INVESTIGATION

Morad Etier[1], V.V. Shvartsman[1], Yanling Gao[1], Soma Salamon[2], Joachim Landers[2], Heiko Wende[2] and Doru C. Lupascu[1]

[1] Institute for Materials Science, Faculty of Engineering, University of Duisburg-Essen
Universitätsstraße 15, 45141 Essen, Germany
doru.lupascu@uni-due.de

[2] Institute of Experimental Physics, Faculty of Physics, University of Duisburg-Essen
Lotharstraße 1, 47048 Duisburg, Germany

Abstract. *Magnetoelectric materials allow control of the magnetization by an external electric field or vice versa. These materials have received much attention recently due to their attractive technological applications in sensors, actuators, potentially energy harvesters and non-volatile random access memories. Composite materials show sufficient magnetoelectric coupling in the vicinity of room temperature while intrinsic multiferroics only provide large coupling at low temperature. We report on the converse magnetoelectric coupling in (0-3) ceramics composed of ferroelectric barium titanate and ferrimagnetic cobalt ferrite. Using an organosol method we have successfully synthesized cobalt ferrite-barium titanate (x)$BaTiO_3$-(1-x) $CoFe_2O_4$ nanopowders having a core-shell structure. The powder was sintered into ceramics with (0-3) connectivity. Phases and morphology of the powder and ceramic samples were studied using x-ray diffraction and scanning electron microscopy. Ferroelectric and magnetic properties were investigated by a Sawyer-Tower circuit and SQUID magnetometry, respectively. Electrically induced magnetization was tested using a modified SQUID ac-susceptometer for measuring the converse magnetoelectric coupling coefficient (α_C).We observed a value of* $\alpha_C = 2.37\times10^{-10} sm^{-1}$ *for the composite containing 60% weight percent of barium titanate.*

1 Introduction

Materials that exhibit two or more ferroic orders e.g. ferromagnetism and ferroelectric are defined to be "multiferroics". The outstanding physical properties of these materials make them the first candidate for future sensors and actuators technology [1-2]. The magnetoelectric effect is expected in multiferroic materials where the control of polarization and magnetization is possible by magnetic and electric field. A weak magnetoelectric effect was experimentally measured in single phase magnetoelectric multiferroics at low temperature [3]. On the other hand, a larger magnetoelectric effect can be found in composite multiferroic magnetoelectric materials even at ambient temperature. In multiferroic composites, the strain mediated approach is the main cause of the magnetoelectric coupling so that the mechanical strain between the piezomagnetic and piezoelectric in the interface is the main factor. As the interface between the phases is very important, the core shell structure is a promising approach for enhancing magnetoelectric coupling due to the large well defined area between the piezoelectric and piezomagnetic components [4]. Such core shell structure can be realized by ferromagnetic cores such as cobalt ferrite and ferroelectric shells such as barium titanate. Large magnetostriction of polycrystalline cobalt ferrite ≈ 400ppm [5] and large longitudinal piezoelectric coefficient 190pCN^{-1} of barium titanate [6] make them promising for fabrication of multiferroic magnetoelectric composites. In this paper we report on the synthesis and measurements of the magnetoelectric effect of (0-3) cobalt ferrite barium titanate ceramic composites sintered from core shell nanoparticles.

2 Experimental procedures

For synthesizing multiferroic magnetoelectric composites, cobalt iron oxide nanoparticles were successfully synthesized by co-precipitation method described in detail in [7]. The process of coating the magnetic particles by barium titanate was accomplished by two main steps; the first is making a very stable cobalt iron oxide ferrofluid. In this case the hydrophobic cobalt ferrite was suspended in toluene. Second the ferrofluid was added to barium titanate organsol creating a multi-phase precursor. Anhydrous tetramethyl-ammonium hydroxide (TMAH, Sigma-Aldrich) was added at 90◦C to promote gelation. All of the exact procedures, quantities and methods are described in [8]. The core shell powder was obtained by calcinating the gel at 750°C for 15 minutes. The powder was pressed into cylindrical pallets and then sintered at 1200°C for 2 hours in order to have a (0-3) ceramic composite. The morphology and structure of the specimens was studied by scanning and transmission electron microscopy (SEM and TEM). The ferroelectric and ferromagnetic hysteresis loops were measured using a Sawyer-Tower circuit and SQUID respectively. Commercial microscopes SEMquanta 400 FEG and TEM TECNAI F20 were used. For the magnetoelectric measurements, a converse magnetoelectric coupling coefficient was determined in a modified SQUID ac-susceptometer using the following procedure, an ac electric field, $E = E_{ac} \cos \omega t$ was applied to the sample depending on the thickness. The lock-in amplifier inside the SQUID was used to detect the harmonic induced ac magnetic moment $m' = m_{ME} \cos \omega t$. The converse magnetoelectric coefficient α_C was calculated from the ac electric field dependence of the induced magnetization.

3 Results and Discussions

The analysis of x-ray diffraction -not shown here- for the calcined cobalt ferrite and cobalt ferrite barium titanate core shell structure proved the crystallinity of the two phases. No other phases are detected assuring the purity of the composite. Figure 1.a shows SEM image for cobalt iron oxide nanoparticles. The monodisperse particles distribute in the range of 30-40 nm. The composite core shell nanopowder is shown in figure 1.b. The particles sizes are distributed in the range of 110-120 nm. Higher magnification of the particles is shown in the inset. The darker core and brighter shell are easily distinguished as well as the energy dispersive analysis which confirmed the core shell nature of the powder [9]. In TEM analysis of the powder, the interplanar spaces between the planes are measured in cores and shells. These measurements were in good agreement with x-ray diffraction data [8].

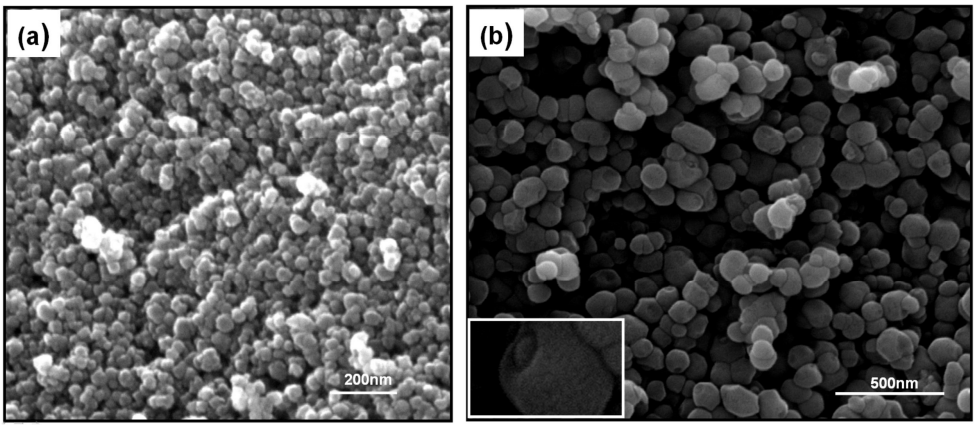

Figure 1: SEM images for (a) calcined cobalt iron oxide nanoparticles synthesized by co-precipitation method (b) calcined (1-x)$CoFe_2O_4$-(x)$BaTiO_3$ [x=0.8] core shell structure. The inset shows a magnification of a particle with a core shell structure [7,8].

Figure 2 shows the SEM images for the ceramic sample. The bright regions are the matrix of barium titanate which was also proved by EDS previously. Cobalt iron oxide regions (dark regions) distributed in barium titanate matrix in the size of ≈ 2μm. To prove the (0-3) nature of the composites SEM scan

was done in the edge of the sample as shown in figure 2.b. The cobalt iron oxide regions are separated from each other forming (0-3) composite compared with the biphasic ideal model shown in the figure. This separation may lead to better contact between the ferromagnetic and ferroelectric region, better isolation of the magnetic particles and higher resistivity of the sample and consequently proper poling and enhanced magnetoelectric effect.

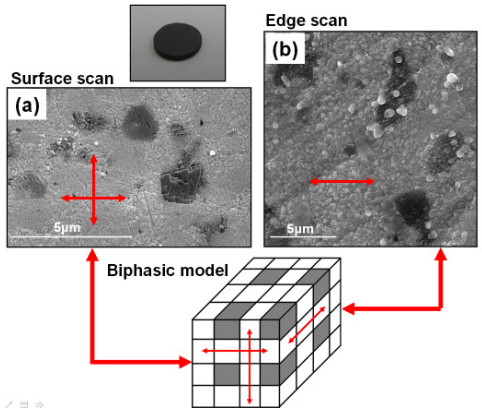

Figure 2: Ceramic (1-x)$CoFe_2O_4$-(x)$BaTiO_3$ [x=0.8] sintered at 1200°C and thermally etched (a) surface SEM image (b) edge SEM image. Above is the ceramic sample and at the bottom an illustration of the biphasic brick model for (0-3) ceramic composites.

The multiferroic nature of the composites was verified by measuring both the polarisation electric field and the magnetization magnetic field hysteresis loops. Typical ferromagnetic and ferroelectric behaviour were observed [9]. After that, the ac electric field dependence of the electrically induced magnetization was measured and shown in figure 3. The measurements were done for different compositions (x=0.8, 0.7, 0.6). All of the measurements were done at temperature 285K because the maximum ME response was detected at this temperature. From the linear relation between the electric field applied and the induced magnetization, the slope of the line is the converse magnetoelectric effect which can be estimated by the relation $\alpha_C = (M_{ME}\mu_o)/(E_{ac})$ where the value of M_{ME} is the electrically induced magnetization divided by the volume of the sample. The maximum magnetization response according to the electric field was recorded for the sample with composition x=0.6. The value of converse magnetoelectric effect was estimated to be $2.37\times10^{-10} sm^{-1}$ which is seven times larger than the best single phase magneoelectric material. The value of $4.4\times10^{-12} sm^{-1}$ was estimated also for the compositions x=0.8. These values still comparable with values reported for samples with the same weight fraction between the piezoelectric and piezomagnetic phases.

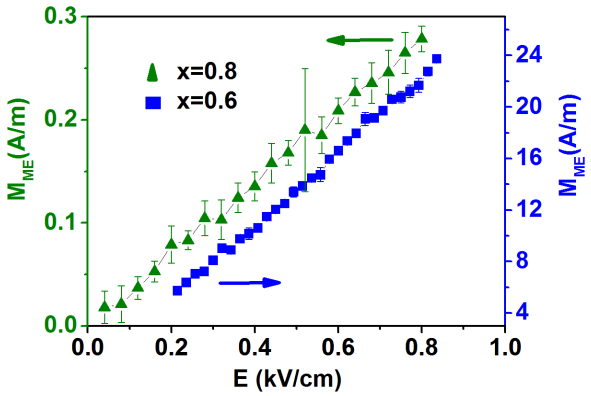

Figure 3: Electric field dependence of electrically induced magnetization for ceramic (1-x)$CoFe_2O_4$ - (x)$BaTiO_3$ sintered at 1200 °C and measured at μ_oH=0.15 T, T= 285K and f=10Hz.

4. Conclusion

Using both the co-precipitation and organosol method we have successfully synthesized different compositions of multiferroic cobalt ferrite barium titanate core shell nanoparticles. The mean sizes of particles are 110-120 nm with shell thickness about 40nm. The nanoparticles were converted into (0-3) ceramic magnetoelectric composite. We proved the multiferroic nature of the different compositions. The maximum magnetoelectric coupling coefficient $2.37\times10^{-10} sm^{-1}$ was recorded to the composition (x)$BaTiO_3$-(1-x) $CoFe_2O_4$ (x=0.6). This value is larger than the best single phase magnetoelectric coefficient and comparable with others values previously reported. We related this large value to proper separation of magnetic particles in the ferroelectric matrix as well as accurate magnetoelectric measurement technique used.

REFERENCES

[1] W. Eerenstein, N. D. Mathur, and J. F. Scott, Multiferroic and magnetoelectric materials, *Natur.,* 442: 759–765, 2006.

[2] C. A. F. Vaz, J. Hoffman, C. H. Ahn, and R. Ramesh, Magnetoelectric coupling effects in multiferroic complex oxide composite structures, *J. Adv. Mater*. 22: 2900–2918, 2010.

[3] G. T. Rado, J. M. Ferrari and W. G. Maisch, Magnetoelectric susceptibility and magnetic symmetry of magnetoelectrically annealed $TbPO_4$, *Phys. Rev. B.* 29: 4041–4048, 1984.

[4] V. Corral-Flores, D. Bueno-Baques, D. Carrillo-Flores, and J. A. Matutes-Aquino, Enhanced magnetoelectric effect in core-shell particulate composites, *J. Appl. Phys.* 99: 08J503, 2006.

[5] A.Muhammad, R. Sato-Turtelli,M. Kriegisch, R. Gr¨ ossinger, and F. Kubel, Large Enhancement of magnetostriction due to compaction hydrostatic pressure and magnetic annealing in $CoFe_2O_4$. *J. Appl. Phys.* 111: 013918–013922, 2012.

[6] K. Uchino, *Ferroelectric devices*, 2nd Edition. Boca Raton: CRC Press; 2010.

[7] M. F. Etier, V. V. Shvartsman, F. Stromberg, J. Landers, H.Wende, and D. C. Lupascu, Synthesis and magnetic properties of cobalt ferrite nanoparticles, *Mater. Res. Soc. Symp. Proc.* 1398, 2012.

[8] M. Etier, Y. Gao, V. V. Shvartsman, A. Elsukova, J. Landers, H. Wende, and D. C. Lupascu, Cobalt ferrite/Barium titanate core/shell nanoparticles, *Ferroelectrics*, 438: 115–122, 2012.

[9] Morad Etier, Vladimir V. Shvartsman, Yanling Gao, Joachim Landers, Heiko Wende, and Doru C. Lupascu, Magnetoelectric Effect in (0–3) $CoFe_2O_4$-$BaTiO_3$(20/80) Composite Ceramics Prepared by the Organosol Route, *Ferroelectrics*, 448: 77-85, 2013.

AKNOWLEDGMENT

Morad Etier acknowledges financial support by Deutscher Akademischer Austauschdienst (DAAD). This work was partly supported by the DAAD-GRISEC program (Grant 50750877) and Deutsche Forschungsgemeinschaft (DFG, Lu729/12).

NUMERICAL ANALYSIS OF DOMAIN SWITCHING AND DAMAGE EVOLUTION IN FERROELECTRIC DEVICES

R. Gellmann[1], **A. Ricoeur**[2]

[1,2] Institute of Mechanics, Department of Mechanical Engineering, University of Kassel
Mönchebergstr. 7, 34125 Kassel, Germany
e-mail: gellmann@uni-kassel.de

Abstract. *In this paper a damage model for ferroelectric materials is presented. It is implemented in terms of a user element in a commercial FEM-code Abaqus. The model is based on micromechanical considerations of domain switching and its interaction with microcrack growth and coalescence. The influence of damage evolution on the effective material properties is demonstrated. Further, a finite element analysis of a multilayer actuator is performed, showing damage and crack patterns.*

1 Introduction

Ferroelectric materials as components of smart structures are widely used in e.g. actuators, acoustic sensors as well as in airfoil control systems. Due to the brittleness of these materials, fracture mechanical approaches are playing an essential role in the modern research. Depending on the application, the material is subjected to mechanical, electrical or combined electromechanical loading. The mechanics of these materials is significantly determined by irreversible nonlinear ferroic effects arising on the microscopic scale, such as polarization switching. These switching processes are accompanied by internal stresses due to the strain incompatibility between neighboring grains, which results in damage and thus a significant variation of the material properties [1]. That means that a comprehensive ferroelectric material model should consider fracture and damage mechanical approaches. Besides that, the long term reliability of smart structures requires the application of numerical tools predicting crack initiation and growth under electromechanical loading conditions.

2 Micromechanical Model

The nonlinear effects are modelled by decomposing the strain ϵ_{ij} and electric displacement D_i additively into a linear piezoelectric part denoted with a superscript rev and a remanent strain $\epsilon_{ij}^{\text{irr}}$ and remanent polarization P_i^{irr} emerging due to polarization switching phenomena

$$\epsilon_{ij} = \epsilon_{ij}^{\text{rev}} + \epsilon_{ij}^{\text{irr}}, \qquad D_i = D_i^{\text{rev}} + P_i^{\text{irr}}. \tag{1}$$

The remanent parts are functions of the load history and remain after switching off the electric field and mechanical stress. The domain switching is simulated by applying a multidomain switching model of polycrystalline ferroelectrics, as illustrated in Fig. 1. Four possible domain species are assumed with $\nu^{(N)}$ being the volume fraction of the N^{th} domain within the

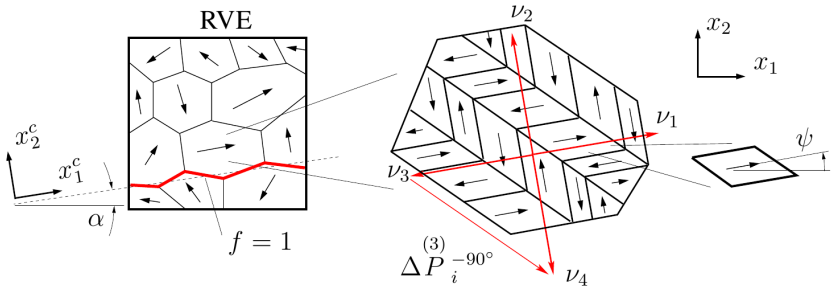

Figure 1: Schematic illustration of an RVE, a single polycrystalline grain with 4 possible tetragonal domain species and a single domain with poling direction ψ in the (x_1, x_2) plane.

representative volume element (RVE). The volume fractions satisfy the following relation

$$\sum_{N=1}^{4} \nu^{(N)} = 1, \qquad 0 \leq \nu^{(N)} \leq 1. \tag{2}$$

The macroscopic constitutive law in a RVE is given by

$$\sigma_{ij} = C_{ijkl}(\epsilon_{kl} - \epsilon_{kl}^{\text{irr}}) - e_{kij}E_k, \tag{3}$$

$$D_i = e_{ikl}(\epsilon_{kl} - \epsilon_{kl}^{\text{irr}}) + \kappa_{ik}E_k + P_i^{\text{irr}}. \tag{4}$$

Here, ϵ_{ij}, σ_{ij}, E_i and D_k are respectively the components of the total strain, local stress tensor, electric field and electric displacement vector. C_{ijkl}, e_{ikl}, κ_{ij} are respectively the effective elastic, piezoelectric and the dielectric constants, which depend on the current configuration of domain structure in the RVE. They are obtained by averaging over all domains within an RVE

$$C_{ijkl} = \sum_{N=1}^{4} C_{ijkl}^{(N)}\nu^{(N)}, \qquad e_{ijk} = \sum_{N=1}^{4} e_{ijk}^{(N)}\nu^{(N)}, \qquad \kappa_{ij} = \sum_{N=1}^{4} \kappa_{ij}^{(N)}\nu^{(N)}. \tag{5}$$

For small deformations, the strain tensor and electric field are calculated from the displacement gradient and the gradient of the scalar potential, respectively

$$\varepsilon_{ij} = (u_{i,j} + u_{j,i})/2, \qquad E_i = -\varphi_{,i}. \tag{6}$$

Within each domain, the polarisation vector P_i is assumed to switch as soon as mechanical and electrical energy reduction exceeds a critical energy barrier w_{crit}^{γ}, see [2]. The switching is interpreted as the rotation of the polarization vector around the out-of-plane axis, see Fig. 1. The evolution law for the change of internal variables $\dot{\nu}_N$ reads

$$w_{\text{diss}}^{\gamma(N)} = \sigma_{ij}\Delta\epsilon_{ij}^{\gamma(N)} + E_i\Delta P_i^{\gamma(N)}, \qquad \dot{\nu}_N = -\dot{\nu}_N^0 \mathcal{H}\left(\frac{w_{\text{diss}}^{\gamma(N)}}{w_{\text{crit}}^{\gamma}} - 1\right), \tag{7}$$

where $\dot{\nu}_N^0$ is a model parameter and different switching variants $\gamma = \pm 90^\circ, 180^\circ$ are distinguished. Here, $w_{\text{diss}}^{\gamma(N)}$ is the sum of mechanical and electrical work per unit volume for the N^{th} domain species and w_{crit}^{γ} corresponds to the minimal energy required for domain switching, such that $w_{\text{crit}}^{\pm 90^\circ} = \sqrt{2}E_C P^0$, and $w_{\text{crit}}^{180^\circ} = 2E_C P^0$. In Eq. (7) a generalized Reuss approximation is

implied. That is, the mechanical stresses and the electric field components are assumed to be constant and are not modified by the switching events. The local coordinates of the spontaneous strain $\Delta\epsilon_{ij}^{\gamma(N)}$ and change of polarisation $\Delta P_i^{\gamma(N)}$ are described by $\epsilon_D = (c-a)/a_0$

$$\Delta\epsilon_{ij}^{\pm 90^\circ} = \epsilon_D \begin{pmatrix} 1 & 0 \\ 0 & -1 \end{pmatrix}, \quad \Delta\epsilon_{ij}^{180^\circ} = 0, \tag{8}$$

$$\Delta P_k^{+90^\circ} = P^0 \begin{pmatrix} -1 \\ 1 \end{pmatrix}, \quad \Delta P_k^{-90^\circ} = P^0 \begin{pmatrix} -1 \\ -1 \end{pmatrix}, \quad \Delta P_k^{180^\circ} = P^0 \begin{pmatrix} -2 \\ 0 \end{pmatrix}. \tag{9}$$

The changes of remanent strain and polarization induced by domain switching are calculated by building a sum over all switching events weighted by the change of the corresponding volume fraction $d\nu^{(N)}$, such that

$$\mathrm{d}\epsilon_{ij}^{\mathrm{irr}} = \sum_{N=1}^{4} \Delta\epsilon_{ij}^{\gamma(N)} \mathrm{d}\nu^{(N)}, \qquad \mathrm{d}P_i^{\mathrm{irr}} = \sum_{N=1}^{4} \Delta P_i^{\gamma(N)} \mathrm{d}\nu^{(N)}. \tag{10}$$

Note, once the polarization switches, the irreversible strain is locked and cannot be reverse-switched unless external loads enforce it.

The above outlined model is implemented into a FE algorithm by introducing two additional terms on the right-hand side of the algebraic system of equations, $\{f_e\}$ and $\{q_e\}$, such that

$$[K_{uu}]\{u\} + [K_{u\varphi}]\{\varphi\} = \{f\} + \{f_e\}, \tag{11}$$

$$[K_{\varphi u}]\{u\} + [K_{\varphi\varphi}]\{\varphi\} = \{q\} + \{q_e\}. \tag{12}$$

The additional terms describe the residual stresses and spontaneous polarization due to domain wall motion and are calculated as follows

$$\{f_e\} = \int_{V^E} [B_u]^{\mathrm{T}}[C]\{\epsilon^{\mathrm{irr}}\}\mathrm{d}V, \qquad \{q_e\} = \int_{V^E} [B_\varphi]^{\mathrm{T}}([e]\{\epsilon^{\mathrm{irr}}\} - \{P^{\mathrm{irr}}\})\mathrm{d}V. \tag{13}$$

Here, the matrices $[B_u]$ and $[B_\varphi]$ relate the nodal variables $\{u\}$ and $\{\varphi\}$ with strain and electric field, in accordance with Eq. (6).

Now, the effective properties of damaged ferroelectric materials are calculated. The constitutive law, as given by Eqs. (3) and (4) is still valid. However, the material constants are modified by the damage. Therefore, a general relation between the volume averages of two piezoelectric field variables Π and Z is considered as

$$\langle Z \rangle = F^\star \langle \Pi \rangle, \tag{14}$$

with $\Pi = (\sigma_{11}, \sigma_{22}, \sigma_{12}, D_1, D_2)^{\mathrm{T}}$, and $Z = (\epsilon_{11}, \epsilon_{22}, 2\epsilon_{12}, -E_1, -E_2)^{\mathrm{T}}$. Here, $F^\star$ is the generalized compliance. Moreover, Eq. (14) can be written in an equivalent constitutive formulation with strain and electric field being independent variables $\langle \Pi \rangle = C^\star \langle Z \rangle$. The average strain and electric field density can be decomposed into two parts $\langle Z \rangle = Z^{\mathrm{M}} + Z^{\mathrm{C}}$ with $Z^{\mathrm{M}} = F^{\mathrm{M}}\Pi^0$ representing the matrix and $Z^{\mathrm{C}} = F^{\mathrm{C}}\Pi^0$ the defect phase. Here, $\langle \Pi \rangle = \Pi^0$ are the external loads. Then, it can be shown that the generalized compliance $F^\star$ as well as $C^\star$ are given as the sum of the generalized compliance of the matrix medium $F^{\mathrm{M}} = [C^{\mathrm{M}}]^{-1}$ and a contribution to be determined through the crack surface deformation F^{C}, i.e. $F^\star = F^{\mathrm{M}} + F^{\mathrm{C}}$. The contribution of micro cracks to the averaged strain and el. field density Z^{C} is given by

$$\epsilon_{ij}^{\mathrm{C}} = \frac{1}{2A} \int_{-a}^{+a} (\Delta u_i n_j + \Delta u_j n_i)\, \mathrm{d}x_1^c, \qquad E_i^{\mathrm{C}} = -\frac{1}{A} \int_{-a}^{+a} \Delta\varphi\, n_i\, \mathrm{d}x_1^c. \tag{15}$$

The calculations are done by applying the so called dilute model where defect interaction is neglected. Jumps of the displacement and the electric potential across crack surfaces are given by

$$\Delta u_M = 2Y_{MN}\sqrt{a^2 - (x_1^c)^2}\,\Pi_{N2}. \tag{16}$$

The latter is drawn from a closed form solution of the piezoelectric Griffith crack problem [3]. This means, that the crack is assumed to be in a flawless matrix medium. Here, Y_{MN} is the Irwin matrix. Note that Eqs. (15) and (16) are given in the coordinate system of a microcrack (x_1^c, x_2^c). After calculating F^C, the material properties in Eqs. (11) and (12) are updated according to

$$C^\star = [(C^{\mathrm{M}})^{-1} + F^{\mathrm{C}}]^{-1}. \tag{17}$$

The influence of damage evolution is governed by a damage parameter $f = 4a^2/A$ which describes the density of microcracks, that is $f = 0$ for a flawless material and $f = 1$ for the full damage. The microcrack initiation is controlled by a mode-I stress intensity factor $K_I = K_{IC}$, where $K_I = \sqrt{\pi a_n}\sigma_I$ and σ_I is the maximal principal stress. Once the criterion is satisfied the microcrack is initiated and the calculation continues with crack growth, such that $a_n = a_0 + n \cdot \Delta a$ and $f_n = f_0 + n \cdot \Delta f$, where a_n is the crack length associated with the damage parameter f_n.

3 Example

The model has been implemented into the commercial FEM-code Abaqus in terms of a user element. In Fig. 2 an analysis of a multilayer actuator is presented, showing (a) polarization vectors after the poling process with $E_{\max} = 5E_c$ and (b) maximal principal stresses. Those are largest close to the electrode tips leading to crack initiation.

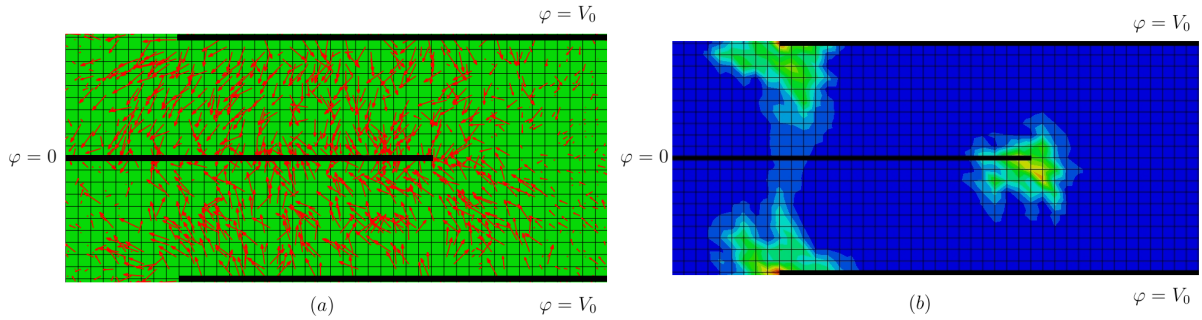

Figure 2: (a) Polarization vectors around electodes inside actuator after poling process. (b) Maximal principal stresses at the electrode tips during polarization process: red color (100 MPa), green color (35 MPa).

REFERENCES

[1] R. Gellmann, A. Ricoeur, E. Merkel, and Z. Wang. Generalized boundary conditions and effective properties in cracked piezoelectric solids, *PAMM*, 13: 225–226, 2013.

[2] S. C. Hwang, C. S. Lynch, and R. M. McMeeking. Ferroelectric/ferroelastic interactions and a polarization switching model, *Acta Metallurgica et Materialia*, 43(5): 2073–2084, 1995.

[3] A. Ricoeur, M. Kuna. Influence of electric fields on the fracture of ferroelectric ceramics, *Journal of the European Ceramic Society*, 23: 1313–1328, 2003

ON CHARACTERIZATION OF THE ELECTRO-MECHANICALLY COUPLED PROPERTIES OF VHB 4910 POLYMER

Mokarram Hossain[1], **Duc Khoi Vu**[1], **and Paul Steinmann**[1]

[1] Chair of Applied Mechanics, Mechanical Engineering, University of Erlangen-Nuremberg
5, Egerland Strasse, Erlangen Germany
e-mail: mokarram.hossain@fau.de

Abstract. *A detailed account on VHB 4910 polymer under application of purely mechanical and electro-mechanically coupled loadings is presented. VHB 4910 is a acrylic type viscoelastic polymer that has potential applications as an electro-active polymer. To see the electro-mechanical coupled effects for all experimental tests presented here, the polymer samples were pre-stretched up to several hundred percent to make them thin enough initially. Then, the pre-stretched samples were subjected to various amount of mechanical as well coupled deformations at different strain rates. All data produced from electro-mechanically coupled tests show that the electric loading has profound effect in the time-dependent behaviour of the electro-active VHB 4910 polymer. The data set from various tests can be used for the identification of electro-viscoelastic parameters for a suitable constitutive model that can capture electro-mechanically coupled behaviours of VHB 4910.*

1 Introduction

Recently, much efforts have been invested in the so-called electronic electro-active polymers (EEAPs) since these can potentially be used in the production of a class of smart materials. In EEAPs, a large displacement mechanical output is produced by the application of an electrostatic excitation. The possibility of the high deformation characteristics is an attractive attribute that has enabled a myriad of potential applications. Therefore, considerable research works have been driven towards the development of constitutive modelling as well as numerical implementation of such material models. EEAPs in actuators are utilized in the form of a thin film that is sandwiched between two compliant electrodes and then exposed to an electric potential difference, which creates Maxwell forces between the electrodes, i.e. a mechanical output is the resultant due to electric stimuli [1,3,5]. VHB 4910 is an acrylic type polymer that can be used in developing EEAP actuators.

Several constitutive modelling approaches both for mechanical and coupled problems in the case of the dielectric VHB elastomer have been proposed in the literature [3,4]. However, very few experimental works can be found in the literature that illustrate the time-dependent dissipative behaviour of the material with simultaneous electric and mechanical loadings. Diaconu et al. [2] studied the electro-mechanical properties of a synthesized polyurethane elastomer film-based polyester. Ask et al. [3] proposed a thermodynamically consistent electro-mechanical coupled finite strain viscoelastic model based on a multiplicative decomposition of the deformation gradient where they used Diaconu et al. [2] data for the identification of the model material parameters as well as for their model validation.

Here we present several standard experimental tests that are frequently utilized for a viscoelastic polymeric material characterization. The experiments were performed on the acrylic type VHB 4910 polymer with and without the application of electric loads. For all cases, the pre-stretched samples were stretched in lateral direction up to several hundred percent deformation to make them thin enough so that the effect of two opposite charged electric loads will be high enough to show their effect on the polymeric material with a pronounced mechanical deformation.

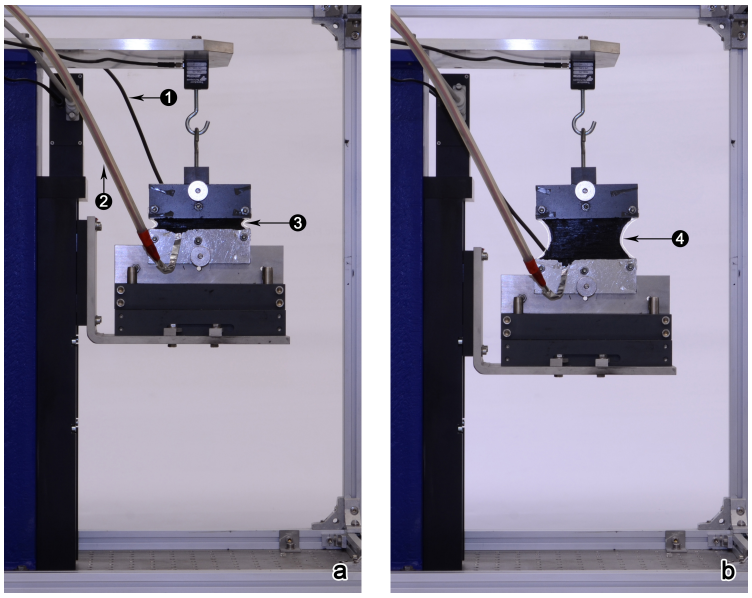

Figure 1: Preparation for electro-mechanical coupled tests: Specimen is hanged from the vertically-mounted load cell by a hook; pre-stretched undeformed sample (**a**); Sample is clamped in-between the clamping plates, deformed geometry (**b**). Legend: **1**. upper cable, **2**. lower cable, **3**. pre-stretched but undeformed specimen, and **4**. pre-stretched and deformed specimen

2 Experimental set-ups

The purely mechanical counterpart of this experimental set-up is described in our previous publication, cf. Hossain et al. [4]. Henceforth, we briefly review the procedure in the case of the electro-mechanical coupled loading. For electric tests, electric connection is set up via two cables that are connected to two metal plates (one at the top and one at the bottom of the clamped specimen) attached to the linear stage, cf. Fig (1). A sample is held at its two ends using two pairs of clamps, see Fig (1), which in turn are mounted on a linear translation stage with the help of a table and a pair of metal hooks. The upper hook is connected to the frame of the linear translation stage through a force transducer. The stretching of the sample is realized by moving up and down the table using the linear translation stage. During each test, the position of the table is recorded at the same time with the signal captured by the force transducer. For the purely mechanical tests as well as tests with electro-mechanical coupled loadings, all tests were conducted either with a constant strain rate as in the case of the cyclic tests or at a predefined deformation level in the case of the stress relaxation tests. The resulting force history was measured with the force transducer. The transducer is connected to a PC LabView system for the data acquisition. All forces for required deformations in the lateral direction of the two hundred percent pre-stretched sample are calculated in Newton (N).

3 Electro-mechanical tests

In the following sections loading-unloading tests and multi-step relaxation tests will be presented with and without the application of electric loads. In the case of the electric load, the aim was to apply maximum voltage, e.g. ten kilovolt (kV) on the pre-stretched sample in order to observe large deformation. However, in this particular situation we can apply maximum five kilovolt electric load on a two hundred percent pre-stretched sample.

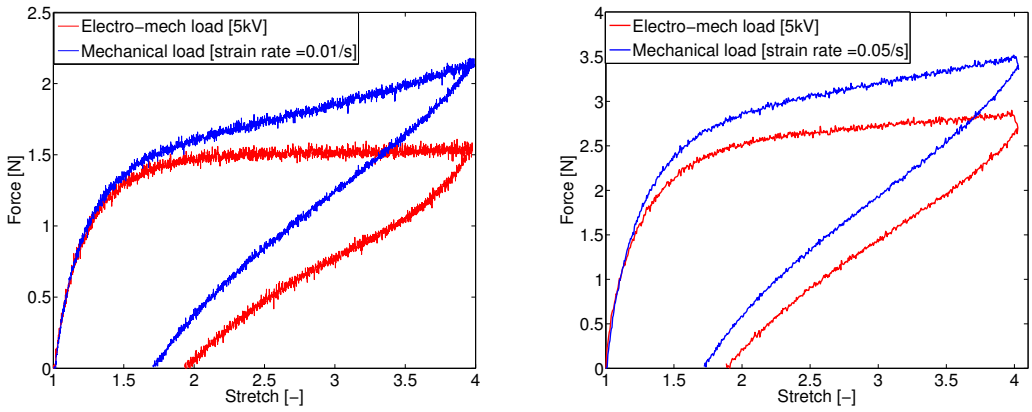

Figure 2: Loading-unloading test: Force (N) vs deformation on a two hundred percent pre-strained sample. The strain rates were $0.01s^{-1}$ (left) and $0.05s^{-1}$ for mechanical deformations as well as for electro-mechanical loads while a five kilovolt electric load was applied in the case of coupled tests. Samples were deformed by a three hundred percent deformation in the lateral direction of loading

Loading-unloading cyclic test is a typical experiment for the characterization of a viscoelastic polymeric material behaviour. In the case of electro-mechanical coupled loading-unloading tests, the electric loading was applied from the beginning of the deformation to the end of the deformation, i.e. in a complete loading-unloading cycle. We had observed that the effect of the electric load can only be sufficiently visible if the prestrained sample was elongated starting from a three hundred percent mechanical lateral deformation during the loading path. All tests were carried out at two selective strain rates $0.01s^{-1}$ and $0.05s^{-1}$. The obtained results are presented in Fig (2) in terms of required force (N) versus stretch.

For electro-mechanical coupled tests, the multi-step relaxation experiments can be used to see the drop of the force due to an electric load in several consecutive load steps. In the first step-wise elongation, deformations of a two hundred and fifty percent, cf. Fig (3), were applied quickly to make the sample thin enough to get electric effect. Simultaneously, the electric load was switched on from the beginning until completion of the entire test. We tried with other smaller amount of mechanical deformations, e.g. a one hundred percent or even a two hundred percent deformation but the applied deformations were not enough for the electric load to affect the polymeric samples. Therefore, we had to go for a higher amount of deformation in the first step load. After that another deformation of one hundred percent was applied in the second step of loading with the same velocity as in the first case. We can not go further step-wise deformation because samples either broke down during a mechanical load or short-circuited during the application of an electric load. It can be observed that at the end of the first step stretching with a holding period of ten minutes, the stress did not converge to an almost constant state. This agrees with earlier observations that that a thirty minute holding

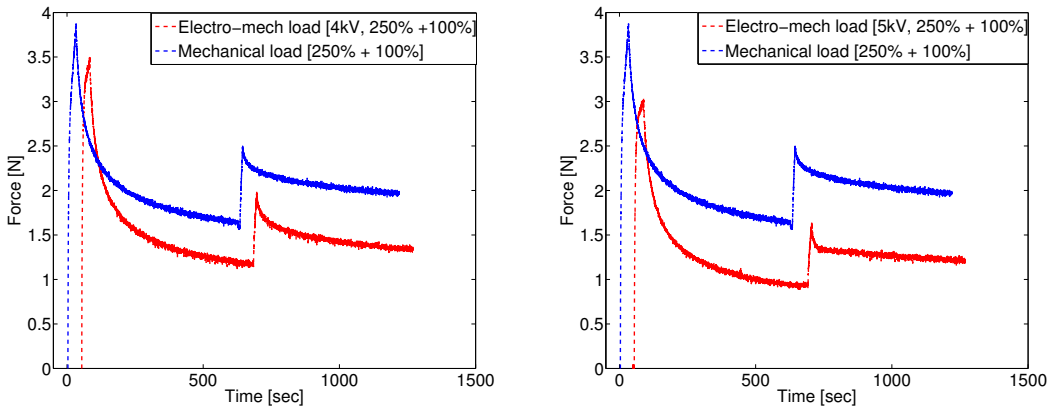

Figure 3: Multi-step relaxation test: Coupled electro-mechanical load with a four (left) and a five kilovolt electric loads were applied in a two step deformation on a two hundred percent pre-stretched sample. The holding period was ten minutes while the speed for the sudden deformation was 1 mms^{-1}.

time is required for a complete relaxation. However, we can not wait for more than ten minutes since the thirty minutes holding period for the relaxation experiments was not suitable here as the sample broke down before it reached the desired time span. The difference of the force between the mechanical and the electro-mechanical cases has a thirty percent drop in the first step relaxation but very little in the second phase. The reason might be that samples were affected slightly in their thickness in the case of the second step deformation.

4 Conclusion

The data produced from several loading-unloading tests and multi-step relaxation tests show that the electric loading has profound effect in the time-dependent behaviour of the electro-active VHB 4910 polymer. The data set from loading-unloading cyclic tests can be used to identify electro-elastic parameters while multi-step relaxation data would be useful for the identification of electro-viscoelastic parameters for a suitable constitutive model that can capture electro-mechanically coupled behaviours of VHB 4910 polymer.

REFERENCES

[1] J. Qiang, H. Chen and B. Li. Experimental study on the dielectric properties of polyacrylate dielectric elastomer, *Smart Material Structures*, 21: 1-9,2012.

[2] I. Diaconu, D.O. Dorohoi and C. Ciobanu. Eletromechanical response of polyurethane films with different thickness, *Romanian Journal of Physics*, 53(1-2):91-97,2008.

[3] A. Ask, A. Menzel and M. Ristinma, Electrostriction in electro-viscoelastic polymers, *Mechanics of Materials* 50:9-21, 2012

[4] M. Hossain, D. K. Vu,and P. Steinmann. Experimental study and numerical modelling of VHB 4910 polymer, *Computational Materials Science* 59: 65-74, 2012

[5] M. Wissler, E. Mazza, Mechanical behaviour of an acrylic elastomer used in dielectric elastomer actuators, *Sensors and Actuators A* 134: 494-504, 2007

MICROSCOPIC SIMULATION OF THERMALLY-INDUCED SECOND ORDER EIGENSTRESSES IN AL-SI ALLOYS

Matthias Kabel[1], **Heiko Andrä**[1], **and Sarah Staub**[1]

[1] Fraunhofer Institute for Industrial Mathematics (ITWM), Department of Flow and Material Simulation
Fraunhofer-Platz 1, 67663 Kaiserslautern, Germany
e-mail: matthias.kabel@itwm.fraunhofer.de

Abstract. *Due to the different coefficients of thermal expansion of aluminium and silicium high residual stresses of second order occur in AlSi alloys depending on the solidification rate during the molding process. In products as for example crank cases made of AlSi alloys these residual stresses may cause microcracks. In the work at hand measurements of the eigenstresses in the single phases performed via neutron diffractometry are compared to numerical simulations for different cooling rates. To this end different multiphase-models are presented and compared which consider the α aluminium and the eutectic phase or the α aluminium, the eutectic aluminium and the silicium particles. The presented model is able to predict the residual stresses in the single phases within an elastoplastic framework. The influence of the cooling rate onto the microscopic setting (dendrites geometry and amount of eutectic phase) and thus the eigenstresses is studied. The numerical calculations are carried out directly on segmented synchrotron images or on stochastic geometry models with the Fourier method.*

1 Introduction

The Fourier method for the calculation of full field solutions was first proposed by Moulinec and Suquet in the middle of the 1990s [6]. This method applies the Fast Fourier Transformation (FFT) to solve integral equations of Lippmann-Schwinger type [12, 3]. Since no meshing is required and the assembly of the linear system is avoided, the memory needed for solving the problem is significantly reduced compared with other methods. This approach became popular in recent years primarily due to the striking speed of available FFT implementations [2], in particular for real world industrial applications [1]. Improvements of the original Fourier method for dealing with nonlinear thermoelastic problems at infinitesimal strains can be found in [7, 4, 8, 11].

Microstructures of cast aluminium alloys with large secondary dendrite arm spacing (SDAS) are characterized by an extremely inhomogeneous distribution of inclusions. Therefore, traditional single-step homogenization methods (FEM, Voronoi cell FEM) are not suitable for this type of microstructures due to the size of the representative volume element (RVE) and dual-stage nested homogenization methods are proposed [10] even for two-dimensional RVE's. By using the FFT-based solver we overcome the size limitation of the RVE's. The Fourier method enables a single-step homogenization for realistic three-dimensional RVE's of AlSi alloys.

2 Thermoelasticity

For the sake of simplicity, we omit volume forces and plastic (or other inelastic) strains in the following derivation of the governing equations. In the linear approximation thermal expansion

is governed by the equation

$$\sigma(x) = C(x) : (\epsilon(x) - \theta\alpha(x)),$$

where $\theta = T - T_0$ is the change in temperature T measured from some constant base temperature T_0, $\epsilon(x)$ and $\sigma(x)$ are the strain and stress fields, $C(x)$ is the stiffness tensor field, and $\alpha(x)$ is the symmetric second-order tensor field of thermal expansion [5]. $A(x) = -C(x)\alpha(x)$ is the thermal stress (eigenstress) tensor field. The (static) equilibrium condition without volume forces is given by

$$\operatorname{div}\sigma = 0.$$

Combining the constitutive equation with the equilibrium condition on a representative volume element (RVE) with periodic boundary conditions gives a set of explicit field equations for the determination of the periodic displacement field u which is defined by

$$\epsilon(x) = E + (\operatorname{grad} u(x) + (\operatorname{grad} u(x))^T)/2.$$

Proper boundary conditions have to be defined by prescribing the average strain E and the temperature change θ.

3 Lippmann-Schwinger equation

By introducing a reference material with homogeneous stiffness C^0 and thermal stress A^0 and the polarization

$$\tau(x) = \left(C(x) - C^0\right) : \epsilon(x) + \theta(A(x) - A^0),$$

the constitutive equation can be transformed as follows

$$\sigma(x) = C^0 : \epsilon(x) + \theta A^0 + \tau(x).$$

For known residual stresses $\tau(x)$ the solution of $\operatorname{div}\sigma(x) = 0$ can be expressed by using the nonlocal elastic Green operator Γ^0 for strains associated with the reference Material C^0 [3],

$$\epsilon(x) = E - \left(\Gamma^0 * \tau\right)(x),$$

where the convolution is defined by

$$\left(\Gamma^0 * \tau\right)(x) = \int_\Omega \Gamma^0(x - y) : \tau(y) dy.$$

By combining the last equations one obtains the Lippmann-Schwinger equation:

$$(I + B_\epsilon)\epsilon := \epsilon + \Gamma^0 * \left(\left(C - C^0\right) : \epsilon + \theta(A - A^0)\right) = E.$$

4 Numerical algorithm

The Lippmann-Schwinger equation can be iteratively solved using the Neumann series expansion for inverting the operator $(I + B_\epsilon)$. To be more precise, the iterates of the local strain resp. stress read

$$\begin{aligned} \epsilon^0 &= E, \\ \epsilon^{n+1} &= -B_\epsilon \epsilon^n + E. \end{aligned}$$

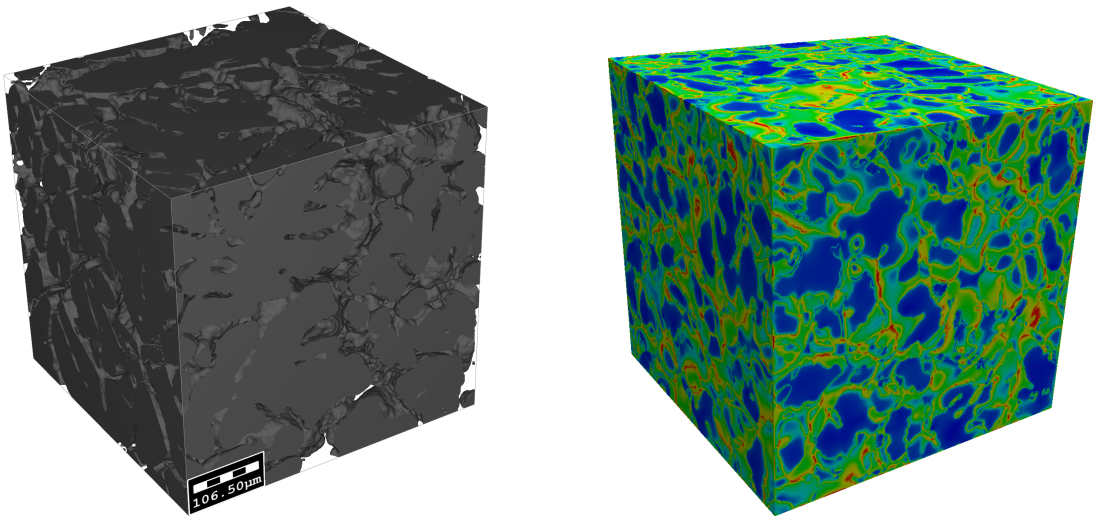

a) b)

Figure 1: a) Two-phase model of AlSi7. b) Residual stresses of second order

These iterates can be efficiently calculated in four simple steps using FFT by the so called basic scheme [4]:

$$\begin{aligned} \tau &= (C - C^0) : \epsilon^n + \theta(A - A^0), \\ \hat{\tau} &= \mathrm{FFT}(\tau), \\ \hat{\eta} &= -\hat{\Gamma}^0 : \hat{\tau}, \quad \hat{\eta}(0) = E, \\ \epsilon^{n+1} &= \mathrm{FFT}^{-1}(\hat{\eta}). \end{aligned}$$

Explicit expressions for the Fourier coefficients $\hat{\Gamma}^0$ of the Green operator can be found in [9] for different types of anisotropy.

5 Numerical results

In our presentation we consider RVE's (see Fig. 1a) of AlSi microstructure models for varying solidification rates. In the numerical simulation we take into account the averaged hydrostatic stress in the Si particles of the eutectic phase which was measured by neutron diffractometry. Therewith we compute the local and averaged residual stresses (and strains) in all phases of the AlSi microstructure (see Fig. 1b). The magnitude of the so-called residual stresses of second order are one essential reason for damage effects and crack initiation in AlSi alloys.

6 Acknowledgement

This study is part of a program supported by the Bavarian Research Foundation.

REFERENCES

[1] H. Andrä, N. Combaret, J. Dvorkin, E. Glatt, J. Han, M. Kabel, Y. Keehm, F. Krzikalla, M. Lee, C. Madonna, M. Marsh, T. Mukerji, E. H. Saenger, R. Sain, N. Saxena, S. Ricker, A. Wiegmann, and X. Zhan. Digital rock physics benchmarks - Part II: Computing effective properties. *Computers & Geosciences*, 50:33–43, 2013.

[2] S.G. Johnson and M. Frigo. A modified split-radix fft with fewer arithmetic operations. *Signal Processing, IEEE Transactions on*, 55(1):111–119, 2007.

[3] E. Kröner. Bounds for effective elastic moduli of disordered materials. *Journal of the Mechanics and Physics of Solids*, 25(2):137–155, 1977.

[4] J. C. Michel, H. Moulinec, and P. Suquet. A computational scheme for linear and non-linear composites with arbitrary phase contrast. *International Journal for Numerical Methods in Engineering*, 52(12):139–160, 2001.

[5] G. W. Milton. *The Theory of Composites*. Cambridge University Press, 2002.

[6] H. Moulinec and P. Suquet. A fast numerical method for computing the linear and non-linear mechanical properties of composites. *Comptes rendus de lAcadmie des sciences. Srie II, Mcanique, physique, chimie, astronomie*, 318(11):1417–1423, 1994.

[7] H. Moulinec and P. Suquet. A numerical method for computing the overall response of nonlinear composites with complex microstructure. *Computer Methods in Applied Mechanics and Engineering*, 157:69–94, 1998.

[8] H. Moulinec and P. Suquet. Comparison of fft-based methods for computing the response of composites with highly contrasted mechanical properties. *Physica B: Condensed Matter*, 338(1–4):58–60, 2003.

[9] T. Mura. *Micromechanics of Defects in Solids*. Martinus Nijhoff Publishers, Dordrecht, 1987.

[10] D. Paquet, P. Dondeti, and S. Ghosh. Dual-stage nested homogenization for rate- dependant anisotropic elasto-plasticity model of dendritic cast aluminum alloys. *Int. J. Plasticity*, 27:1677–1701, 2011.

[11] V. Vinogradov and G. W. Milton. An accelerated FFT algorithm for thermoelastic and non-linear composites, *Int. J. Numer. Meth. Engng*, 76: 1678–1695, 2008.

[12] R. Zeller and P. H. Dederichs. Elastic constants of polycrystals. *physica status solidi (b)*, 55(2):831–842, 1973.

MODELING THE INTERACTION OF LITHIUM INSERTION AND MECHANICS IN ELECTRODES OF LITHIUM ION BATTERIES

Magalie Huttin, Julia Ott, Ann-Christin Walk, and Marc Kamlah[1]

[1] Institute for Applied Materials, Karlsruhe Institute of Technology
Hermann von Helmholtz-Platz 1, 76344 Eggenstein-Leopoldshafen, Germany
e-mail: marc.kamlah@kit.edu

Abstract. *In this talk, we consider the interaction of lithium insertion and mechanical stresses in electrode particles and electrodes of lithium ion batteries. First, we consider a phase-field model employing the Cahn-Hilliard equation to study the effect of phase changes on the stresses occuring in electrode particles made of lithium manganese oxide spinel. Second, this theory is implemented in a finite deformation framework, and the consequences are discussed. Third, with the help of the discrete element method, the impact of mechanical effects on the transport properties in a porous electrode are investigated.*

1 Introduction

The original work summarized in this abstract has been published in references [1-5]. For further reading we refer to the references given in these publications.

The electrochemical processes in the electrodes of lithium ion batteries (LIB) are coupled to mechanical properties. On the one hand, insertion of lithium into the host material leads to strains and, as a consequence, mechanical stresses are induced. Depending on the host material, very large deformations up to a few 100% may occur during lithium insertion. On the other hand, for thermodynamical reasons, there is a contribution of mechanical stresses to the driving force for diffusion of lithium in the host material. During lithium insertion, most of the host materials show non-ideal effects in the form of phase changes. An important example of current candidates is lithium manganese oxide spinel ($Li_xMn_2O_4$ or LMO).

As diffusion of lithium in the host material is the process limiting cell power, the electrodes usually are composed of small particles. Composition and microstructure of electrodes in chemical power sources in general play a critical role for high electrode performance of the cells. Hence, for optimization it is crucial to understand how effective transport properties improve cell performance and how they are affected by the mechanical state.

2 Phase-field modeling of the interaction of lithium insertion and mechanical stresses in LMO electrode particles

Many cathodic materials in lithium ion batteries show capacity fade due to particle crackings, especially cathodes made of LMO particles exhibit, even at low applied charge and discharge current, mechanical failure. This indicates that large stresses arise in the particle. One possible origin for such large stresses is the occurrence of phase segregation, for which we account by means of a phase-field model coupled to mechanics. Using this model, both the equilibrium and dynamical behavior of the particle can be analyzed [1,3]. In a first step, we use a spherically symmetric particle model (so-called core-shell-scenario). Fig. 1 summarizes results for

dynamical loading. The curves shown there are obtained during lithium extraction and for two different radii of the particle. Bigger applied C-rate, i.e. loading rates, values are represented in the inset. It can be seen that phase changes lead to severe stresses. And in contrast to the stresses caused by the purely rate induced gradients in the commonly applied dilute solution approach, very high stresses are present in the phase-field model even for arbitrary low loading rates. This observation has recently been confirmed by experiments at IAM-WBM of KIT.

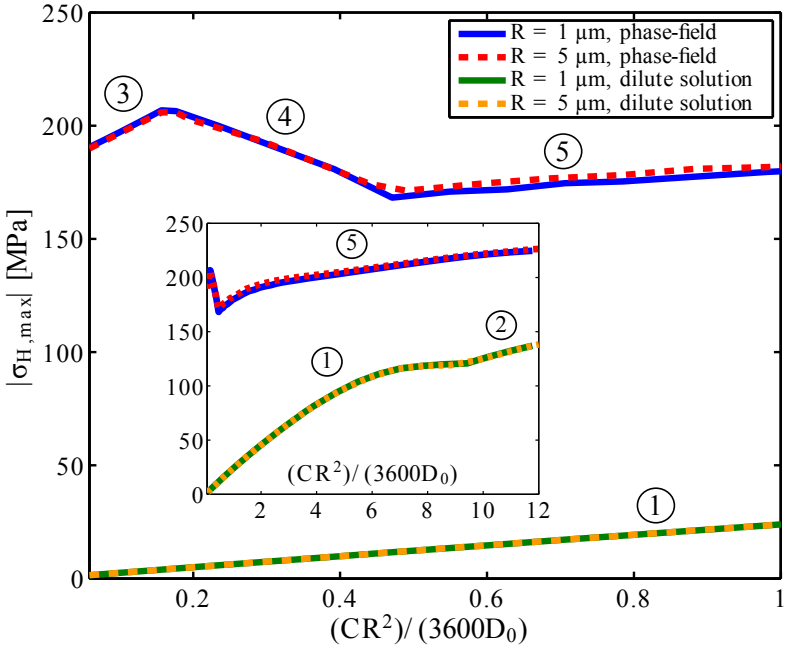

Figure 1: Maximum hydrostatic stress reached using the phase-field model and the dilute solution model [1].

3 Comparision of small and finite deformation formulation of the phase-field model

In this section, a comparison will be made for a small and a large deformation implementation of the theory introduced in the previous section [2,4]. We study charging processes close to equilibrium, and we will look at the influence of certain material parameters. As an example, see the effect of a variation of Young's modulus in Fig. 2. It can clearly be seen that the finite deformation formulation of the theory leads to less pronounced gradients and to a reduced concentration difference between the regions of different phase state.

In particular, for values of Young's modulus beyond a certain threshold, phase segregation is surpressed. For such values, the energetical cost due to the elastic strain energy caused by the strain mismatch between adjacent phases becomes too large, and the system stays in a homogenous state even though it is in the spinodal region of average concentration.

4 DEM study on the effect of the mechanical state on the electric transport in an porous electrode

In this section, we study with the help of the discrete element method the impact of mechanical effects on the transport properties in a porous electrode [5]. To be specific a mixture having electrical conducting spherical particles describes the granular electrode structure, one phase representing the intercalation material LMO and the other carbon black. To determine the per-

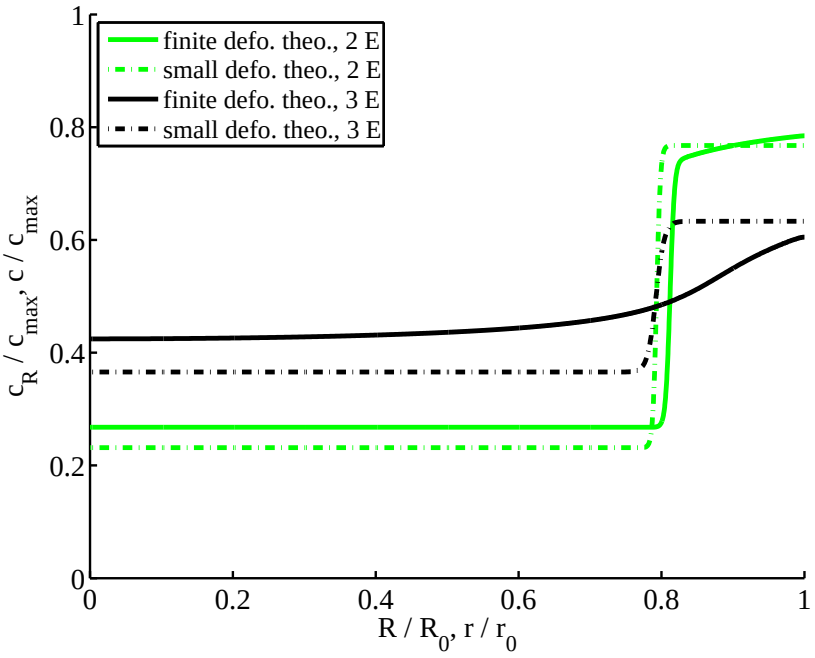

Figure 2: Concentration profiles for increasing values of Young's modulus [2].

colation threshold for binary mixtures a tracking algorithm (Hoshen-Kopelman) was adapted for non-lattice topologies with periodic boundaries. Based on that, a network analysis method is implemented to determine the effective conductivity of various structures.

In LIB, intercalation processes lead to volume change and therefore internal stresses. To investigate this, the methods mentioned above for determination of conductivity were combined with discrete element modeling (DEM), which allows simulation of interparticular forces and rearrangements in granular structures during loading to determine the impact of mechanical stress on transport properties. In addition, the effect of the calendering process during manufacturing of an electrode in order to increase the density is simulated.

Fig. 3 shows the change in conductivity for carbon black during calendering and the subsequent intercalation process in a LMO electrode. In the un-calendered state, the carbon black phase is not percolated, and, consequently there is no electronic conductivity in this phase and the electronic conductivity of the electrode is dominated by the low electronic conductivity of the active material. After calendering, the carbon black phase is now percolated, and one can clearly see the anisotropy in conductivity with the highest conductivity in the direction of the applied mechanical load during calendering. A subsequent intercalation process leads to volumentric swelling of the active material particles (LMO) of up to 6%. During this process, the contact forces between particles increase, thus leading to an even improved electronic conductivity.

REFERENCES

[1] M. Huttin and M. Kamlah. Phase-field modeling of stress generation in electrode particles of lithium ion batteries, *Applied Physics Letters*, 101: 133902, 2012.

[2] A.-C. Walk, M. Huttin, and M. Kamlah. Comparison of a Phase-Field Model for Intercalation Induced Stresses In Electrode Particles Of Lithium Ion Batteries for Small and Finite

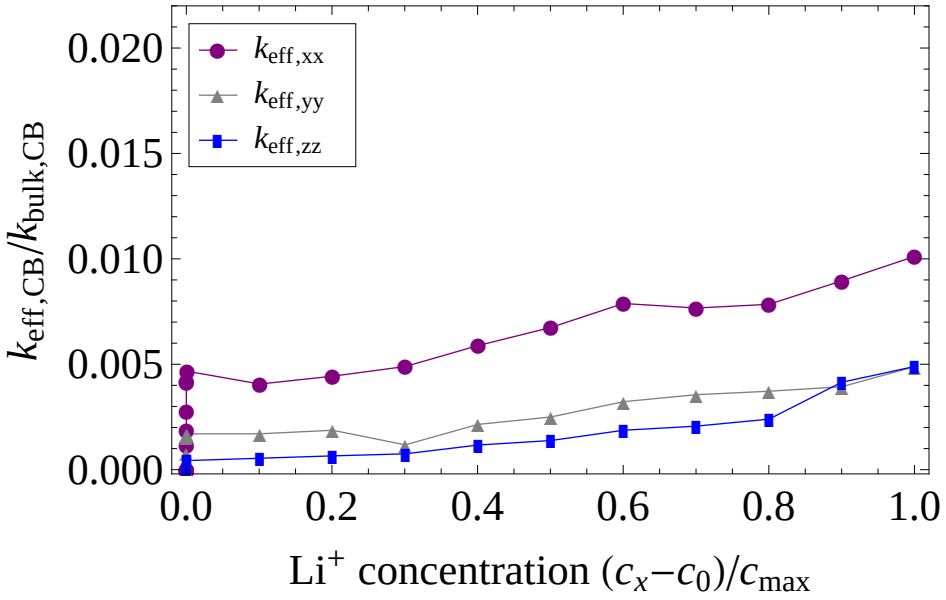

Figure 3: Change in conductivity for carbon black during calendering and the subsequent intercalation process in a LMO electrode [5].

Deformation Theory, *European Journal of Mechanics - A/Solids*, accepted, 2013.

[3] M. Huttin. Phase-field modeling of the influence of mechanical stresses on charging and discharging processes in lithium ion batteries. Dissertation thesis, Karlsruhe Institute of Technology, 2014.

[4] A.-C. Walk. Phasenfeldmodellierung von interkalationsinduzierten Spannungen in Elektrodenpartikeln von Lithium-Ionen-Batterien bei großen Deformationen. Diploma thesis, Karlsruhe Institute of Technology, 2013.

[5] J. Ott, B. Völker, Y. Gan, R. M. McMeeking, M. Kamlah. A micromechanical model for effective conductivity in granular electrode structures. *Acta Mechachnica Sinica*, 29: 682-698, 2013.

A PHASE FIELD MODEL FOR NEMATIC ELASTOMERS: CONTINUUM MECHANICAL FORMULATION AND FINITE ELEMENT IMPLEMENTATION

Marc-André Keip[1] **and Kaushik Bhattacharya**[2]

[1] Institute of Applied Mechanics (CE), Chair I, University of Stuttgart
Pfaffenwaldring 7, 70569 Stuttgart, Germany
e-mail: keip@mechbau.uni-stuttgart.de

[2] Division of Engineering and Applied Science, California Institute of Technology
1200 E California Blvd, Pasadena, CA 91125, USA
e-mail: bhatta@caltech.edu

Abstract. *Liquid crystal elastomers combine the elastic properties of rubber with the orientational properties of liquid crystals. Due to their unique properties they have attracted considerable scientific attention during the last years. Amongst the various types of liquid crystal elastomers, nematic elastomers are one special class. These undergo a phase transition from a high-temperature isotropic state to a low-temperature nematic state, which is accompanied by rather large deformations. As a consequence of the phase transition the elastomer may develop domains which consist of homogeneously oriented nematic mesogens. The goal of this talk is to discuss a phase-field model for the continuum mechanical description of nematic elastomers. The model will be implemented into the finite element method and applied to the simulation of domain evolution under specified initial boundary conditions.*

1 Introduction

Liquid crystal elastomers (LCE) have attracted considerable scientific attention recently. LCEs are soft materials and they mechanically react on externally applied fields like, for example, temperature, electric and magnetic fields, as well as light. They do so with comparably large deformations, which makes them a prototype material for soft actuators. Due to their unique properties they may find application in the area of, for instance, micro-robotics and medicine technology [6].

As the name implies, liquid crystal elastomers combine features of liquid crystals and elastomers at the same time: they have the elastic properties of rubber and the orientational properties of liquid crystals. They are made from liquid crystals by cross-linking their polymeric chains. A comprehensive textbook on liquid crystal elastomers is given by the fundamental work from Mark Warner and Eugene Terentjev [12]. The interested reader may also be referred to the classic on liquid crystals from Pierre-Gilles de Gennes and Jacques Prost [5].

A special class of LCEs is given by *nematic elastomers*, which are characterized by a phase transition between an isotropic and an anisotropic state. The isotropic state exists at high temperatures and shows a random distribution of nematic mesogens (mesogens are quasi-rigid and mainly rod-like particles that are attached to the polymer chain). When cooled down below a certain transition temperature, the elastomer undergoes an isotropic-to-nematic phase transition.

This phase transition is accompanied by the alignment of adjacent nematic mesogens. Here it should be noticed that the properties of nematics depend significantly on their cross-linking history, where one distinguishes between cross-linking the polymer in the high-symmetry isotropic and cross-linking it in the low-symmetry nematic state. This production history influences their elastic behavior, which is characterized by a unique phenomenon given by soft (or semi-soft) elasticity [11]. Theoretical studies on the effective elastic response of polydomain nematics for both cross-linking histories have been conducted in [1].
There exist numerous works on theory and experiments of LCEs in the literature. Fundamental experimental studies were, for example, performed by Finkelmann and co-workers [8]. Micromechanically motivated free energies for the description of nematic elastomers were presented in the context of a so-called neo-classical theory [2]. Mathematical issues have been explored, for example, in the framework of relaxation theories [4,7]. Works on phase-field modeling of nematic elastomers are given by, for example, [10,9].

2 Nematic phase transition, order parameters, and Landau-de Gennes theory

As mentioned above, nematic elastomers are characterized by a phase transition. Figure 1 shows a sketch of a nematic elastomer microstructure above and below the isotropic-to-nematic phase transition temperature.

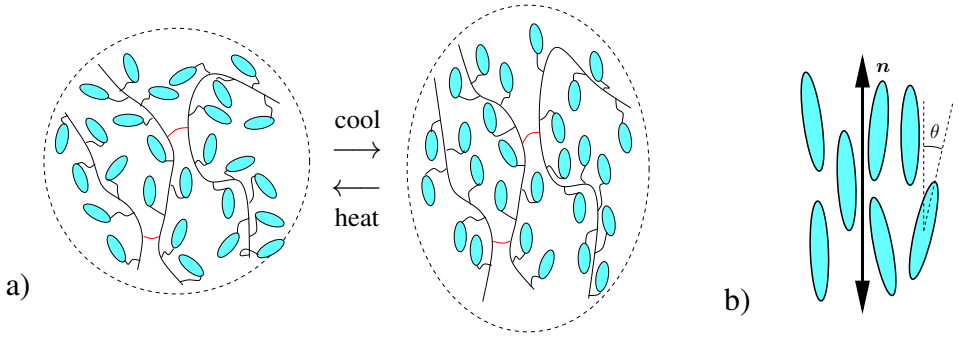

Figure 1: Phase transition of nematic elastomers: a) When the elastomer is cooled down below a critical temperature it undergoes an isotropic-to-nematic phase transition. As a result the order of nematic mesogens changes. b) Below the transition temperature the mesogens align in a homogeneous direction. This direction can be described by the nematic director $\boldsymbol{n}$.

In Fig. 1a we see cross-linked polymer chains with attached mesogens, which order in a homogeneous direction when they are cooled down below a critical temperatue. The mean direction of order is usually described by the *nematic director* $\boldsymbol{n}$ that has unit length $\|\boldsymbol{n}\| = 1$. Note that, due to the symmetry in the nematic phase, the states $+\boldsymbol{n}$ and $-\boldsymbol{n}$ are indistinguishable. This is why the nematic director is often visualized by a double-headed vector, see Fig. 1b. Next to the direction of nematic order we may want to quantify the amount of order in this direction. This can be done through the scalar nematic order parameter S

$$S = \langle P_2(\cos\theta)\rangle = \langle \frac{3}{2}\cos^2\theta - \frac{1}{2}\rangle. \tag{1}$$

Here, θ is the inclination angle between the individual mesogens and the nematic director, and $\langle\bullet\rangle$ defines the volume average. Due to the above mentioned symmetry reasons the order parameter S is derived from a Legendre polynomial of order 2, for a detailed discussion see [12],

page 11. As a consequence we may distinguish, for example, three extreme cases of order. First, when $S = 1$, all mesogens are perfectly aligned and we thus have perfect nematicity. Second, when $S = 0$, the mesogens are randomly oriented in space, so that the elastomer is isotropic. Third, when $S = -1/2$, all mesogens are oriented perpendicular to the nematic director and thus decribe a plane ortogonal to $\boldsymbol{n}$.
A combination of the vectorial order parameter $\boldsymbol{n}$ and the scalar order parameter S is given by the *Landau-de Gennes* order parameter $\boldsymbol{Q}$, which is a tensor of second order. It is defined as traceless tensor by

$$\boldsymbol{Q} := \frac{3}{2}\, S \left(\boldsymbol{n} \otimes \boldsymbol{n} - \frac{1}{3} \boldsymbol{1} \right). \tag{2}$$

This order parameter is the fundamental ingredient of the phase-transition theory by *de Gennes*. The *Landau-de Gennes* free energy is given as a polynomial of the nematic order tensor $\boldsymbol{Q}$ as

$$\psi^{\mathrm{Q}}_{\mathrm{LdG}} = \frac{1}{3}\, A\, \mathrm{tr}(\boldsymbol{Q} \cdot \boldsymbol{Q}) - \frac{4}{9}\, B\, \mathrm{tr}(\boldsymbol{Q} \cdot \boldsymbol{Q} \cdot \boldsymbol{Q}) + \frac{2}{9}\, C\, \mathrm{tr}(\boldsymbol{Q} \cdot \boldsymbol{Q} \cdot \boldsymbol{Q} \cdot \boldsymbol{Q}) + ... \tag{3}$$

However, taking into account the definition of the order parameter $\boldsymbol{Q}$ in (2), this polynomial can be reformulated to a function of the scalar nematic order parameter S only:

$$\psi^{\mathrm{S}}_{\mathrm{LdG}} = \frac{1}{2}\, A\, S^2 - \frac{1}{3}\, B\, S^3 + \frac{1}{4}\, C\, S^4 + ... \,. \tag{4}$$

The individual coefficients A, B, and C can be obtained from experiments, see, for example, [3], or [12], page 18.

3 Phase field model for nematic elastomers

In order to provide a continuum model for the description of nematic elastomers we formulate a potential energy that comprises contributions from liquid crystal and elastic effects. The energies associated to the liquid crystalline behavior are given by a part that models the phase transition ψ_{LdG}, see (3,4), and a furher part given by a suitable gradient energy ψ_{grad} formulated in terms of the order parameter. The elastic part will be given by a mechanical energy ψ_{mech}. Consequently, the complete free energy is assumed to have the additive form

$$\psi = \psi_{\mathrm{mech}} + \psi_{\mathrm{LdG}} + \psi_{\mathrm{grad}}. \tag{5}$$

The first part defines the purely elastic part of the energy and can be given by one of the neo-classical Warner-Terentjev energies derived in [2]. In detail, we choose for the isochoric part of the elastic energy

$$\psi^{\mathrm{iso}}_{\mathrm{WT}} = \frac{1}{2}\mu \left[\mathrm{tr} \left(\boldsymbol{F}^T \cdot \boldsymbol{l}^{-1} \cdot \boldsymbol{F} \right) - 3 \right] \tag{6}$$

where $\boldsymbol{F}$ is the deformation gradient and $\boldsymbol{l}^{-1}$ is the inverse of the *step-length tensor* $\boldsymbol{l}$. In [1], an explicit version of the step-length tensor is given as

$$\boldsymbol{l} = r^{-1/3} \left[\boldsymbol{1} + (r-1) \boldsymbol{n} \otimes \boldsymbol{n} \right] \quad \text{so that} \quad \boldsymbol{l}^{-1} = r^{1/3} \left[\boldsymbol{1} + \left(r^{-1} - 1 \right) \boldsymbol{n} \otimes \boldsymbol{n} \right], \tag{7}$$

with $\det \boldsymbol{l} = 1$. The scalar r denotes the *relative step length* and is given as a function of the nematic order parameter S by $r = \frac{1+2\,S}{1-S}$. As complete elastic energy we use a compressible version of (6), so that we define

$$\psi_{\mathrm{mech}} := \psi^{\mathrm{iso}}_{\mathrm{WT}} - \mu \ln J - \frac{1}{4}\, \lambda \left(J^2 - 1 \right) - \frac{1}{2}\, \lambda \ln J. \tag{8}$$

In order to complete the material model we use the equivalent Landau-de Gennes energies ψ_{LdG} given in (3) and (4), respectively, as well as a suitable gradient term ψ_{grad} formulated as function of the gradient of the order parameter. The fundamental equations to be solved are then the balance of momentum as well as the associated evolution equation of the order parameter. This will be accomplished by numerical implementation into a finite element framework.

REFERENCES

[1] J. S. Biggins, M. Warner & K. Bhattacharya. Elasticity of Polydomain Liquid Crystal Elastomers, *Journal of the Mechanics and Physics of Solids*, 60: 573–590, 2012.

[2] P. Bladon, E. M. Terentjev & M. Warner. Transitions and Instabilities in Liquid-Crystal Elastomers, *Physical Review E*, 47: 3838–3840, 1993.

[3] H. J. Coles. Laser and electric field induced birefringence studies on the cyanobiphenyl homologues, *Molecular Crystals and Liquid Crystals* 49(3): 67–74, 1978.

[4] S. Conti, A. DeSimone, and G. Dolzmann. Soft elastic response of stretched sheets of nematic elastomers: a numerical study, *Journal of the Mechanics and Physics of Solids*, 50(7): 1431–1451, 2002.

[5] P. G. de Gennes and J. Prost: *The Physics of Liquid Crystals*, Second Edition, vol. 83 of *International Series of Monographs on Physics*, Clarendon Press, 1995.

[6] W. H. de Jeu, editor: *Liquid Crystal Elastomers: Materials and Applications*, vol. 250 of *Advances in Polymer Science*, Springer, 2012.

[7] A. DeSimone and G. Dolzmann. Macroscopic Response of Nematic Elastomers via Relaxation of a Class of SO(3)-Invariant Energies, *Archive for Rational Mechanics and Analysis*, 161(3): 181–204, 2002.

[8] J. Küpfer and H. Finkelmann. Nematic liquid single crystal elastomers, *Die Makromolekulare Chemie, Rapid Communications*, 12(12): 717–726, 1991.

[9] W. S. Oates and H. Wang. A new approach to modeling liquid crystal elastomers using phase field methods, *Modelling and Simulation in Materials Science and Engineering*, 17(6): 064004, 2009.

[10] N. Uchida and A. Onuki. Elastic interactions in nematic elastomers and gels, *Europhysics Letters*, 45(3): 341–347, 1999

[11] K. Urayama, E. Kohmon, M. Kojima & T. Takigawa: Polydomain–Monodomain Transition of Randomly Disordered Nematic Elastomers with Different Cross-Linking Histories. *Macromolecules*, 42: 4084–4089, 2009.

[12] M. Warner & E. M. Terentjev. *Liquid Crystal Elastomers*, vol. 120 of *International Series of Monographs on Physics*, Oxford University Press, 2003.

MODELING OF MAGNETOELASTIC NANOSTRUCTURES WITH A FULLY COUPLED MECHANICAL-MICROMAGNETIC MODEL

Scott M. Keller, Cheng-Yen Liang, and Gregory P. Carman

Translational Applications of Nanoscale Multiferroic Systems TANMS, Department of Mechanical and Aerospace Engineering, University of California, Los Angeles, California 90095, USA
email: Scott Keller: s.keller@verizon.net, Cheng-Yen Liang: liang1982@ucla.edu , Greg Carman: carman@seas.ucla.edu

Abstract: *Micromagnetic simulations of magnetoelastic nanostructures traditionally rely on either the Stoner-Wohlfarth model or the Landau-Lifshitz-Gilbert LLG model assuming uniform strain (and/or assuming uniform magnetization). While the uniform strain assumption is reasonable when modeling magnetoelastic thin films, this constant strain approach becomes increasingly inaccurate for smaller in-plane nanoscale structures. This paper presents analytical work verified with experimental data to significantly improve simulation of finite structures by fully coupling LLG with elastodynamics, i.e. the partial differential equations are intrinsically coupled.*

1 INTRODUCTION

Electrical control of ferromagnetic elements represents an important and emerging area of study in multiferroics. Magnetic control has conventionally been accomplished using an applied magnetic field rather than an electric field. Recently a number of researchers have focused on electric field induced strain-mediated control of magnetic properties. While interesting, a robust modeling approach that accurately predicts the response of nanoscale structures magnetic response is unavailable.

The strain-mediated multiferroic approach consists of mechanically coupling magnetoelastic elements onto ferroelectric substrates [1], e.g. sputter deposition of composite heterostructures. In these composites, an electric field applied to the ferroelectric/piezoelectric substrate induces an anisotropic strain in the magnetoelastic material. The anisotropic stain induces a magnetic anisotropy via the converse magnetoelastic effect [2]. There exist fairly extensive studies containing both theoretical and experimental work on strain-mediated magnetization changes, coercivity changes [3], and strain-induced anisotropy in continuous magnetic thin films [4]. In all of the continuous film studies the strain is appropriately assumed to be uniform in the ferroelectric and ferromagnetic layers.

A relatively less studied area is the strain-mediated effect in multiferroic nanostructures [5]. For example, Bur et al. [7] reported strain-induced coercive field changes in patterned single-magnetic-domain nickel nanostructures deposited on Si/SiO_2 substrate. A few analytical studies also exist on uniform strain transfer and strain-induced change of magnetization in nanostructures [5,6,8]; however, as the thickness of the nanostructures increases or in-plane dimensions decrease, the validity of the uniform strain assumption becomes increasingly compromised. Recently, researchers have begun to investigate more sophisticated modeling techniques for coupling LLG with elastodynamics. These approaches include mathematical [9] and numerical [10,11] methods for the solutions of coupled micromagnetic and elastodynamic equations. While a few sophisticated solutions have been presented, these presentations do not compare their data directly with experimental results and thus leaves the modeling accuracy questionable.

In this study, we develop a numerical method based on finite elements to fully-couple micromagnetic simulations with elastodynamics in finite size 3D structures. The analytical results are compared to both conventional analytical methods and experimental results. The validated model is used to guide the development of experimental tests and devices using nanoscale magnetoelastic structures.

2 THEORY

The theoretical magnetoelastic framework for a problem between micromagnetics and elastodynamics reduces to seven coupled PDEs, which can be formulated in their weak form (i.e. referred to as LLG/EQ). Assumptions include small elastic deformations, linear elasticity, magnetostatics, and negligible electrical current contributions. The elastodynamic governing equations are

$$\rho \frac{\partial^2 \underline{u}}{\partial t^2} - \nabla \cdot \underline{\underline{\sigma}} = \underline{0} \tag{1}$$

where ρ is the density, σ is the stress tensor. The phenomenological Landau-Lifshitz-Gilbert (LLG) micromagnetic relations represent the second set of equations defined by

$$\frac{\partial \underline{m}}{\partial t} = -\mu_0 \gamma \left(\underline{m} \times \underline{H}_{eff} \right) + \alpha \left(\underline{m} \times \frac{\partial \underline{m}}{\partial t} \right) \tag{2}$$

Where γ is the Gilbert gyromagnetic ratio and α is the Gilbert damping constant. Substituting the appropriate constitutive relations and definitions including magnetocrystalline anisotropy field H_{anis}, exchange field H_{ex}, demagnetization field H_d, and magnetoelastic field H_{me} reduces the set of equations to six partial differential equations relating the displacements $\underline{u}$ and the magnetization $\underline{m}$ defined as:

$$\rho \frac{\partial^2 \underline{u}}{\partial t^2} - \nabla \cdot \underline{\underline{C}} \left[\frac{1}{2} \left(\nabla \underline{u} + (\nabla \underline{u})^T \right) \right] + \nabla \cdot \underline{\underline{C}} \left(\underline{\underline{\lambda}}^m \underline{m} \underline{m}^T \right) = \underline{0} \tag{3}$$

$$\frac{\partial \underline{m}}{\partial t} = -\mu_0 \gamma \left(\underline{m} \times \left(\underline{H}_{ext} + \underline{H}_{ex}(\underline{m}) + \underline{H}_d(\phi) + \underline{H}_{anis}(\underline{m}) + \underline{H}_{me}(\underline{m}, \underline{u}) \right) \right) + \alpha \left(\underline{m} \times \frac{\partial \underline{m}}{\partial t} \right) \tag{4}$$

Equations (3) and (4) along with the Ampere's law $\underline{H}_d = -\nabla\varphi$ represent seven equations as a function of seven unknowns defined by $\underline{u}$, ϕ, and $\underline{m}$. To solve this system LLG/EQ of coupled equations, the PDEs are formulated in their weak forms and solved numerically using finite elements.

3 SIMULATION & RESULTS

Experimental tests have been conducted on 100 nm × 300 nm × 35 nm nickel single domain nanostructures subjected to mechanical loads. An illustration of the finite element model used to analyze the experimental data is shown in Fig.1 (a). The structure is discretized using tetrahedral elements with a size on the order of nickel's exchange length (~8.5 nm). The nickel properties were derived from bulk values [12] and the Gilbert damping constant was chosen to be $\alpha = 0.5$ to improve stability and process time.

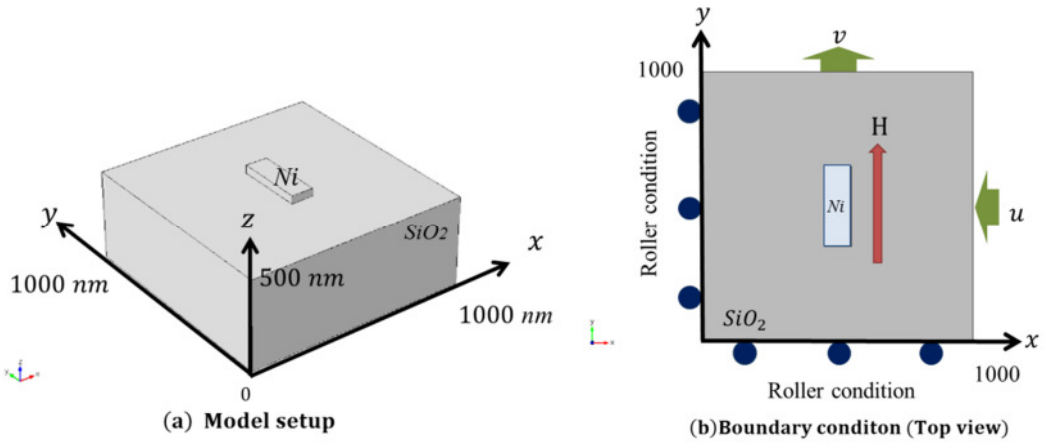

Figure.1 Schematic diagram of the model and boundary conditions

Figure 2(a) compares the coercive fields H_c as a function of effective applied strain (ε_{yy}-ε_{xx}) for the Stoner Wahlforth SW model, the micromagnetic LLG model assuming constant strain, the LLG/EQ model (described in this paper), and experimental data. The SW model shows significant disagreement with the experimental data by as much as 2350 Oe, while the LLG model and LLG/EQ model results have relatively better agreement but differ by as much as 200 Oe. Such inconsistencies in the analytical results are attributed to thermal issues, surface roughness, aspect ratio, or geometric smoothing in the nanostructure, which are not adequately represented in the numerical simulations. In Figure 2(b), the change in coercive field values (i.e., $\Delta H_c = H_c - H_c^0$) for the different curves are provided. The LLG/EQ model shows very good agreement with experiment data (less than 2% deviation) while the SW model and the LLG-constant strain model show relatively poor agreement with errors as large as 60%. These set of comparisons clearly indicate that non-uniform strain distributions must be considered when predicting the strain-mediated magnetic anisotropic effect in nanostructures. This is especially true when consider substantially stronger magnetoelastic materials such as Terfenol-D.

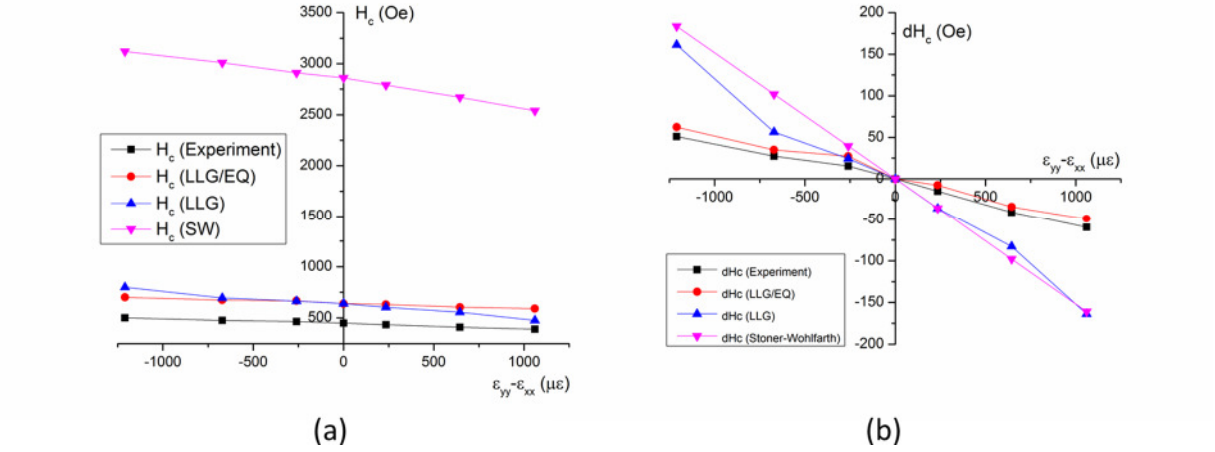

Figure.2 Comparison of models for (a) coercive field H_c and (b) coercive difference ΔH_c, as a function of (ε_{yy}-ε_{xx}).

Figure 3 shows analytical LLG/EQ results of the relative strain distribution in the Ni nanostructure with an effective applied strain ε_{yy}-ε_{xx}= -671$\mu\varepsilon$ and zero applied magnetic field. Figure 3(a) shows the surface plot for strains (ε_{yy}-ε_{xx}= -671$\mu\varepsilon$) in the nickel nanostructure. The simulation results clearly show that the strain distribution is non-uniform throughout the nanostructure. The relative strain values vary substantially between -700$\mu\varepsilon$ and -80$\mu\varepsilon$. Figure 3(b) plots the relative strain (ε_{yy}-ε_{xx}) as a function of y at x = 50nm for four different z values. Large strain variations are observed near the nanostructure ends (y = 0 nm and y = 300 nm), while the strain in the middle (y = 150 nm) is relatively uniform. The volume-averaged strain (ε_{yy}-ε_{xx}) for the nickel nanostructure is -322$\mu\varepsilon$ and is 50% less than the applied strain. The strain variation as a function of position occurs due to a well-known phenomenon, classically referred to as shear lag in the mechanics community. Therefore, one can clearly see that the assumption of constant strain present in SW and LLG is inappropriate for this structure.

4 CONCLUSION

In conclusion, we have developed a numerical approach based on a weighted residual formulation and finite elements for simulating magnetization states, magnetic hysteresis curves, and strain-induced coercive field changes in magnetic nanostructures by coupling the spatially-dependent strain state with micromagnetic simulation (LLG/EQ model) with elastodynamics. This model provides substantially better predictive results than the LLG model and the conventional Stoner-Wohlfarth (SW) model and in some cases must be used to accurately predict the response of a nanoscale structure. The LLG/EQ coupled model was verified with existing experimental data validating its predictive capabilities. In general this work strongly encourages researchers to use coupled solutions when modeling the

magnetoelastic response of finite size structures to accurately predict the magnetic response. This is important in a wide range of fields including memory, motors, and spin wave propagation.

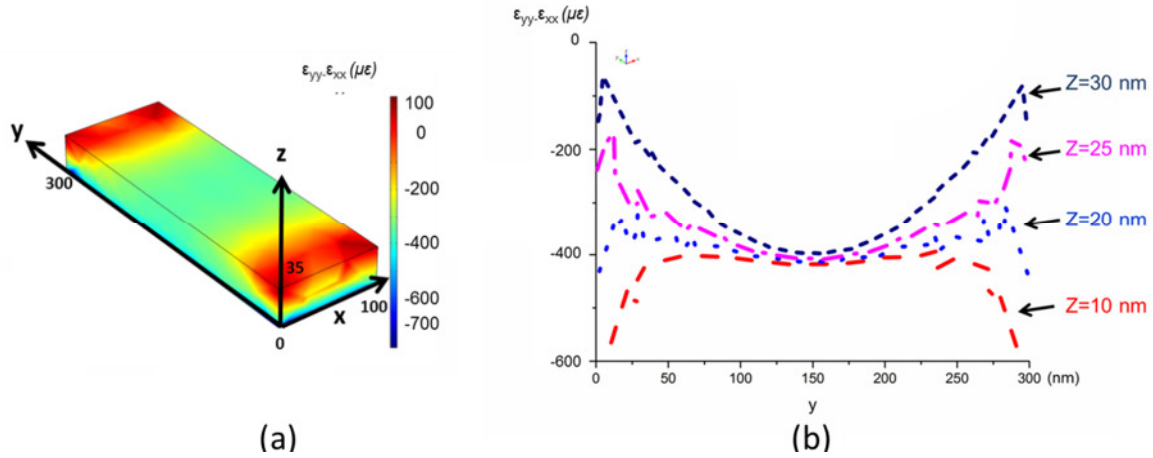

Figure.3. The strain distributions with (ε_{yy}-ε_{xx}= -671με) (a) contour plot and (b) as a function of y direction.

5 ACKNOWLEDGMENTS

This work was supported by the NSF Nanosystems Engineering Research Center for Translational Applications of Nanoscale Multiferroic Systems (TANMS), under Cooperative Agreement Award EEC-1160504.

REFERENCES

[1] J. Ma, J. M. Hu, Z. Li, and C. W. Nan, "Recent Progress in Multiferroic Magnetoelectric Composites: from Bulk to Thin Films," *Advanced Materials*, vol. 23, pp. 1062-1087, Mar 4 2011.

[2] B. Zhu, C. C. H. Lo, S. J. Lee, and D. C. Jiles, "Micromagnetic modeling of the effects of stress on magnetic properties," *Journal of Applied Physics*, vol. 89, pp. 7009-7011, Jun 1 2001.

[3] R. L. Hu, A. K. Soh, G. P. Zheng, and Y. Ni, "Micromagnetic modeling studies on the effects of stress on magnetization reversal and dynamic hysteresis," *Journal of Magnetism and Magnetic Materials*, vol. 301, pp. 458-468, Jun 2006.

[4] Y. J. Chen, T. Fitchorov, C. Vittoria, and V. G. Harris, "Electrically controlled magnetization switching in a multiferroic heterostructure," *Applied Physics Letters*, vol. 97, Aug 2 2010.

[5] J. M. Hu, G. Sheng, J. X. Zhang, C. W. Nan, and L. Q. Chen, "Phase-field simulation of electric-field-induced in-plane magnetic domain switching in magnetic/ferroelectric layered heterostructures," *Journal of Applied Physics*, vol. 109, Jun 15 2011.

[6] K. Roy, S. Bandyopadhyay, and J. Atulasimha, "Switching dynamics of a magnetostrictive single-domain nanomagnet subjected to stress," *Physical Review B*, vol. 83, Jun 22 2011.

[7] A. Bur, T. Wu, J. Hockel, C. J. Hsu, H. K. D. Kim, T. K. Chung, K. Wong, K. L. Wang, and G. P. Carman, "Strain-induced magnetization change in patterned ferromagnetic nickel nanostructures," *Journal of Applied Physics*, vol. 109, Jun 15 2011.

[8] J. Atulasimha and S. Bandyopadhyay, "Bennett clocking of nanomagnetic logic using multiferroic single-domain nanomagnets," *Applied Physics Letters*, vol. 97, Oct 25 2010.

[9] L. Banas, "Numerical methods for the Landau-Lifshitz-Gilbert equation," *Numerical Analysis and Its Applications*, vol. 3401, pp. 158-165, 2005.

[10] Y. C. Shu, M. P. Lin, and K. C. Wu, "Micromagnetic modeling of magnetostrictive materials under intrinsic stress," *Mechanics of Materials*, vol. 36, pp. 975-997, Oct 2004.

[11] J. X. Zhang and L. Q. Chen, "Phase-field microelasticity theory and micromagnetic simulations of domain structures in giant magnetostrictive materials," *Acta Materialia*, vol. 53, pp. 2845-2855, May 2005.

[12] Robert C. O'Handley, *Modern Magnetic Material: Principles and Applications* (John Wiley & Sons, Inc, 2000).

DIELECTRIC ELASTOMERS - NUMERICAL MODELING OF NONLINEAR ELECTROELASTICITY

Sven Klinkel

Lehrstuhl für Baustatik und Baudynamik, RWTH Aachen University
Mies-van-der-Rohe-Str. 1, Aachen, Germany
e-mail: klinkel@lbb.rwth-aachen.de

Abstract. *The paper is concerned with a numerical formulation to simulate the behavior of thin dielectric elastomer structures. Dielectric elastomers belong to the group of electroactive polymers. Due to the efficient electro-mechanical coupling and the huge actuation strain they are very interesting for actuator applications. The coupling effect in the material is mainly caused by the polarization. In the present work a simple constitutive relation, which is based on an elastic model involving one additional material constant to describe the polarization state, is incorporated in a solid shell formulation. It is based on a mixed variational principle of Hu-Washizu type. Thus, for quasi stationary fields, the balance of linear momentum and Gauss' law are fulfilled in a weak sense. As independent fields the displacements, electric potential, strains, electric field, mechanical stresses, and dielectric displacements are employed. The surface oriented shell element models the bottom and the top surfaces of a thin structure. This allows for a simple modeling of layered structures by stacking the elements through the thickness. An example is presented to demonstrate the ability of the proposed formulation.* ***March 2014***

1 Introduction

In the last decade electro-active polymers are increasingly applied to sensors and actuators. This paper is restricted to model the behavior of dielectric elastomers in which actuation is caused by electrostatic forces. The forces generate a compression between the electrodes and due to incompressibility a large elongation in lateral direction occurs. This effect is very prominent if one considers thin structures, which is shown in some experiments by [1], [2]. Typical dielectric elastomer devices consist out of thin membranes, see the above cited literature. This motivates us to deal with a shell formulation incorporating electro-mechanical coupling to model thin dielectric elastomer structures.

The electromechanical coupling occurs due to the contribution of the electromechanical body forces in the balance of linear and angular momentum, see e.g. [3]. For the electrically induced body force density and the couple density the polarization of the material plays an important role. The polarization describes the density of the electric dipole moments in a dielectric material. It appears only inside a material and may be derived from a constitutive relation. For electro sensitive elastomers a principle how to derive a constitutive model in the frame work of electro elasticity is proposed by [4, 5]. Within this framework Vu et al. [6, 7] suggested an invariant formulation with additional material constants. To observe an adequate material model these constants are needed to be determined by more or less complicated experiments. On the other hand the relative permittivity, which could be expressed with the susceptibility, is a

well known quantity. This motivates us to introduce a constitutive equation for the polarization where only one material constant is involved, which is the susceptibility, see also [8, 9]. Models which consider the viscous effect of the considered polymers are presented in [10, 11, 12, 13]

With restriction to elasticity the constitutive equations for the polarization and the mechanical stress are considered in the electrostatic balance laws. These are fulfilled within a mixed variational formulation. Here we make use of a Hu-Washizu type variational functional. In the frame of the finite element method the advantage of a mixed formulation is the robustness with respect to large load steps, cf. e.g. [14]. The surface oriented solid-shell element formulation allows to model layered structures by simply stacking up the elements.

2 Governing equations

Let the deformation $\Phi(\vec{\boldsymbol{X}}, t)$ be a point map from the reference configuration $\mathcal{B}$ with $\vec{\boldsymbol{X}} \in \mathcal{B}$ to the actual configuration $\mathcal{B}_t$ with $\vec{\boldsymbol{x}} \in \mathcal{B}$ at the time t. If $\vec{\boldsymbol{X}}$ and $\vec{\boldsymbol{x}} = \vec{\boldsymbol{u}} + \vec{\boldsymbol{X}}$ are the coordinates of $\mathcal{B}$ and the current configuration $\mathcal{B}_t$, the deformation gradient is given by $\boldsymbol{F} = \nabla_X \otimes \vec{\boldsymbol{x}}$. The Green-Lagrange strains are denoted by $\boldsymbol{E}$, whereas the electric field is denoted by $\vec{\boldsymbol{E}}$ and the electric potential as φ. With the 2nd Piola-Kirchhoff stress tensor $\boldsymbol{S}$, the electric stress tensor $\boldsymbol{T}$, the dielectric displacements $\vec{\boldsymbol{D}}$, the gravity load $\vec{\boldsymbol{g}}$ and the charge density ϱ the governing equations read

$$
\begin{aligned}
\boldsymbol{E} &= \frac{1}{2}(\boldsymbol{F}^T\boldsymbol{F} - \boldsymbol{1}) \quad \text{in } \mathcal{B}, & \nabla_X \cdot [\boldsymbol{F}(\boldsymbol{S} + \boldsymbol{T})] + \vec{\boldsymbol{g}} = 0 \quad & \text{in } \mathcal{B} \\
\vec{\boldsymbol{E}} &= -\nabla_X \varphi \quad \text{in } \mathcal{B}, & \nabla_X \cdot \vec{\boldsymbol{D}} + \varrho = 0 \quad & \text{in } \mathcal{B} \\
\vec{\boldsymbol{u}} &= \bar{\vec{\boldsymbol{u}}} \quad \text{on } \partial_u\mathcal{B}, & \boldsymbol{F}\boldsymbol{S} \cdot \vec{\boldsymbol{N}} = \bar{\vec{\boldsymbol{T}}} \quad & \text{on } \partial_S\mathcal{B} \\
\varphi &= \bar{\varphi} \quad \text{on } \partial_\varphi\mathcal{B}, & \vec{\boldsymbol{D}} \cdot \vec{\boldsymbol{N}} = -\bar{\zeta} \quad & \text{on } \partial_D\mathcal{B}.
\end{aligned}
$$

Here, $\vec{\boldsymbol{N}}$ denotes the unit normal outward vector on the boundary of the reference configuration and $\bar{\vec{\boldsymbol{T}}}$ is the traction, $\bar{\zeta}$ is an external charge. The constitutive equations

$$
\boldsymbol{S} + \boldsymbol{T} = \frac{\partial \Psi}{\partial \boldsymbol{E}}, \qquad \vec{\boldsymbol{D}} = -\frac{\partial \Psi}{\partial \vec{\boldsymbol{E}}}
$$

are determined by the energy function $\Psi = \psi - \frac{1}{2}\chi\epsilon_0(\vec{\boldsymbol{E}} \otimes \vec{\boldsymbol{E}}) : \boldsymbol{C}^{-1} - \frac{1}{2}J\epsilon_0(\vec{\boldsymbol{E}} \otimes \vec{\boldsymbol{E}}) : \boldsymbol{C}^{-1}$, here χ is the susceptibility and ϵ_0 the permittivity in vacuum. ψ refers to the elastic stored energy; in this work an Ogden-type of material is applied.

3 Variational formulation

A Hu-Washizu type variational functional is applied. As unknowns we assume displacements $\boldsymbol{u}$, electric potential φ, generalized stresses $\hat{\boldsymbol{S}}$, dielectric displacements $\hat{\vec{\boldsymbol{D}}}$, strains $\hat{\boldsymbol{E}}$ and the electric field $\hat{\vec{\boldsymbol{E}}}$. The variational formulation reads

$$
\begin{aligned}
\delta\pi = \int_{\mathcal{B}} \delta_u\boldsymbol{E} : \hat{\boldsymbol{S}} - \delta_\varphi\vec{\boldsymbol{E}} \cdot \hat{\vec{\boldsymbol{D}}} - \delta\boldsymbol{u} \cdot \vec{\boldsymbol{g}} - \delta\varphi\varrho \,\mathrm{d}V + \int_{\mathcal{B}} \delta\hat{\boldsymbol{E}} : (\frac{\partial\Psi}{\partial\boldsymbol{E}} - \hat{\boldsymbol{S}}) + \delta\hat{\vec{\boldsymbol{E}}} \cdot (\frac{\partial\Psi}{\partial\vec{\boldsymbol{E}}} + \hat{\vec{\boldsymbol{D}}}) \,\mathrm{d}V \\
+ \int_{\mathcal{B}} \delta\hat{\boldsymbol{S}} : (\hat{\boldsymbol{E}} - \boldsymbol{E}) - \delta\hat{\vec{\boldsymbol{D}}} \cdot (\hat{\vec{\boldsymbol{E}}} - \vec{\boldsymbol{E}}) \,\mathrm{d}V = 0,
\end{aligned}
$$

where δ_u, δ_φ are the variations with respect to the displacements and electric potential respectively. For the finite element approximation see [8].

4 Numerical example

A two way bending actuator is investigated. The device consists out of two bonded layers. An electric field through the thickness is applied only to one of these layers. The eccentric elongation leads to a bending response of the composite. For the elastic behavior an Ogden type of material is employed, the material parameters are given in Tab. 1, where $\varepsilon_r = (1+\chi)\varepsilon_0$ denotes the relative permittivity.

ε_r	ε_0	4.7	8.854 e−12	F/m
α_1	μ_1	0.7	5.488 e−02	MPa
α_2	μ_2	3.25	9.1 e−04	MPa
α_3	μ_3	−3.7	−6.3 e−06	MPa

Table 1: Material parameters, see [15]

The device with the displacement boundary conditions and the geometrical data is given in Fig. 1. It is modeled with 18x32 elements in plane and each layer with one element through the thickness. The voltage is applied either on top of the upper layer or on bottom of the lower layer. The interface between the layer is grounded. When the loading is applied on the upper layer, the area of this layer expands and the whole structure bends down, because of the eccentricity. Utilizing this effect it is possible to reach $360°$ bending down or up response. In Fig. 1 several deformed configurations are displayed. For this calculation the voltage is raised from 0 kV up to 4.2 kV in 42 steps with a step range of 100 V.

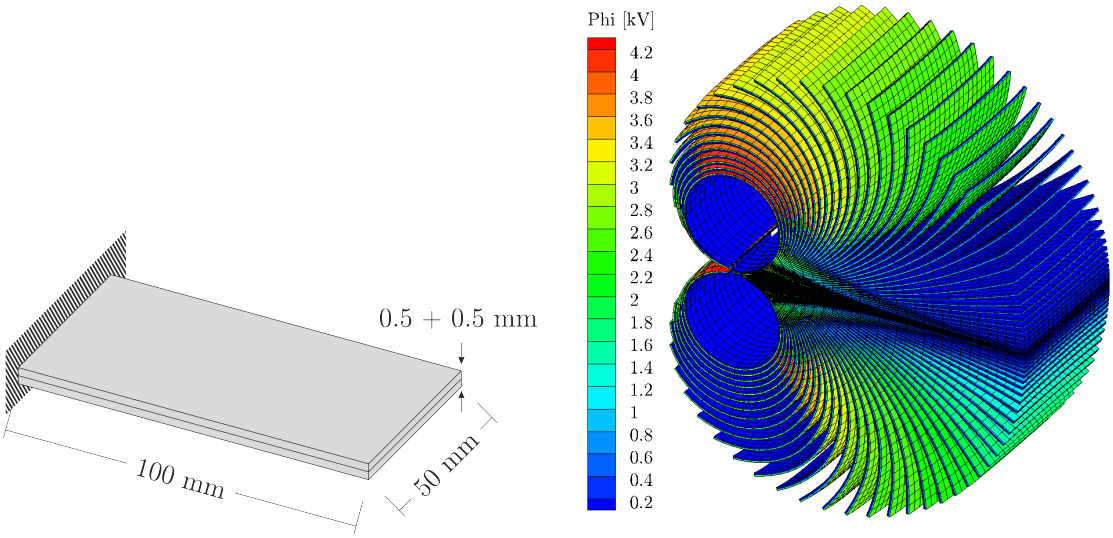

Figure 1: Left: initial geometry of the bending actuator. Right: deformed configurations with a color plot of the applied voltage

REFERENCES

[1] M. Wissler and E. Mazza. Modeling and simulation of dielectric elastomer actuators. *Smart Materials & Structures*, 14(6):1396–1402, 2005.

[2] M. Hossain, D. K. Vu, and P. Steinmann. Experimental study and numerical modelling of VHB 4910 polymer. *Computational Materials Science*, 59:65–74, 2012.

[3] R.M. McMeeking and C.M. Landis. Electrostatic forces and stored energy for deformable dielectric materials. *Journal of Applied Mechancis-Transactions of the ASME*, 72(4):581–590, 2005.

[4] A. Dorfmann and R.W. Ogden. Nonlinear electroelasticity. *Acta Mechanica*, 174:167–183, 2005.

[5] R. Bustamante, A. Dorfmann, and R. W. Ogden. Nonlinear electroelastostatics: a variational framework. *Zeitschrift für Angewandte Mathematik und Physik*, 60(1):154–177, 2009.

[6] D. K. Vu, P. Steinmann, and G. Possart. Numerical modelling of non-linear electroelasticity. *International Journal for Numerical Methods in Engineering*, 70(6):685–704, 2007.

[7] D. K. Vu and P. Steinmann. A 2-d coupled bem-fem simulation of electro-elastostatics at large strain. *Computer Methods in Applied Mechanics and Engineering*, 199(17-20):1124–1133, 2010.

[8] S. Klinkel, S. Zwecker, and R. Mueller. A solid shell finite element formulation for dielectric elastomers. *Journal of Applied Mechanics-Transactions of the ASME*, 80(2), 2013.

[9] R. Müller, B.X. Xu, D. Gross, M. Lyschik, D. Schrade, and S. Klinkel. Deformable dielectrics - optimization of heterogeneities. *Int. J. Engng Science*, 48:647–657, 2010.

[10] C. Miehe, D. Rosato, and B. Kiefer. Variational principles in dissipative electro-magneto-mechanics: A framework for the macro-modeling of functional materials. *International Journal for Numerical Methodes in Engineering*, 86(10):1225–1276, 2011.

[11] A. Ask, A. Menzel, and M. Ristinmaa. Phenomenological modeling of viscous electrostrictive polymers. *International Journal of Non-Linear Mechanics*, 47:156–165, 2012.

[12] A. Bueschel, S. Klinkel, and W. Wagner. A viscoelastic model for dielectric elastomers based on a continuum mechanical formulation and its finite element implementation. In BarCohen, Y and Carpi, F, editor, *Electroactive Polymer Actuators and Devices (EAPAD) 2011*, volume 7976 of *Proceedings of SPIE*. SPIE; Amer Soc Mech Engineers, 2011. Conference on Electroactive Polymer Actuators and Devices (EAPAD) 2011, San Diego, CA, MAR 07-10, 2011.

[13] A. Bueschel, S. Klinkel, and W. Wagner. Dielectric elastomers - numerical modeling of nonlinear visco-electroelasticity. *International Journal for Numerical Methodes in Engineering*, 93(8):834–856, 2013.

[14] S. Klinkel, F. Gruttmann, and W. Wagner. A robust non-linear solid shell element based on a mixed variational formulation. *Computer Methods in Applied Mechanics and Engineering*, 195(1-3):179–201, 2006.

[15] Z. Gao, A. Tuncer, and A.M. Cuitiño. Modeling and simulation of the coupled mechanical-electrical response of soft solids. *International Journal of Plasticity*, 27(10):1459 – 1470, 2011.

EXISTENCE AND UNIQUENESS RESULT FOR FERROELECTRIC MODELS IN CYLINDRICAL DOMAINS

Nataliya Kraynyukova

Working Group Partial Differential Equations and Applications, Department of Mathematics,
Darmstadt University of Technology,
Schlossgartenstr. 7, Darmstadt, Germany,
e-mail: kraynyukova@mathematik.tu-darmstadt.de

Abstract. *Macroscopic models for nonlinear behavior of ferroelectrics presented in [1,4,6,8] use remanent strain and remanent polarization as internal variables. In general form these models are difficult to handle within the mathematical existence theory. We consider a simple geometric case, when the material body has a constant cross section perpendicular to the x_3-axis. Electromechanical forces applied to the whole top and bottom surfaces of the material body are supposed to be constant in a spatial variable x and depend only on time t. In this case the problem can be reduced to the system of ordinary differential equations, which has a local in time, unique solution. We discuss the dynamics of internal variables.*

1 Introduction and setting of the problem

We consider models for nonlinear hysteresis behavior of ferroelectrics presented in [1,4,6,8]. In general form these models contain two nonlinear relations, which raise difficulties for the mathematical existence theory. The first nonlinearity is the piezoelectric tensor, which depends on the remanent polarization. The equations of piezoelectricity for the fixed values of internal variables can be regarded as an elliptic system of partial differential equations. The assumptions on the coefficients required by the common existence theory for elliptic systems can not be automatically deduced for the piezoelectric tensor in a general ferroelectric model. The second difficulty is a composition of two nonlinear functions in the evolution differential equations for the internal variables: the flow rule function and the function which constrains the internal variables by its saturation values. Differential equations with such kind of nonlinearity are often referred to as doubly-nonlinear equations and to the authors knowledge there is no existence results, which can be applied directly to the unmodified ferroelectric equations. We discuss briefly mathematical existence results [2,3,7] proved for modifications of general ferroelectric models. In the presented work the following special case of ferroelectric models is considered. We suppose that the cross section of the material body perpendicular to the x_3-axis is constant for all x_3. The electromechanical forces are assumed to be applied to the whole plane top and bottom surfaces. In this case we prove that the solution exists locally in time and is unique.

Let $\overline{\Omega} \subset \mathbb{R}^2$ be an open bounded set with the origin inside the external boundary of $\overline{\Omega}$. Let the material body occupy the set $\Omega \in \mathbb{R}^3$ defined by $\Omega = \overline{\Omega} \times \gamma x_3$ with $\gamma \in [0, H]$. Unknown are the following functions which in general depend on the material point $x \in \Omega$ at time $t \in [0, T]$: the displacement field u, the Cauchy stress tensor σ, the remanent strain tensor r, the electric potential ϕ, the vector of electric displacements D and the vector of remanent polarization P.

The functions

$$\varepsilon = \frac{1}{2}(\nabla_x u + (\nabla_x u)^T) \quad \text{and} \quad E = -\nabla_x \phi$$

denote the linearized strain tensor and the electric field vector, respectively. The fundamental assumption of the models under consideration is that the strain tensor ε and the vector of electric displacements D can be additively decomposed into reversible and irreversible parts

$$\varepsilon = (\varepsilon - r) + r, \quad D = (D - P) + P.$$

Here $\varepsilon - r$ and $D - P$ are reversible (for fixed values of the functions r and P) and r and P are irreversible parts of ε and D, respectively.

The unknown functions satisfy the following system of equations

$$-\operatorname{div} \sigma = b, \quad \operatorname{div} D = q, \tag{1}$$

$$\varepsilon - r = \mathbf{S}\sigma + \mathbf{d}E, \quad D - P = \mathbf{d}^{\mathbf{T}}\sigma + \mathbf{k}E, \tag{2}$$

$$P_t \in g_1(E - \partial_P f + (\partial_P \mathbf{d})E \cdot \sigma), \quad r_t \in g_2(\sigma - \partial_r f + (\partial_r \mathbf{d})E \cdot \sigma) \tag{3}$$

completed by the boundary conditions

$$\sigma \cdot n = 0,\ D \cdot n = 0,\ (x_1, x_2) \in \partial\overline{\Omega},\ x_3 \in [0, H], \tag{4}$$

$$\phi(t, x_1, x_2, 0) = 0, \quad u_1(t, 0, x_2, x_3) = u_2(t, x_1, 0, x_3) = u_3(t, x_1, x_2, 0) = 0, \tag{5}$$

$$\sigma_{33}(t, x_1, x_2, H) = \overline{\sigma}(t), \quad \phi(t, x_1, x_2, H) = \overline{\phi}(t), \tag{6}$$

and the initial conditions

$$r(0) = r^0, \quad P(0) = P^0. \tag{7}$$

The equations (1) are the equilibrium equation and the Gauss equation in a quasi-static case, respectively. Here $b \in \mathbb{R}^3$ and $q \in \mathbb{R}$ are supposed to be constant. $\mathbf{S}$ is the fourth-order tensor of elastic compliance measured in the absence of electric field, $\mathbf{k}$ is the second-order dielectric permittivity tensor measured the absence of mechanical forces. Both tensors $\mathbf{S}$ and $\mathbf{k}$ are supposed to be isotropic and independent of internal variables [4]. The mapping $\mathbf{d}$ is the third-order piezoelectric tensor. In [1,4,6,8] the tensor $\mathbf{d}$ is supposed to depend on the remanent polarization P and to be transversally isotropic with the symmetry axis, which coincides with the polarization direction $p = \frac{P}{|P|}$. For example, in [1,4,6] $\mathbf{d}$ has the form

$$\mathbf{d}_{kij} = \frac{|P|}{P_s}\Big(\mathrm{d}_{33} p_k p_i p_j + \mathrm{d}_{31} p_k \alpha_{ij} + \frac{1}{2}\mathrm{d}_{15}(p_i \alpha_{jk} + p_j \alpha_{ik})\Big), \tag{8}$$

where $\alpha_{ij} = \delta_{ij} - p_i p_j$, P_s is the saturation value of $|P|$ and d_{ij} are piezoelectric constants measured when $|P| = P_s$. The experimental results in [5,9] show that the reversible response of the material strongly depends on the state of internal variables, therefore the assumption that $\mathbf{d}$ depends on internal variables seems to be unavoidable. We assume that the given functions $\overline{\sigma}$ and $\overline{\phi}$ depend on t and do not depend on x. The boundary of $\overline{\Omega}$ is supposed to be flat enough to avoid contacts of surface points under applied forces. The diagonal matrix r^0 with elements $r^0_{11} = r^0_{22}$, r^0_{33} and $P^0 = (0, 0, P^0_3)$ are assumed to be constant. The form of the functions g_1, g_2 and f in (3) is a constitutive assumption of the models. The nonlinear function $f = f(r, P)$ is the additive irreversible part of the energy, which constrains internal variables by their saturation values.

2 Local existence and uniqueness of solution for the model (1)-(7).

We construct an approximative sequence of functions (ϕ_n, u_n, r_n, P_n) by the iterative procedure. We show that the sequence (ϕ_n, u_n, r_n, P_n) converges to the local unique solution (ϕ, u, r, P) of the model (1)-(7) under continuity assumptions for the constitutive functions g_1, g_2, f. We discuss the result in relation to the models [1,4,6,8]. In conclusion, we analyze the dynamics of internal variables governed by the evolution equations (3), (7).

REFERENCES

[1] M. Kamlah. Ferroelectric and ferroelastic piezoceramics - modeling of electromechanical hysteresis phenomena, *Continuum Mech. Thermodyn.*, 13(4):219-268, 2001.

[2] N. Kraynyukova, H.-D. Alber. A doubly nonlinear problem associated with a mathematical model for piezoelectric material behavior. *Z. Angew. Math. Mech.*, 92(2):141-159, 2012.

[3] N. Kraynyukova, S. Nesenenko. Measure-valued solutions for ferroelectric materials, accept. in *P. Roy. Soc. Edinb. A*, 2013.

[4] C. M. Landis. Fully coupled, multi-axial, symmetric constitutive laws for polycrystalline ferroelectric ceramics, *J. Mech. Phys. Solids*, 50:127-152, 2002.

[5] Q. D. Liu, J. E. Huber. State dependent linear moduli in ferroelectrics, *Int. J. Solids Struct.*, 44:5635-5650, 2007.

[6] R.M. McMeeking, C.M. Landis. A phenomenological multi-axial constitutive law for switching in polycrystalline ferroelectric ceramics. *Int. J. Eng. Sci.*, 40:1553-1577, 2002.

[7] A. Mielke, A.M. Timofte. An energetic material model for time-dependent ferroelectric behavior: Existence and uniqueness, *Math. Meth. Appl. Sci.*, 29:1393-1410, 2006.

[8] H. Romanowski, J. Schröder. Coordinate invariant modelling of the ferroelectric hysteresis within a thermodynamically consistent framework. A mesoscopic approach, *Trends in Applications of Mathematics to Mechanics, Wang Y., Hutter K. (eds). Shaker Verlag: Aachen*, 419-428, 2005.

[9] D. Zhou, R. Wang, M. Kamlah. Determination of reversible and irreversible contributions to the polarization and strain response of soft PZT using the partial unloading method, *J. Eur. Ceram. Soc.*, 30:2603-2615, 2010.

CONFIGURATIONAL FORCES CONCEPT FOR SPATIAL CRACK CONFIGURATIONS IN FERROELECTRIC MATERIALS

Meinhard Kuna[1], **and Benjamin Nassauer**[2]

[1,2] Institute of Mechanics and Fluid Dynamics, Technische Universität Bergakademie Freiberg
Lampadiusstraße 4, 09599 Freiberg, Germany
[1] e-mail: Meinhard.Kuna@imfd.tu-freiberg.de, [2] e-mail: Benjamin.Nassauer@imfd.tu-freiberg.de

Abstract. *In this paper the application of the configurational forces concept to fracture mechanics analysis of ferroelectric ceramics is presented. To predict the non-linear ferroelectric material behavior due to polarization switching in ferroelectric polycrystals, a three-dimensional micromechanical material model for tetragonal domain types is applied. The underlying electromechanical boundary value problem is solved by means of the finite element method. The configurational forces are calculated in a post-processing for several three-dimensional crack configurations. The correlation between configurational forces and the electromechanical J-Integral vector is discussed. This concept might offer a suitable approach to assess fracture in ferroelectric structures.*

1 Introduction

Ferroelectric ceramics are brittle and susceptible to cracking at all scales. The limited reliability of ferroelectric devices due to fracture constitutes a major impediment to their large-scale usage. While linear piezoelectric fracture is now well investigated, the fracture behavior in ferroelectrics shows high complexity attributed to the inherent non-linear polarization processes. High concentration of stress and/or electric fields near the crack tip will cause domain switching, which is found to have a significant influence upon fracture. The change of domain structure strongly affects the internal electric field and/or stress state near the crack tip which may reduce or intensify the applied external electromechanical loading, resulting in strengthening or weakening of the effective fracture toughness. Therefore, capturing non-linear constitutive behavior of ferroelectric polycrystalline materials is inevitable to identify appropriate fracture parameters and criteria.

2 Micromechanical ferroelectric material model

There exist several approaches for the treatment of non-linear ferroelectric behavior such as non-linear phenomenological continuum models, phase field models and micromechanical models of domain switching. In the present work, the micromechanical approach is favoured because it represents the switching and evolution of domain variants with regard to the materials microstructure such as grains and anisotropy, typical for engineering ferroelectrica like PZT. Moreover, it allows to simulate specific failure mechanisms occurring in the crack vicinity and to capture any multi-axial electromechanical loading path.

The material model employed here is mainly based on works of Huber *et al* [1] and Pathak, McMeeking [2]. The idea of the model is to consider the ferroelectric polycrystal as an assembly of single crystals with specific lattice orientations. Each of the crystals consists of

several domains with different spontaneous polarization directions. Assuming tetragonal unit cells, six domain variants are possible in 3D space. The volume fractions of these domains can change if an electric field or mechanical stress is applied. This domain switching is determined by an energy-based criterion. Due to switching the average polarization vector, the remanent strain and the average mechanical, electrical and piezoelectrical material properties of the crystal change, resulting in non-linear macroscopic response. The material model has been implemented in the commercial finite element software ABAQUS by means of a three-dimensional user element and a user material routine. The non-linear system of equations is solved in the usual way by an incremental, iterative Newton's scheme. A more detailed description can be found in [3, 4]. The parameters of the micromechanical model were adjusted to PZT-5H. This concerns the elastic, piezoelectric and dielectric anisotropic constants, as well as the spontaneous polarization $P^{sp} = 0.3C/mm$, strain $\varepsilon^{sp} = 0.003$ and coercive field strength $E_c = 0.8kV/mm$. By means of finite element simulations of a representative volume element of a polycrystal, a qualitative good representation of measured polarization and butterfly hysteresis loops [5] was achieved as function of mechanical pre-load.

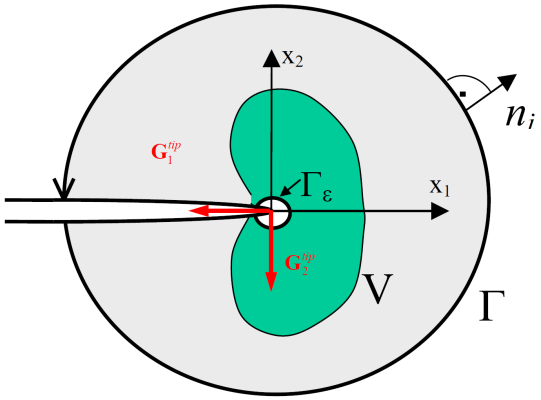

Figure 1: Switching zone around a crack tip and integration of J-integral

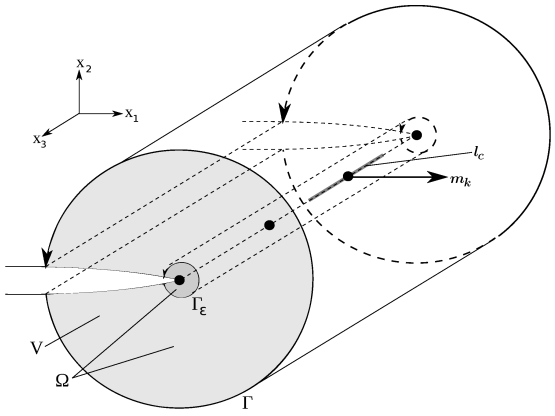

Figure 2: Calculation of configurational forces along 3D crack front

3 Configurational forces

The theory of configurational forces is based on ideas of Eshelby and represents a very useful tool for analysing the thermodynamic driving energy on cracks in a material. The configurational force g_k can be derived from the divergence of the configurational stress tensor Σ_{kj}:

$$g_k = -\Sigma_{kj,j}. \tag{1}$$

The latter is given as:

$$\Sigma_{kj} = h\delta_{kj} - \sigma_{ij}u_{i,k} - D_j\varphi_{,k} \tag{2}$$

with the stresses σ_{ij}, the displacement vector u_i, the dielectric displacement D_i, the electric potential φ, and the electric enthalpy h:

$$h = \frac{1}{2}\left(\varepsilon_{ij} - \varepsilon_{ij}^R\right) c_{ijkl} \left(\varepsilon_{kl} - \varepsilon_{kl}^R\right) - \left(\varepsilon_{ij} - \varepsilon_{ij}^R\right) e_{kij} E_k - \frac{1}{2} E_k \kappa_{kl} E_l - P_k^R E_k \tag{3}$$

considering the remanent strain ε_{ij}^R and polarization P_k^R. To calculate the configurational forces numerically within the finite element method, Eq. (1) is multiplied with a vectorial test function

η_i and integrated over the domain B [5]:

$$\int_B (\Sigma_{kj,j} + g_k)\, \eta_i dV = 0. \tag{4}$$

Discretising the test function with nodal values and shape functions N^I leads to the definition of the discrete configurational forces at the nodes I of a finite element:

$$G_i^{eI} = \int_{V^e} N^I g_i dV = \int_{V^e} \Sigma_{ij} N^I_{,j} dV \tag{5}$$

with the volume of the finite element V^e. The second integral in Eq.(5) can be easily calculated using Eqs.(2) and (4). The total discrete configurational force at a node I consists of the contributions of all adjacent elements:

$$G_i^I = \bigcup_{e=1}^{n^{el}} G_i^{eI}. \tag{6}$$

4 Application to fracture mechanics

It is well known that the configurational forces and the J-integral of fracture mechanics are related. If the classical electromechanical line integral J is computed along an arbitrary contour Γ around the crack tip in a ferroelectric material (see Fig. 1), it is found that J is not independent of the chosen path. This is obvious, since J includes not only the effect of the crack tip singularity but also the non-linear remanent strains and polarizations due to domain switching in the enclosed region. To separate both effects the integration contour is shrunk to the crack tip yielding the near tip J-integral $\tilde{J}_k$:

$$\tilde{J}_k = \lim_{\varepsilon \to 0} \int_{\Gamma_\varepsilon} \Sigma_{kj} n_j ds. \tag{7}$$

$$J_{tip} = \tilde{J}_k^I m_k = -\frac{G_k^{tipI}}{l_c^I} m_k \tag{8}$$

with the unit vector m_k lying in the crack plane and perpendicular to the crack front and l_c^I being the length of a crack front segment assigned to the crack front node I. By these considerations the dissipative processes in the switching domain are separated from the real crack driving force.

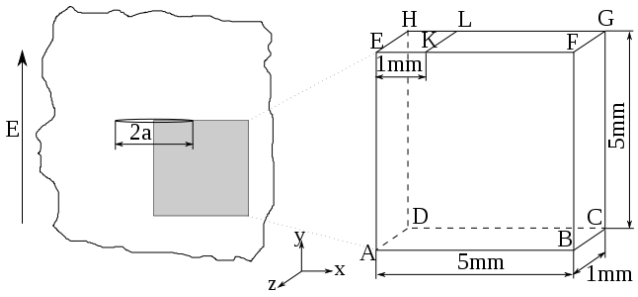

Figure 3: Plate with a part-through crack under cyclic electromechanical loading

5 Numerical Example of a 3D Crack

The configurational forces are used to calculate the J-integral of a part-through crack in a finite plate (see Fig. 3) under cyclic loading by a perpendicular electric field, altering from - $4E_c$ to $+4E_c$. The results at one node of the crack front are shown in Fig. 4 for various integration contour. Applying the electrical load, the J-integral becomes negative first. This effect is known from piezoelectric materials if the crack is electrically impermable as in this study. If the coercive field strength E_c is reached, domain switching occurs, which has a strong influence on the J-integral. After unloading the remanent strain and polarization remain in the body, leading to a positive value of J. This means the residual fields induce a positive crack driving force. The path-dependency of the classical J-integral becomes obvious. Only the crack tip value J_{tip} can serve as a real fracture parameter to be confronted with material toughness values. The behavior is qualitatively the same for all nodes along the crack front, see Fig. 5. However, the domain switching processes are different in due to the random distribution of lattice orientations in the model, influencing the crack driving force along the crack tip.

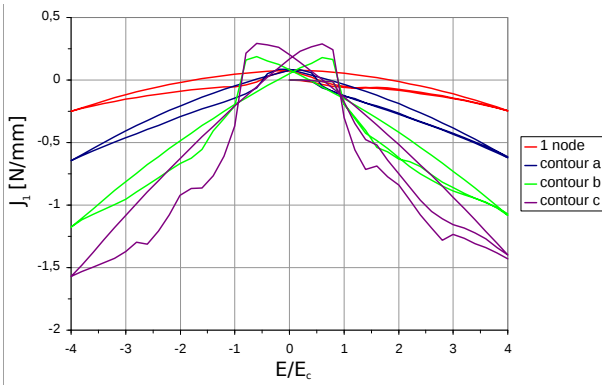

Figure 4: Path dependency of J-integral for 3D part-through crack under cyclic electrical loading

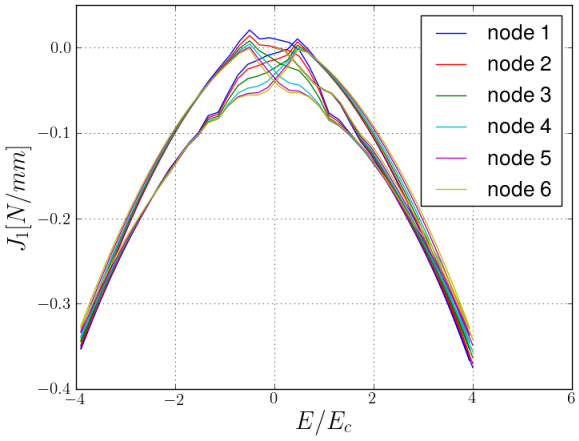

Figure 5: J-integral along crack front

References

[1] Huber, J.E., Fleck, N.A., Landis, C.M., McMeeking, R.M.: A constitutive model for ferroelectric polycrystals. *J Mech Phys Solids* **47**:1663-1697, 1999.

[2] Pathak, A., McMeeking, R.M.: Three-dimensional finite element simulations of ferroelectric polycrystals under electrical and mechanical loading. *J Mech Phys Solids* **56**:663-683, 2008.

[3] Qun Li, Ricoeur, A., Enderlein, M. and Kuna, M.: Evaluation of electromechanical coupling effect by microstructural modeling of domain switching in ferroelectrics. *Mechanics Research Communications*, **37**:332-336, 2010.

[4] Qun Li and Kuna, M.: Inhomogeneity and material configurational forces in three dimensional ferroelectric polycrystals. *European Journal of Mechanics - A/Solids*, **31**:77-89, 2012.

[5] Mueller, R., Kolling, S., Gross, D.: On configurational forces in the context of the finite element method. *Int J Num Meth Eng* **53**:1557-1574, 2002.

[6] Zhou, D.Y., Kamlah, M., Munz, D.: Effects of uniaxial prestress on the ferroelectric hysteretic response of soft PZT. *J European Ceramic Society* **25**:425432, 2005.

A CONDENSED APPROACH TO MODELING AND ANALYSIS OF TETRAGONAL AND RHOMBOHEDRAL FERROELECTRICS

Stephan Lange[1], **Andreas Ricoeur**[2] **and Rebecca Merkel**[3]

[1,2,3] Institute of Mechanics, Chair of Engineering Mechanics / Continuum Mechanics, University of Kassel
Moenchebergstr. 7, 34109 Kassel, Germany
e-mail: stephan.lange@uni-kassel.de

Abstract. *In the paper a condensed model for ferroelectric solids with tetragonal and rhombohedral unit cells is presented. The approach is microelectromechanically and physically motivated, considering discrete switching processes on the level of unit cells and quasi-continuous evolution of inelastic fields on the domain wall level. To calculate multiple grain interactions an averaging technique is applied. Hysteresis loops are simulated for pure electric and electromechanical loading, demonstrating e.g. the influence of a compressive preload on the poling and stress-strain behavior. Further, residual stresses are calculated as a result of switching processes and interactions between statistically arranged crystallits. These stresses and some hysteresis loops are compared to Finite Element calculations demonstrating the potential of the condensed approach.*

1 Introduction

Ferroelectric materials such as barium titanate (BT) or lead zirconate titanate (PZT) have been established as components of so-called smart structures during the past few decades. They are used as bulk material in actuators or sensors and are constitutents of micro electromechanical systems (MEMS) and composite devices. To model the nonlinear behavior of ferroelectric materials, a variety of models has been published during the past decades. HWANG et. al. [1] propose a model that assumes a polycrystal with monodomain grains, where the polarization switches by a discrete angle if an energetic switching criterion is satisfied. In HUBER et. al. [2], scalar weights are introduced for each orientation of the c-axis of a tetragonal unit cell within a grain. Within the context of material theory, they have to be interpreted as internal variables controlling all dissipative processes. Their evolution is governed by energetic considerations based on the first and second principles of thermodynamics. Most of the approaches that have been developed are implemented within the framework of the Finite Element Method (FEM), enabling the solution of complex boundary value problems. On the other hand, the implementation of a discretization scheme is going along with a high effort and the solution of problems requires high computational costs. However, many results shown in papers are restricted to very basic boundary value problems under uniaxial loading. The goal mostly is to calculate different hysteresis loops of tetragonal ferroelectrics, thus demonstrating and investigating their constitutive behavior. This kind of investigation, however, does not require the application of a discretization method. On the other hand, it is not appropriate just considering a single grain based method, since grain-grain interaction is crucial for most macroscopically observed features of a polycrystalline ferroelectric material.

In the presented approach, the interaction between grains is taken into account applying an averaging technique calculating effective inelastic mechanical and electrical fields for a polycrystalline material. The computational and implementation effort going along with the condensed model is low compared to FEM based approaches. Nevertheless, all essential features are included yielding smooth hysteresis loops of the bulk material under combined electromechanical load and residual stresses in each grain. Besides classically modelled tetragonal ferroelectrics, rhombohedral unit cells are in the focus of investigation.

2 Condensed approach for a nonlinear ferroelectric model

In the whole paper the analytical notation is applied implying summation over double indices. The system under consideration is a ferroelectric ceramic. Here, barium titanate is supposed for tetragonal unit cells and $\mathrm{PbTiZrO_3}$ for rhombohedral ones. Further, volume forces b_i and charges ω_V are neglected. Therefore, the balance equations of mechanical and electrostatic equilibrium are reduced to:

$$\sigma_{ij,j} = 0 \quad \text{and} \quad D_{i,i} \;\; = 0 \tag{1}$$

with stresses σ_{ij} and electric displacement D_i. To describe the nonlinear behavior of a ferroelectric material, the thermodynamic potential

$$\begin{aligned}\psi\left(\varepsilon_{kl}, E_l\right) = \frac{1}{2} C_{ijkl}\varepsilon_{kl}\varepsilon_{ij} - e_{lij}E_l\varepsilon_{ij} - \frac{1}{2}\kappa_{il}E_lE_i - C_{ijkl}\varepsilon^{irr}_{kl}\varepsilon_{ij} + \\ + e_{ikl}\varepsilon^{irr}_{kl}E_i - P^{irr}_i E_i\end{aligned} \tag{2}$$

leads to the following constitutive equations of a nonlinear ferroelectric material:

$$\sigma_{ij} = \left.\frac{\partial\psi}{\partial\varepsilon_{ij}}\right|_{E_i} = C_{ijkl}\left(\varepsilon_{kl} - \varepsilon^{irr}_{kl}\right) - e_{lij}\,E_l, \tag{3}$$

$$D_i = -\left.\frac{\partial\psi}{\partial E_i}\right|_{\varepsilon_{ij}} = e_{ikl}\left(\varepsilon_{kl} - \varepsilon^{irr}_{kl}\right) + \kappa_{il}\,E_l + P^{irr}_i, \tag{4}$$

where ε_{kl} and ε^{irr}_{kl} are the total and irreversible switching strains, respectively, E_l is the electric field and P^{irr}_i denotes the spontaneous polarization. The domain structure of tetragonal ferroelectrics exhibits $90°$ and $180°$ and of rhombohedral ferroelectrics $70.5°$, $109.5°$ and $180°$ domain walls, respectively. In the presented model, the domain structure of a grain is condensed to a single material point with internal variables $\nu^{(n)}$ representing the four possible orientations (s. Figure 1 and Figure 2). The orientations of the domains with respect to the global coordinate

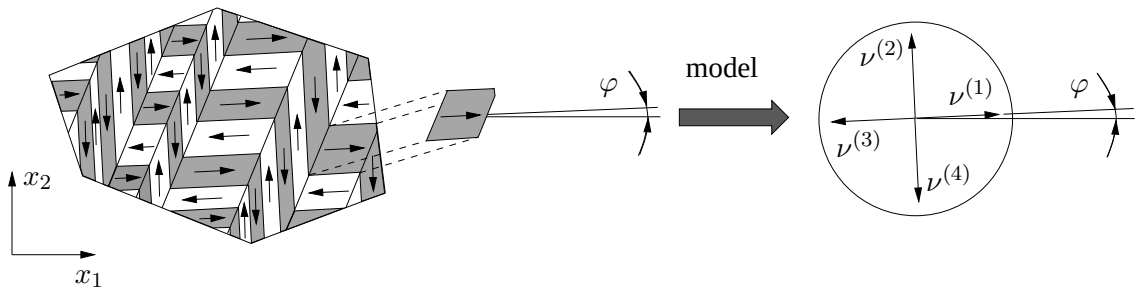

Figure 1: Domain structure of a tetragonal single grain and motivation of the internal variables $\nu^{(n)}$.

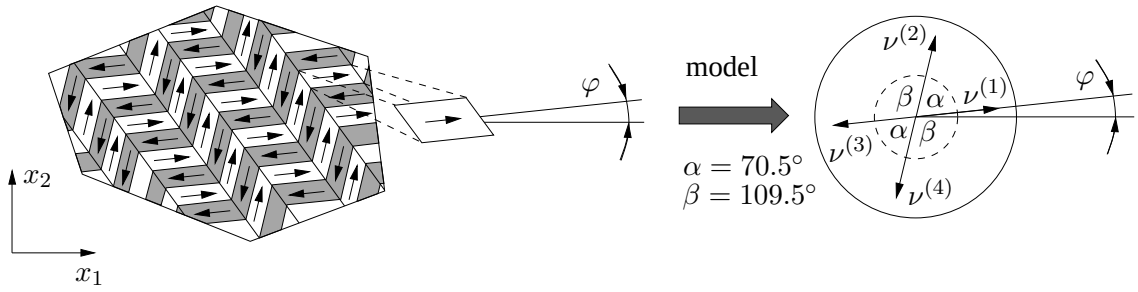

Figure 2: Domain structure of a rhombohedral single grain.

system are described by an angle φ. The calculations start with an unpoled material, thus the internal variables are $\nu^{(n)} = \nu_0 = 0.25$. All material properties and the change of irreversible quantities on the macroscopic scale can be expressed in terms of the $\nu^{(n)}$. The evolution law of volume fractions is based on the CLAUSIUS-DUHEM inequality [3] reading:

$$\mathrm{d}\nu_{(k)}^{(n)} = -\mathrm{d}\nu_0 \, H \left(\frac{w_{(k)}^{diss(n)}}{w_{(k)}^{crit}} - 1 \right) \quad \text{and} \quad w_{(k)}^{diss(n)} = \sigma_{ij} \varepsilon_{ij(k)}^{sp(n)} + E_i \Delta P_{i(k)}^{sp(n)}. \tag{5}$$

In Eq. (5) $\mathrm{d}\nu_0$ describes a numerical parameter and the Heaviside function H is equal to zero in case of $w_{(k)}^{diss(n)} < w_{(k)}^{crit}$ or equal to one if $w_{(k)}^{diss(n)} \geq w_{(k)}^{crit}$. The indices n and k represent the possible orientation and switching directions. Critical values of a tetragonal unit cell are e.g. given by [4]. For a rhombohedral unit cell the calculation of the critical values, spontaneous polarization and spontaneous strain are determined likewise accounting for the different switching directions.

To account for interactions, the considerations of a single grain have to be extended to a polycrystalline body. Macroscopic stress and electric displacement are microscopic volume averages. In this respect, grains are assumed to be homogeneous in the present work. Thus, the volume average of stress $\langle \sigma_{ij} \rangle$ and electric displacement $\langle D_i \rangle$ are given as an average over all grains $m = 1, \ldots, M$. The material properties of a polycrystal are calculated likewise. Further, a generalized Voigt approximation is assumed, thus the strain and the electric field are constant in each grain. To calculate an interaction tensor, one has to formulate Eq. (3) as an average. With the assumptions mentioned above, the constitutive equation of average stress results in:

$$\langle \sigma_{ij} \rangle = \langle C_{ijkl} \rangle \left(\varepsilon_{kl} - \langle \varepsilon_{kl}^{irr} \rangle \right) - \langle e_{lij} \rangle \, E_l. \tag{6}$$

For an electromechanical loading $\langle \sigma_{ij} \rangle$ and E_l are prescribed and only the strain ε_{kl} is unknown:

$$\varepsilon_{kl} = \langle C_{ijkl} \rangle^{-1} \left\{ \langle \sigma_{ij} \rangle + \langle e_{lij} \rangle \, E_l \right\} + \langle \varepsilon_{kl}^{irr} \rangle. \tag{7}$$

With Eq. (8) it is possible to determine an interaction tensor

$$\varepsilon_{kl}^{int(m)} = \varepsilon_{kl} - \varepsilon_{kl}^{irr(m)} \tag{8}$$

and to calculate the residual stress

$$\sigma_{ij}^{(m)} = C_{ijkl}^{(m)} \left(\varepsilon_{kl} - \varepsilon_{kl}^{irr(m)} \right) - e_{lij}^{(m)} \, E_l \tag{9}$$

of each grain m.

3 Numerical results

The numerical results presented in this section refer to a tetragonal unit cell. A pure electric loading E_2 is considered and 25 grains are assumed. In Figure 2 the numerical results for the strain ε_{22} and the residual stress into the loading direction σ_{22} are presented. The numerical

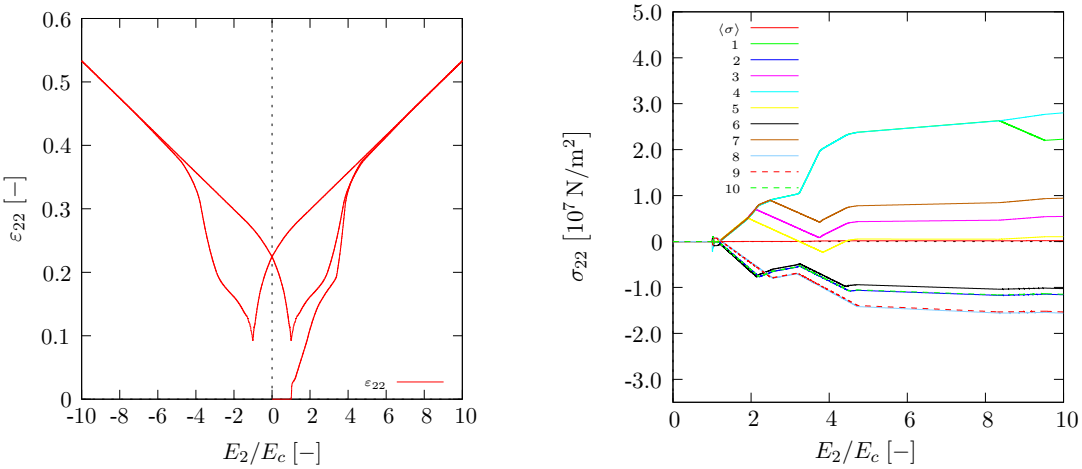

a) Butterfly hysteresis loop b) residual stress vs. electric field

Figure 3: Numerical results fo a polycrystalline material with a pure electric loading

result of the butterfly hysteresis loop is in a good agreement with the solution of the FEM. The residual stress σ_{22} shows, that there are some grains with a tensile and other with a compressive stress, however the average $\langle\sigma_{22}\rangle$ is equal to zero. That agrees with the boundary condition mentioned above.

4 Closure

A condensed approach for ferroelectric ceramics with tetragonal or rhombohedral unit cells has been presented. Being mechanically, electrostatically and thermodynamically consistent, it provides a powerful and efficient tool to investigate the inelastic constitutive behavior of multifunctional materials without the requirement of expensive FE calculations.

REFERENCES

[1] S. C. Hwang, C. S. Lynch, and R. M. McMeeking. Ferroelectric/ferroelastic interactions and a polarization switching model, *Acta Metallurgica et Materialia*, 43(5): 2073–2084, 1995.

[2] J. E. Huber, N. A. Fleck, C. M. Landis and R. M. McMeeking. A constitutive model for ferroelectric polycrystals, *Journal of the Mechanics and Physics of Solids*, 47(8): 1663–1697, 1999.

[3] V. Z. Patron and B.A. Kudryavtsev. *Electromagnetoelasticity*. Gordon and Breach Science Publishers, New York, 1988.

[4] M. Kamlah, A. C. Liskowsky, R. M. McMeeking and H. Balke. Finite element simulation of a polycrystalline ferroelectric based on a multidomain single crystal switching model, *International Journal of Solids and Structures*, 42(9–10): 2949–2964, 2005.

STRAIN-INDUCED PRODUCT PROPERTIES OF TWO-PHASE MAGNETO-ELECTRIC COMPOSITES

M. Labusch[1], M.-A. Keip[2], J. Schröder[1], and D.C. Lupascu[3]

[1] Institute of Mechanics, Department of Civil Engineering, Faculty of Engineering, University of Duisburg-Essen
Universitätsstraße 15, 45141 Essen, Germany
e-mail: matthias.labusch@uni-due.de, j.schroeder@uni-due.de

[2] Institute of Applied Mechanics (CE), Chair I, University of Stuttgart
Pfaffenwaldring 7, 70569 Stuttgart, Germany
e-mail: keip@mechbau.uni-stuttgart.de

[3] Institute for Materials Science, Department of Civil Engineering, Faculty of Engineering, University of Duisburg-Essen
Universitätsstraße 15, 45141 Essen, Germany
e-mail: doru.lupascu@uni-due.de

Abstract. *Coupling between electric and magnetic fields may find application in sensor technology and data storage. Since natural materials are generally characterized by a very low magneto-electric (ME) coupling effect at room temperature, synthetic materials consisting of magnetically and electrically active phases are promising candidates for the generation of a high ME coupling effect. These ME composites generate the ME coupling as a strain-induced product property. Due to the significant influence of the microstructure on the ME effect, we derive a two-scale homogenization framework, which allows for the consideration of microscopic morphologies. A real two-phase composite microstructure consisting of a electro-active matrix with magneto-active inclusions is simulated and the results are compared to experimental measurements.*

1 Introduction

In the last decades there has been a steady increase in attention to magneto-electric (ME) materials that couple polarization and magnetization with each other. By using such materials smart applications in sensor and actuator technology, like electrical magnetic-field sensors as well as electric-write magnetic-read memories, see e.g. [1,2], can be realized. Such ME multiferroics have been investigated intensively, see for example [3,5,8]. Since the ME coupling in natural materials at room temperature is very weak, the development of *ME composite materials* with much higher ME coefficients becomes very important. Such ME composites, consisting of electro-active and magneto-active phases, produce the desired ME coefficients as a *strain-induced product property*, see e.g. [9,10,11,13], where one distinguishes between the direct and the converse ME effect. The direct effect characterizes magnetically induced polarization: an applied magnetic field yields a deformation of the magneto-active phase that is transferred to the electro-active phase, which results in a *strain-induced polarization* in the electric phase. On the other hand, the converse effect is characterized by an electrically activated magnetization.
However, this macroscopic response is a result of the microscopic interaction between two

phases and significantly depends on the underlying microscopic properties. In order to explicitly account for the microscopic morphology of such composites, we make use of a scale transition in the framework of the FE^2-method. This homogenization procedure allows for the determination of macroscopic effective properties in consideration of attached representative volume elements ($\mathcal{RVE}$s) in each macroscopic integration point, see, for example, [7] for the application to electro-mechanically coupled problems. In the present contribution the homogenization approach is extended to magneto-electro-mechanically coupled boundary value problems and applied to realistic two-phase magneto-electric microstructures. The resulting effective ME coefficient is compared to experimental measurements obtained by [4].

2 Theoretical framework

The main idea of the FE^2-method is to attach a representative volume element ($\mathcal{RVE}$) in each macroscopic integration point instead of solving a material law. The material response is then given by solving the microscopic boundary value problem on the $\mathcal{RVE}$, which is driven by macroscopic quantities. Subsequently, the homogenized effective properties are given back to the macroscale, where the macroscopic boundary value problem is solved.

2.1 Magneto-electro-mechanical boundary value problems and scale transition

The considered body on the macroscale is denoted as $\mathcal{B} \subset \mathbb{R}^3$ and parameterized with the coordinates $\overline{\boldsymbol{x}}$. Furthermore, the macroscopic displacement field, the macroscopic electric potential as well as the magnetic potential are defined as $\overline{\boldsymbol{u}}$, $\overline{\phi}_e$ and $\overline{\phi}_m$, respectively. Depending on theses variables the basic kinematic and magnetic quantities as well as the balance of linear momentum, the Gauß's law of electrostatics and the Gauß's law of magnetostatics are given by

$$\begin{aligned} &\overline{\boldsymbol{\varepsilon}} = \text{grad}^{sym}_{\overline{\boldsymbol{x}}} \overline{\boldsymbol{u}} \,, \qquad \overline{\boldsymbol{E}} = -\text{grad}_{\overline{\boldsymbol{x}}} \overline{\phi}_e \quad \text{and} \quad \overline{\boldsymbol{H}} = -\text{grad}_{\overline{\boldsymbol{x}}} \overline{\phi}_m \,, \\ &\text{div}_{\overline{\boldsymbol{x}}} \overline{\boldsymbol{\sigma}} + \overline{\boldsymbol{f}} = \boldsymbol{0} \,, \quad \text{div}_{\overline{\boldsymbol{x}}} \overline{\boldsymbol{D}} = q_e \qquad \text{and} \quad \text{div}_{\overline{\boldsymbol{x}}} \overline{\boldsymbol{B}} = 0 \,, \end{aligned} \tag{1}$$

with the macroscopic symmetric linear strain tensor $\overline{\boldsymbol{\varepsilon}}$, the electric and magnetic field vectors $\overline{\boldsymbol{E}}$ and $\overline{\boldsymbol{H}}$, the Cauchy stress tensor $\overline{\boldsymbol{\sigma}}$, the vector of body forces $\overline{\boldsymbol{f}}$, the vector of dielectric displacements $\overline{\boldsymbol{D}}$, the free charge carriers q_e and the vector of magnetic flux density $\overline{\boldsymbol{B}}$. In order to connect the macroscopic magneto-electro-mechanical quantities to their corresponding microscopic quantities for the performed scale transition, we define the macroscopic variables in terms of suitable volume integrals, see [12], as

$$\overline{\boldsymbol{\xi}} = \int_{\mathcal{RVE}} \boldsymbol{\xi} \, dv \quad \text{with} \quad \boldsymbol{\xi} := \{\boldsymbol{\varepsilon}, \boldsymbol{\sigma}, \boldsymbol{E}, \boldsymbol{D}, \boldsymbol{H}, \boldsymbol{B}\} \tag{2}$$

The $\mathcal{RVE}$ is driven by boundary conditions that arise as a consequence of macroscopic fields. These boundary conditions have to ensure energetic consistency of the scales, derived by exploring a *scale transition*. For this purpose, we decompose the microscopic fields into constant macroscopic fields $\overline{\bullet}$ and fluctuation parts $\widetilde{\bullet}$ as $\boldsymbol{\xi} = \overline{\boldsymbol{\xi}} + \widetilde{\boldsymbol{\xi}}$. Energetic consistency is then ensured by postulating a generalized macrohomogeneity condition of the form

$$\overline{\boldsymbol{\sigma}} : \dot{\overline{\boldsymbol{\varepsilon}}} - \overline{\boldsymbol{D}} \cdot \dot{\overline{\boldsymbol{E}}} - \overline{\boldsymbol{B}} \cdot \dot{\overline{\boldsymbol{H}}} = \int_{\mathcal{RVE}} \boldsymbol{\sigma} : \dot{\boldsymbol{\varepsilon}} - \boldsymbol{D} \cdot \dot{\boldsymbol{E}} - \boldsymbol{B} \cdot \dot{\boldsymbol{H}} \, dv, \tag{3}$$

in this context we refer to [7]. Boundary conditions satisfying the macrohomogeneity condition are the following periodic boundary conditions

$$\{\widetilde{\boldsymbol{u}}, \widetilde{\phi}_e, \widetilde{\phi}_m\}(\boldsymbol{x}^+) = \{\widetilde{\boldsymbol{u}}, \widetilde{\phi}_e, \widetilde{\phi}_m\}(\boldsymbol{x}^-) \quad \text{and} \quad \{\boldsymbol{t}, Q, \zeta\}(\boldsymbol{x}^+) = -\{\boldsymbol{t}, Q, \zeta\}(\boldsymbol{x}^-) \tag{4}$$

where $\boldsymbol{x}^+$ and $\boldsymbol{x}^-$ denote points on opposite faces of a periodic unit cell and $\widetilde{\boldsymbol{u}}$ are fluctuations of the mechanical displacements.

2.2 Constitutive framework and effective ME coefficient

For the analysis of the effective ME behavior of the composite, we consider a transversely isotropic material law for both phases and use the constitutive framework proposed in [6]. Without going into detail, the constitutive effective quantities of the composite are defined as

$$\begin{aligned} \Delta\overline{\boldsymbol{\sigma}} &= \overline{\mathbb{C}} : \Delta\overline{\boldsymbol{\varepsilon}} - \overline{\boldsymbol{e}}^T \cdot \Delta\overline{\boldsymbol{E}} - \overline{\boldsymbol{q}}^T \cdot \Delta\overline{\boldsymbol{H}} \,, \\ -\Delta\overline{\boldsymbol{D}} &= -\overline{\boldsymbol{e}} : \Delta\overline{\boldsymbol{\varepsilon}} - \overline{\boldsymbol{\epsilon}} \cdot \Delta\overline{\boldsymbol{E}} - \overline{\boldsymbol{\alpha}}^T \cdot \Delta\overline{\boldsymbol{H}} \,, \\ -\Delta\overline{\boldsymbol{B}} &= -\overline{\boldsymbol{q}} : \Delta\overline{\boldsymbol{\varepsilon}} - \overline{\boldsymbol{\alpha}} \cdot \Delta\overline{\boldsymbol{E}} - \overline{\boldsymbol{\mu}} \cdot \Delta\overline{\boldsymbol{H}} \,. \end{aligned} \tag{5}$$

Although the ME coefficient $\boldsymbol{\alpha}$ is zero for each of the two phases, the overall macroscopic ME modulus of the composite $\overline{\boldsymbol{\alpha}}$ is in general non-zero since it is activated by the electric- or magnetic-field induced microscopic deformations. This macroscopic property is defined as

$$\overline{\boldsymbol{\alpha}} = \frac{\partial \overline{\mathbf{B}}}{\partial \overline{\mathbf{E}}} = \left[\frac{\partial \overline{\mathbf{D}}}{\partial \overline{\mathbf{H}}}\right]^T . \tag{6}$$

For the simulation of the ME coefficients and the comparison to experimental measurements in [4], we use a realistic microstructure, shown in Figure 1.

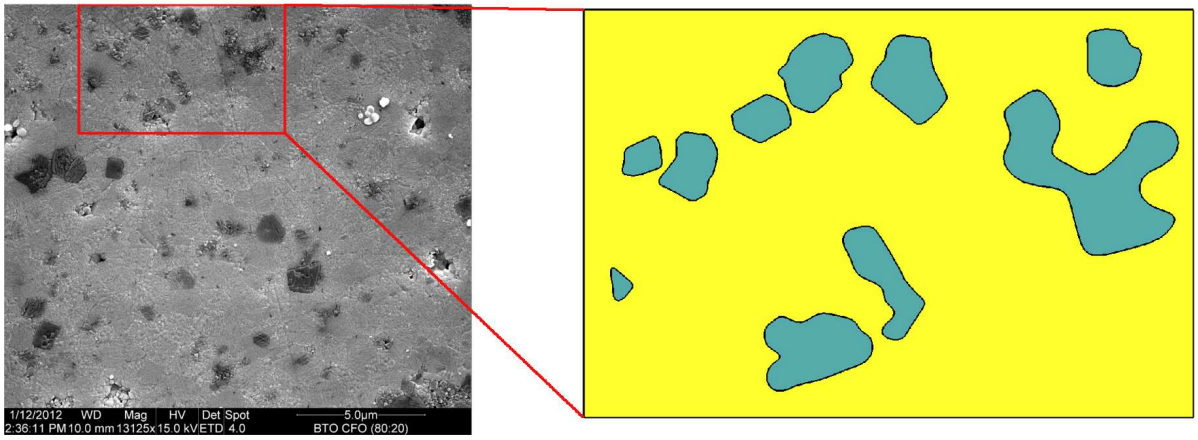

Figure 1: Real composite microstructure with representative volume element analyzed in the computations.

Acknowledgements We gratefully acknowledge the financial support by the “Deutsche Forschungsgemeinschaft” (DFG), research group “Ferroische Funktionsmaterialien - Mehrskalige Modellierung und experimentelle Charakterisierung”, project 1 (SCHR 570/12-1) and project 2 (LU 729/12). Furthermore, we acknowledge the comprehensive discussions and suggestions by Dr. Vladimir V. Shvartsman.

REFERENCES

[1] W. Eerenstein, M. Wiora, J.L. Prieto, J.F. Scott and N.D. Mathur. Giant sharp and persistent converse magnetoelectric effects in multiferroic epitaxial heterostructures, *Nature Materials*, 6: 348–351, 2007.

[2] M. Bibes and A. Barthélémy. Multiferroics: Towards a magnetoelectric memory, *Nature Materials*, 7: 425–426, 2008.

[3] M. Labusch, M. Etier, D.C. Lupascu, J. Schröder and M.-A. Keip. Product properties of two-phase magneto-electric composite: Synthesis and numerical modeling, *Computational Mechanics*, 466, 2014.

[4] M. Etier, Y. Gao, V.V. Shvartsman, D.C. Lupascu, J. Landers and H. Wende. Magnetoelectric properties of $0.2CoFe_2O_4$-$0.8BaTiO_3$ composite prepared by organic method, *Proceedings of the ECAPD*, 1–4, 2012.

[5] S.W. Cheong and M. Mostovoy. Multiferroics: a magnetic twist for ferroelectricity, *Nature Materials*, 6(1): 13–20, 2000.

[6] J. Schröder and D. Gross. Invariant formulation of the electromechanical enthalpy function of transversely isotropic piezoelectric materials, *Archive of Applied Mechanics*, 73: 533–552, 2004.

[7] J. Schröder and M.-A. Keip. Two-scale homogenization of electromechanically coupled boundary value problems, *Computational Mechanics*, 50: 229–244, 2012.

[8] T. Zohdi. Simulation of coupled microscale multiphysical-fields in particulate-doped dielectrics with staggered adaptive FDTD, *Computer Methods in Applied Mechanics and Engineering*, 199: 3250–3269, 2010.

[9] G. Srinivasan. Magnetoelectric composites, *Annual Review of Materials Research*, 40: 1–26, 2010.

[10] J. van Suchtelen. Product properties: a new application of composite materials, *Philips Research Reports*, 27: 28–37, 1972.

[11] C.W. Nan. Magnetoelectric effect in composites of piezoelectric and piezomagnetic phases, *Physical Review B*, 50: 6082–6088, 1994.

[12] J. Schröder. Derivation of the localization and homogenization conditions for electromechanically coupled problems, *Computational Materials Science*, 46(3): 595–599, 2012.

[13] W. Eerenstein, N.D. Mathur and J.F. Scott. Multiferroic and magnetoelectric materials, *Nature*, 442(7104): 759–765, 2006.

FRACTURE AND ADHESION IN AN INFINITE FERROELECTRIC STRIP SUBJECT TO ELECTRIC FIELD AND STRESS

Robert M. McMeeking[1], Chad M. Landis[2]

[1] Materials Department and Department of Mechanical Engineering, University of California
Santa Barbara, California 93106, USA

and School of Engineering, University of Aberdeen, Aberdeen AB24 3UE, Scotland
email: rmcm@engineering.ucsb.edu

[2] Department of Aerospace Engineering and Engineering Mechanics, University of Texas
Austin, Texas 78712, USA
email: landis@utexas.edu

Abstract. *The fracture of dielectrics and ferroelectrics can exhibit interactions between the effects of mechanical and electrostatic fields; in the case of the ferroelectric material these interactions are over and above the direct coupling of ferroelectricity. A simple configuration that encompasses some of these phenomena is that of an infinite strip of finite width between two attached electrodes, i.e. an infinite capacitor. The electrostatic or Maxwell stresses must be accounted for to allow analysis of the behavior of this system. These stresses account for the action at a distance that occurs between the charges on the electrodes and are associated with the attraction that occurs as a consequence. This attraction occurs whether the strip is intact or separated by a gap within the dielectric or ferroelectric, representative of a crack that may be present in the system. In some cases where the loading system is evolving, either by adjustment of the strain between the electrodes or the electric potential difference, there may occur a jump into contact eliminating a gap or a sudden separation creating a gap. In this sense, the system has features analogous to adhesive behavior where similar jumps into and out of contact can occur. These phenomena play a role in determining how fracture can occur in the dielectric or ferroelectric, and constitute aspects of the physics that control whether unstable fracture or unstable reattachment may or may not occur according to the relevant energy balance and rates of change of the driving force for fracture relative to the fracture toughness.*

1 Overview

The manner in which electrostatic and mechanical fields interact in the fracture of dielectrics and ferroelectrics has long been a puzzle that has proved to be difficult to resolve due to the paucity of experimental data and the lack of completely rigorous theories in regard to the relevant phenomena playing a role in the fracture processes. One of the challenges has been the fact that a complete picture of the problem in the presence of a crack can only be obtained by inclusion of electrostatic or Maxwell stresses, since otherwise a proper accounting of the interaction among charges present cannot be given. An obvious example is a vacuum capacitor, where the attraction between the electrodes must be represented by a Maxwell stress in the gap between them, so that the electric field that one normally associates with such a configuration is alone an incomplete picture. Of course, the Maxwell stress and the electric field have an intimate connection, but the attraction cannot be represented mechanically by anything other than the Maxwell stress.

We therefore consider the problem of an infinite strip of dielectric or ferroelectric material between 2 electrodes along with the possibility that a crack may separate the system parallel to the electrodes. Far away from the crack tip the strip is either fully intact or is a pair of dielectric or ferroelectric layers with a gap between them. The Maxwell stress in the gap where it exists allows for the accounting of the attraction across the gap, just as it allows for the same aspects in the dielectric or ferroelectric itself. We therefore analyze the electric fields and the stress, including the electrostatic or Maxwell stress, in both the intact segment of the capacitor and the segment where the crack separates it with a gap.

Due to nonlinear phenomena associated with the straining of the dielectric or ferroelectric material and the stress generated within it and the gap, unstable situations can arise. For example, in certain circumstances as the strain between the electrodes is held fixed and the electric potential difference between them is increased, the gap in the cracked segment can be closed by a jump into contact when the situation loses stability. Similarly, as the strain between the electrodes is increased and the potential difference between them held fixed, the gap can suddenly and unstably separate where previously it has not existed despite the material already having a crack present. The question of whether this jump into contact and this jump out of contact can occur is a stability issue, just as is the question of the propagation of the crack into segments of the capacitor that has previously been intact.

We therefore analyze both the jump into contact and the jump out of contact for the infinite capacitor having a dielectric that can be isotropic or that is a ferroelectric along with the phenomenon of the propagation of the crack by fracturing previously intact material. The propagation of the crack is considered to occur when the energy release rate, as the driving force, exceeds the toughness of the material. The issue of stable versus unstable growth is addressed as is the question the unstable jump into and jump out of contact. We find that these aspects of the system behavior interact in a rich a complex manner and lead to interesting phenomena in the interaction of electrostatics and mechanics within the overall problem of the fracture of a dielectric or ferroelectric material.

As such, the analysis extends the previous treatment [1] of the subject that hinted at some of the above phenomena but that did not bring them fully to light in the approach that was adopted.

REFERENCES

[1] C.M. Landis and R.M. McMeeking. Modeling of Fracture in Ferroelectric Ceramics, *Smart Materials and Structures: Active Materials: Behavior and Mechanics* (C.S. Lynch, Ed.), *Proceedings of SPIE*, 3992: 176-184, 2000.

ON INVERSE-MOTION-BASED FORM FINDING AND CONFIGURATIONAL MECHANICS FOR ELECTRO-ACTIVE POLYMERS

A. Menzel[1,2], R. Denzer[1], A. Ask[3], and M. Ristinmaa[2]

[1] Institute of Mechanics, Department of Mechanical Engineering, TU Dortmund
Leonhard-Euler-Str. 5, Dortmund, Germany
e-mail: andreas.menzel@udo.edu, ralf.denzer@udo.edu

[2] Division of Solid Mechanics, Lund University
P.O. Box 118, 221 00 Lund, Sweden
e-mail: andreas.menzel@solid.lth.se, matti.ristinmaa@solid.lth.se

[3] ABB AB, Corporate Research
Forskargränd 7, 72178, Västeras, Sweden
e-mail: anna.ask@se.abb.com

Abstract. *Electroactive polymers exhibit large mechanical deformation under an applied electrical field. This electro-mechanical coupling is an attractive property for actuators, e.g., artificial muscles for micro-robotics. In this work we focus on the formulation of geometrically nonlinear electroactive polymers as established by the balance of linear momentum and Gauss law. These balance laws govern the evolution of the deformation and the electric field and can be given for both, the classical direct and the inverse motion problem. The latter leads us first to the notion of configurational forces where the electric field and the viscous behaviour of electroactive polymers can be understood as a source of inhomogeneity and thus influence in the case of a cracked actuator the crack driving forces. Moreover, the inverse motion problem can be used to solve the problem in form finding applications for the case of electroelasticity – in other words, the computation of an undeformed and load free configuration for a given deformed configuration and given boundary conditions. This is of practical interest for the design of actuators such as grippers. We address issues of implementation of the quasi-incompressible case and discuss representative numerical examples.*

1 Introduction

An important class of materials that exhibits an electromechanical response are electroactive polymers (EAP). EAP convert electrical energy directly into mechanical energy through their material response and are commonly used in actuators and sensors. Their performance is comparable with that of natural muscles. Together with the electromechanical behaviour, the typical properties of polymers – for instance, light weight, high flexibility, and low cost – make EAP highly interesting in technical applications such as micro-robotics, biomimetics, and energy harvesting; see [1].

Only a few works in the literature deal with the determination of the undeformed shape of a hyperelastic body in the purely mechanical case. The original numerical scheme was introduced

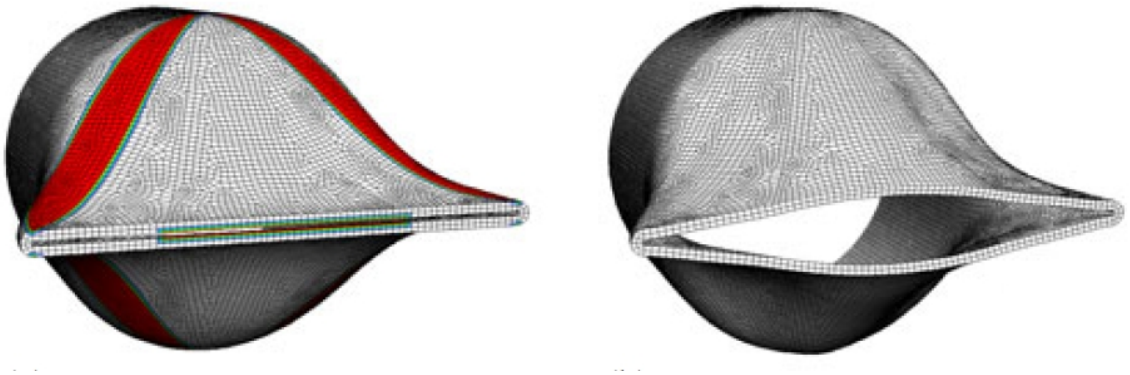

Figure 1: Cylindrical sealing – inverse form finding: Given deformed configuration (left) and initially unknown undeformed configuration (right); cf. [5].

in [2] and, later on, interpreted in the more general framework of configurational mechanics in [3]. Details on the extension to the case of finite deformation electromechanics, as addressed in this contribution and related to the framework for electromechanics established in [4], are discussed in [5].

When EAPs undergo cyclic deformations, the predictive modelling of fracture-related effects such as fatigue crack growth are of high interest. The framework of configurational forces provides a suitable theory to calculate crack driving forces; see [6,7]. In this contribution, we address the framework of material forces with application to the electro-viscoelastic model as introduced, and calibrated, in [8].

2 Inverse-motion problem for quasi-incompressible electro-elasticity

Let $\boldsymbol{x} = \boldsymbol{\varphi}(\boldsymbol{X}, t) \in \mathcal{B}_t$ denote the direct motion, whereas $\boldsymbol{X} = \boldsymbol{\Phi}(\boldsymbol{x}, t) \in \mathcal{B}_0$ characterises the inverse motion. The related deformation gradients are introduced as $\boldsymbol{F} = \nabla_{\boldsymbol{X}} \boldsymbol{\varphi}$ and $\boldsymbol{f} = \nabla_{\boldsymbol{x}} \boldsymbol{\Phi}$, both possessing non-negative determinants J and j, respectively. Their isochoric parts are represented as $\bar{\boldsymbol{F}}$ and $\bar{\boldsymbol{f}}$. Similarly, we assume that the electric field can be derived as the gradient of an electric potential with referential representation $\boldsymbol{E} = -\nabla_{\boldsymbol{X}} \phi$ and spatial form $\boldsymbol{e} = -\nabla_{\boldsymbol{x}} \phi$.

In view of the quasi-static inverse motion problem, we assume the existence of a free energy density $\widehat{\Omega}_t(\vartheta, \bar{\boldsymbol{f}}, \boldsymbol{e})$ per unit volume in $\mathcal{B}_t$, wherein the inverse motion dilatation is denoted by $\vartheta(\boldsymbol{x})$ and the inverse motion pressure will is represented by $q(\boldsymbol{x})$. The total potential energy of the system – in the context of the mixed formulation at hand and for the case of dead loads – reads

$$\begin{aligned} l(\boldsymbol{\Phi}(\boldsymbol{x}),\, \phi(\boldsymbol{x}),\, \vartheta(\boldsymbol{x}),\, q(\boldsymbol{x})) \;=\; & \int_{\mathcal{B}_t} [\, \widehat{\Omega}_t(\vartheta,\, \bar{\boldsymbol{f}}, \boldsymbol{e}) + q\,[\, j - \vartheta\,]] \,\mathrm{d}v \\ & - \int_{\mathcal{B}_t} \boldsymbol{\Phi} \cdot \boldsymbol{B}_t \,\mathrm{d}v - \int_{\partial\mathcal{B}_t} \boldsymbol{\Phi} \cdot \boldsymbol{T}_t \,\mathrm{d}s - \int_{\partial\mathcal{B}_t} \phi\, d_t \,\mathrm{d}s \end{aligned} \tag{1}$$

with $\boldsymbol{T}_t$ and d_t the mechanical and electrical flux with respect to the outward surface normal and the mechanical volume forces $\boldsymbol{B}_t$. Let the inverse motion Piola-type total stresses be denoted by $\boldsymbol{p}$ and, together with the electric displacements $\boldsymbol{d}$, be defined in the context of stationarity of the total inverse motion potential $l(\boldsymbol{\Phi},\, \phi,\, \vartheta,\, q)$. We assume that possible defects present in the material will not move relative to the ambient material and obtain

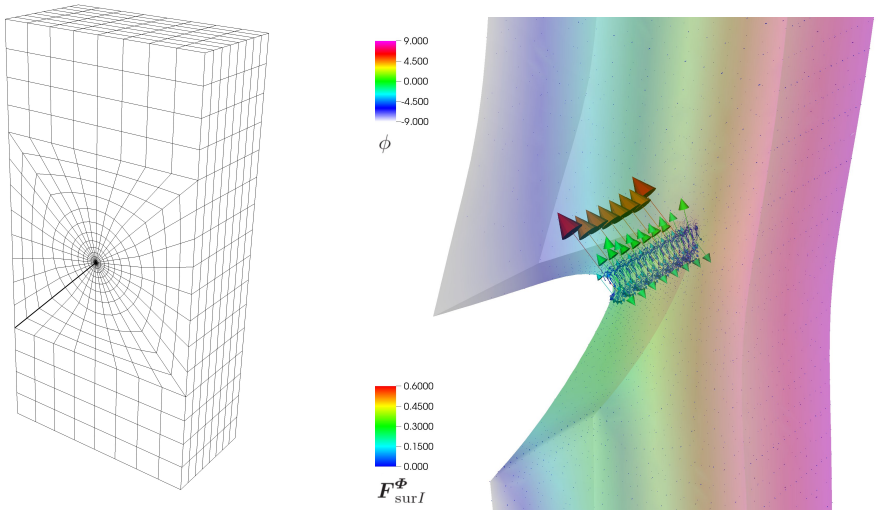

Figure 2: Three-dimensional crack – mixed-mode loading conditions: Discretisation (left) and discrete configurational surface forces at crack front (right); R. Denzer and A. Menzel [2014].

$$
\begin{aligned}
\delta l_1|_{\boldsymbol{x}} &= \int_{\mathcal{B}_t} \nabla_{\boldsymbol{x}} \delta\boldsymbol{\Phi} : \boldsymbol{p}\,\mathrm{d}v - \int_{\mathcal{B}_t} \delta\boldsymbol{\Phi}\cdot\boldsymbol{B}_t\,\mathrm{d}v - \int_{\partial\mathcal{B}_t} \delta\boldsymbol{\Phi}\cdot\boldsymbol{T}_t\,\mathrm{d}s \;=\; 0 \\
\delta l_2|_{\boldsymbol{x}} &= \int_{\mathcal{B}_t} \nabla_{\boldsymbol{x}} \delta\phi\cdot\boldsymbol{d}\,\mathrm{d}v + \int_{\partial\mathcal{B}_t} \delta\phi\, d_t\,\mathrm{d}s \;=\; 0 \\
\delta l_3|_{\boldsymbol{x}} &= \int_{\mathcal{B}_t} \delta q\,[\,j-\vartheta\,]\,\mathrm{d}v \;=\; 0 \\
\delta l_4|_{\boldsymbol{x}} &= \int_{\mathcal{B}_t} \delta\vartheta\left[\,\frac{\partial\widehat{\Omega}_t}{\partial\vartheta} - q\right]\mathrm{d}v \;=\; 0
\end{aligned}
\tag{2}
$$

Solving this system of coupled equations in discrete form, here by means of the finite element method, enables us to simulate complex boundary value problems; see Fig. 1 for an example, where the deformed configuration together with loading and boundary conditions are given and the undeformed, or rather initial, configuration is obtained as solution of the electromechanically coupled inverse motion problem. This illustrates that solving the inverse motion problem, the shape of the body can be tailored to produce a specific deformed configuration.

3 Material forces for quasi-incompressible electro-viscoelasticity

In order to additionally account for viscous effects of the EAPs considered, (referential and symmetric) internal variables $\boldsymbol{C}_{v\alpha}$ are introduced, each of which represents one Maxwell element α. The evolution of these internal variables is chosen to be caputured by

$$
\dot{\boldsymbol{C}}_{v\alpha} = \dot{\Gamma}_\alpha\,\boldsymbol{C}_{v\alpha}\cdot[\,\boldsymbol{C}_{v\alpha}^{-1}\cdot\partial_{\boldsymbol{C}_{v\alpha}}\widehat{\Omega}_0]^{\mathrm{dev}} \tag{3}
$$

This renders the material volume forces and the Eshelby stresses for the electro-viscoelastic problem at hand to take the representations

$$
\bar{\boldsymbol{\Sigma}} = \widehat{\Omega}_0\,\boldsymbol{I} - \boldsymbol{F}^{\mathrm{t}}\cdot\bar{\boldsymbol{P}} + \boldsymbol{E}\otimes\boldsymbol{D} \qquad \boldsymbol{B}_0 = -\sum_\alpha \partial_{\boldsymbol{C}_{v\alpha}}\Omega_0 : \nabla_{\boldsymbol{X}}\boldsymbol{C}_{v\alpha} - \boldsymbol{F}^{\mathrm{t}}\cdot\boldsymbol{b}_0 \tag{4}
$$

Material forces related to the material motion quasi-static balance of linear momentum form $\nabla_{\boldsymbol{X}}\cdot\bar{\boldsymbol{\Sigma}} + \boldsymbol{B}_0 = \boldsymbol{0}$ can – in a finite element context – be computed as a post-processing step.

The representation of the discrete material surface force at node I results in

$$\boldsymbol{F}^{\boldsymbol{\Phi}}_{\mathrm{sur}I} = \mathop{\mathbf{A}}_{e=1}^{\mathrm{n_{el}}} \int_{\mathcal{B}_0^e} \bar{\boldsymbol{\Sigma}} \cdot \nabla_{\boldsymbol{X}} N^A - N^A \, \boldsymbol{B}_0 \, \mathrm{d}V \tag{5}$$

Fig. 2 shows an illustration of crack driving material forces along a crack front. The specimen is pre-stretched in longitudinal direction before an electric field is applied in transverse direction. Due to the initial crack orientation, mixed-mode loading is induced. Fig. 2 shows the almost fully relaxed state, whereas the material forces exhibit time-dependent effects due to the viscosity of the underlying material. Future work shall address the crack propagation problem.

REFERENCES

[1] K.J. Kwang and S. Tadokoro. *Electroactive Polymers for Robotic Applications*, Springer, 2007.

[2] S. Govindjee and P.A. Mihalic. Computational methods for inverse finite elastostatics. *Computer Methods in Applied Mechanics and Engineering*, 136:47–57, 1996.

[3] P. Steinmann, M. Scherer, and R. Denzer. Secret and joy of configurational mechanics: from foundations in continuum mechanics to applications in computational mechanics. *Journal of Applied Mathematics and Mechanics*, 89:614–630. 2009.

[4] A. Dorfmann and R.W. Ogden. Nonlinear electroelasticity. *Acta Mechanica*, 174:167–183. 2005.

[5] A. Ask, R. Denzer, A. Menzel, and M. Ristinmaa. Inverse-motion-based form finding for quasi-incompressible finite electroelasticity. *International Journal for Numerical Methods in Engineering*, 94:554–572. 2013.

[6] C. Trimarco and G.A. Maugin. Material mechanics of electromagnetic bodies, In *Configurational Mechanics of Materials*, vol. 427 of *CISM Courses and Lectures*, 129–179, Springer, 2001.

[7] D.K. Vu and P. Steinmann. Theoretical and numerical aspects of the material and spatial settings in nonlinear electro-elastostatics. *International Journal of Fracture*, 147:109–116, 2007.

[8] A. Ask, A. Menzel, and M. Ristinmaa. Electrostriction in electro-viscoelastic polymers. *Mechanics of Materials*, 50:9–21, 2012.

THE LIPPMANN-SCHWINGER EQUATION IN ELASTICITY FOR POROUS MEDIA

Matti Schneider[1], **Matthias Kabel**[2]

[1] Department of Lightweight Structures and Polymer Technology, Faculty of Mechanical Engineering,
Chemnitz University of Technology
Reichenhainer Straße 70, 09126 Chemnitz, Germany
e-mail: matti.schneider@mb.tu-chemnitz.de

[2] Department of Flow and Materials Simulation, Fraunhofer Institute for Industrial Mathematics ITWM
Fraunhofer-Platz 1, 67663 Kaiserslautern
e-mail: matthias.kabel@itwm.fraunhofer.de

Abstract. *The numerical computation of effective elastic properties of heterogeneous materials using the Lippmann-Schwinger equation in elasticity becomes problematic in the presence of pores. Under mild conditions on the interface of the pore the Lippmann-Schwinger equation is well-posed, but ill-conditioned. Introducing a fictitious soft material renders the problem well-conditioned again. We will discuss the exact rate of convergence of these regularized problems to the porous problem.*

1 Introduction

In [1] Moulinec-Suquet introduced a trigonometric collocation discretization of the Lippmann-Schwinger equation in elasticity

$$\varepsilon + \Gamma^0(\mathbb{C} - \mathbb{C}^0)\varepsilon = E,$$

which has become a powerful alternative to FEM or BEM computations for various reasons.

1. The discretization is based on a regular grid. It can directly handle voxel-based data (coming for instance from CT scans) and renders time-consuming meshing and assembling superfluous.

2. The Lippmann-Schwinger equation can be solved by FFT-accelerated fixed point or Krylov subspace solvers, leading to very short computation times compared to FEM or BEM.

3. The arising systems are well-conditioned in the sense that their conditioning depends solely on the contrast (i.e. the ratio $\kappa = C/c$, where c and C are lower and upper bounds on the stiffness $\mathbb{C}$). In particular, they are independent of the mesh spacing and the location/size of the inclusions.

4. Similarly to the FEM and in contrast to the BEM, the method can be adjusted to treat problems of non-linear elasticity and large deformations [2].

The method assumes a perfect bonding between the materials, and cannot handle more interesting interfacial conditions.
The above considerations apply only if the contrast κ is not too large. In practice one observes that $\kappa < 10^5$ works robustly. Thus most practically relevant situations devoid of imperfections like pores or stiff inclusions can be covered.
The literature contains solvers and stopping criteria, which are claimed to work in the presence of pores [3,4]. The basic problem is usually overlooked: for a complex 3D porous medium, the Lippmann-Schwinger equation is ill-conditioned. This is a problem of the formulation and the discretization, and also appears for FEM problems. In particular, no solver can handle pores if it does not address the ill-conditioning.
We will give an example for a strange phenomenon arising from the conditioning.

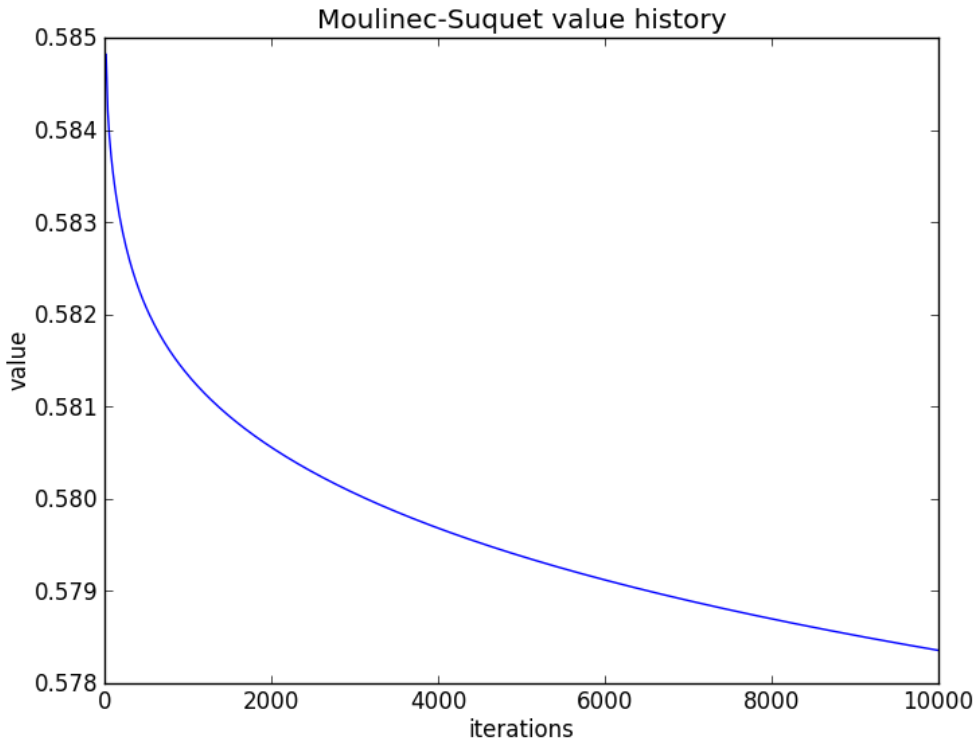

The figure above shows the history of the elastic modulus in the direction of applied strain for a single 3D spherical pore for a large number of iterations of the basic iterative scheme of Moulinec-Suquet. Apparently there is no convergence of the effective elastic constants, even for large iteration numbers. Thus, any stopping criterion, if triggered, singles out a more or less random value. The Krylov subspace solvers behave similarly, raising the question how to overcome these difficulties.
Since the original problem seems numerically intractable, we propose to regularize the problem and to solve the regularized problem.
More precisely, we introduce a fictitious material $\alpha\mathbb{B}$ into the pore, where $\mathbb{B}$ is a fixed material and $\alpha \ll 1$. From the point of view of physical intuition, this should not change the problem too much, but we can still profit from the advantages stated in the beginning.
In the talk we want to assess the magnitude of the error generated by introducing the fictitious material. We will discuss the rate of convergence as $\alpha \to 0$ and how to make use of this information numerically.

2 Problem formulation

Let V be a brick-shaped RVE in $\mathbb{R}^3$. Suppose that $\mathbb{C} : V \to L(\mathrm{Sym}(3))$ denotes a given stiffness distribution, and E a fixed macroscopic strain. Then, solving

$$\operatorname{div} \sigma = 0, \quad \sigma = \mathbb{C}(E + \varepsilon(u)),$$

where $\varepsilon(u) = \frac{1}{2}(\nabla u + \nabla u^T)$, for the displacement $u : V \to \mathbb{R}^3$ with periodic boundary conditions is equivalent to finding a solution[1] $\varepsilon : V \to \mathrm{Sym}(3)$ of the Lippmann-Schwinger equation

$$\varepsilon + \Gamma^0(\mathbb{C} - \mathbb{C}^0)\varepsilon = E$$

for any fixed elastic reference material $\mathbb{C}^0$. Here, $\Gamma^0 = \varepsilon \circ G^0 \circ \operatorname{div}$, where G^0 denotes the fundamental solution of $\operatorname{div} \circ \mathbb{C} \circ \varepsilon$ with periodic boundary conditions. The relation between the two problems is given by $\varepsilon = E + \varepsilon(u)$.
Suppose that V is the union of (the closures of) two open disjoint sets Ω_{solid} and Ω_{pore}. Suppose furthermore that $\mathbb{C} \equiv 0$ on Ω_{pore} and uniformly positive definite on Ω_{solid}. Then both equations are no longer uniquely solvable. If the interface between the domains is Lipschitz continuous, it is possible to restrict to a suitable subspace of displacements (and corresponding strains), on which both operators above are symmetric and positive definite in a suitable sense. In particular, we can prove existence and uniqueness in the corresponding spaces. The coercivity constant, however, enters the proof only indirectly, making a direct estimate difficult.
In numerical simulations we observed that the condition number of the Lippmann-Schwinger equation for 3D elasticity is extremely high, i.e. of the order $1/\text{machine precision}$. Consequently we face a mathematically well-posed, but numerically ill-conditioned system.

3 Replacing voids by soft inclusions

Fix a material $\mathbb{B}$, and consider, for $\alpha > 0$, the material

$$\mathbb{C}_\alpha(x) = \begin{cases} \mathbb{C}(x), & x \in \Omega_{solid}, \\ \alpha\mathbb{B}, & x \in \Omega_{pore}, \end{cases}$$

which corresponds to adding a fictitious material $\alpha\mathbb{B}$ to the pores. This procedure can be regarded as a Tikhonov-type regularization from a mathematical point of view. Consider the Lippmann-Schwinger equation

$$\varepsilon_\alpha + \Gamma^0(\mathbb{C}_\alpha - \mathbb{C}^0)\varepsilon_\alpha = E.$$

For fixed $\alpha > 0$, this equation is well-posed and well-conditioned, and can thus be solved by standard methods. For decreasing α, the solution procedure becomes more expensive. Furthermore, for fixed grid spacing the Moulinec-Suquet discretization becomes less accurate.

4 On convergence and the choice of the regularization

Under the hypotheses above there are positive constants C_1 and C_2, independent of α, s.t. we have

$$\frac{\alpha}{1+\alpha} C_1 \leq \|\varepsilon - \varepsilon_\alpha\|_{L^2(V)} \leq \frac{\alpha}{1+\alpha} C_2.$$

[1] It is important to distinguish the strain operator $u \mapsto \varepsilon(u)$ from the total strain $\varepsilon = E + \varepsilon(u)$. This notation is standard, but confusing at first.

The proof is based on a reformulation of the differential equations as a boundary integral equation of the second kind. As $\frac{\alpha}{1+\alpha} \approx \alpha$ for small α we have a linear convergence rate.
For the Moulinec-Suquet discretization one observes convergence that is linear in the grid spacing h, but inversely proportional to α. That means there is a positive constant C_3 with

$$\|\varepsilon_{\alpha,h} - \varepsilon_\alpha\|_{L^2(V)} \leq C_3 \frac{h}{\alpha}$$

Combining the last two estimates we obtain

$$\|\varepsilon_{\alpha,h} - \varepsilon\|_{L^2(V)} \leq C_4 \left(\alpha + \frac{h}{\alpha}\right)$$

where ε denotes the solution in the suitable subspace alluded to above. Thus, if we choose $\alpha \sim \sqrt{h}$, we obtain the convergence

$$\|\varepsilon_{\alpha,h} - \varepsilon\|_{L^2(V)} = O(\sqrt{h}),$$

which can be successfully used in conjunction with Richardson extrapolation.

REFERENCES

[1] H. Moulinec, P. Suquet. A fast numerical method for computing the linear and nonlinear properties of composites, *C. R. Acad. Sc. Paris II*, 318: 1417-1423, 1994.

[2] H. Moulinec, P. Suquet. A numerical method for computing the overall response of nonlinear composites with complex microstructure.*Comp. Meth. Appl. Mech. Engng.*, 157 69-94, 1998.

[3] J. C. Michel, H. Moulinec, P. Suquet. A computational method based on augmented Lagrangians and Fast Fourier Transforms for composites with high contrast, *Comput. Modelling Engng. Sc.*, 1(2), 79-88, 2000.

[4] V. Monchiet, G. Bonnet: A polarization-based FFT iterative scheme for computing the effective properties of elastic composites with arbitrary contrast, *Int. J. Numer. Meth. Engng,* 89: 1419–1436, 2012.

PHASE FIELD MODELING IN FERROELECTRIC MATERIALS IN THE CONTEXT OF SIZE EFFECTS

D. Schrade[1], R. Müller[1], and D. Gross[2]

[1] Institute of Applied Mechanics, Department of machinery and process engineering, TU Kaiserslautern
Gottlieb-Daimler-Strae, Kaiserslautern, Germany
e-mail: schrade@rhrk.uni-kl.de

[2] Fachgebiet Festkörpermechanik, Fachbereich Bau- und Umweltingenieurwissenschaften, TU Darmstadt
Franziska-Braun-Straße 7, Darmstadt, Germany
e-mail: gross@mechanik.tu-darmstadt.de

Abstract. *An electro-mechanically coupled phase field model for ferroelectric domain evolution is presented [1]. The thermodynamical framework is based on a generalized micro-force balance from which a Ginzburg-Landau type evolution equation is derived [2]. By adopting an invariant theory for transverse isotropic piezoelectrics [3], the material tensors in the phase field model can be derived in a consistent way. In the process the invariant basis taken from the literature is extended to avoid a loss of positive definiteness of the stiffness and the dielectric tensor. After a reduction to 2d, the material constants are adapted under the condition of a vanishing micro-force [4]. Within a 2d finite element implementation [5] the model is used to study different size effects in tetragonal barium titanate thin films, nanodots, and polycrystals.*

1 Phase field model

The phase field approach is based on the electric enthalpy H which depends on the linearized strain tensor $\boldsymbol{\varepsilon}$, the electric field $\boldsymbol{E}$, and the spontaneous polarization $\boldsymbol{P}$ (the primary order parameter) and its gradient, i.e.

$$H = H(\boldsymbol{\varepsilon}, \boldsymbol{E}, \boldsymbol{P}, \nabla \boldsymbol{P}) \,, \tag{1}$$

The thermodynamical framework is based on [2] which postulates a micro-stress vector which is thermodynamically conjugate to the time rate of the order parameter. Then the integral form of the second law reads

$$\int_{\partial\mathcal{B}} \Big((\boldsymbol{\sigma}\boldsymbol{n}) \cdot \dot{\boldsymbol{u}} + (\boldsymbol{D} \cdot \boldsymbol{n})\dot{\varphi} + (\boldsymbol{\Sigma}\boldsymbol{n}) \cdot \dot{\boldsymbol{P}} \Big) \, \mathrm{d}a + \int_{\mathcal{B}} \Big(\boldsymbol{f} \cdot \dot{\boldsymbol{u}} - \rho\dot{\varphi} + \boldsymbol{\zeta} \cdot \dot{\boldsymbol{P}} \Big) \, \mathrm{d}v - \int_{\mathcal{B}} \dot{H} \, \mathrm{d}v \geq 0 \,. \tag{2}$$

Here $\boldsymbol{\sigma}$ is the mechanical stress, $\boldsymbol{D}$ is the electric displacement, $\boldsymbol{\Sigma}$ is the micro-stress tensor, $\boldsymbol{\Sigma}\boldsymbol{n}$ the micro-force vector, $\boldsymbol{u}$ represents the displacement field, φ is the electric potential, $\boldsymbol{f}$ and ρ are volume forces and volume charges, respectively, and $\boldsymbol{\zeta}$ is an external micro-force vector. The second underlying assumption is the balance of micro-forces

$$\int_{\partial\mathcal{B}} \boldsymbol{\Sigma}\boldsymbol{n} \, \mathrm{d}a + \int_{\mathcal{B}} (\boldsymbol{\zeta} + \tilde{\boldsymbol{g}}) \, \mathrm{d}v = \boldsymbol{0} \,, \tag{3}$$

where $\tilde{\boldsymbol{g}}$ is the internal micro-force which does not enter the second law. The local form of the second law reads

$$\left(\boldsymbol{\sigma}-\frac{\partial H}{\partial \boldsymbol{\varepsilon}}\right)\cdot\dot{\boldsymbol{\varepsilon}}-\left(\boldsymbol{D}+\frac{\partial H}{\partial \boldsymbol{E}}\right)\cdot\dot{\boldsymbol{E}}+\left(\boldsymbol{\Sigma}-\frac{\partial H}{\partial \nabla\boldsymbol{P}}\right)\cdot\dot{\overline{\nabla\boldsymbol{P}}}-\left(\tilde{\boldsymbol{g}}+\frac{\partial H}{\partial \boldsymbol{P}}\right)\cdot\dot{\boldsymbol{P}}\geq 0\,. \tag{4}$$

The following constitutive equations are derived from this inequality:

$$\boldsymbol{\sigma}=\frac{\partial H}{\partial \boldsymbol{\varepsilon}}\,,\quad \boldsymbol{D}=-\frac{\partial H}{\partial \boldsymbol{E}}\,,\quad \boldsymbol{\Sigma}=\frac{\partial H}{\partial \nabla\boldsymbol{P}}\,. \tag{5}$$

The residual dissipation inequality then reads

$$-\Bigg(\underbrace{\tilde{\boldsymbol{g}}+\frac{\partial H}{\partial \boldsymbol{P}}}_{\tilde{\boldsymbol{g}}_{\mathrm{dis}}}\Bigg)\cdot\dot{\boldsymbol{P}}\geq 0\,. \tag{6}$$

This inequality can be fulfilled in a sufficient way by postulating $\tilde{\boldsymbol{g}}_{\mathrm{dis}}=-\boldsymbol{\beta}\dot{\boldsymbol{P}}$, where $\boldsymbol{\beta}$ is a constitutive positive semi-definite second order inverse mobility tensor. The Ginzburg-Landau type evolution law for the order parameter is obtained by combining the residual inequality and the local form of the micro-force balance. The field equations to be solved numerically consist of this evolution equation, Gauss' Law, and the mechanical equilibrium equations:

$$\boldsymbol{\beta}\dot{\boldsymbol{P}}=\operatorname{div}\boldsymbol{\Sigma}+\boldsymbol{\zeta}-\frac{\partial H}{\partial \boldsymbol{P}}\,,\quad \operatorname{div}\boldsymbol{D}-\rho=0\,,\quad \operatorname{div}\boldsymbol{\sigma}+\boldsymbol{f}=\boldsymbol{0}\,, \tag{7}$$

where $\boldsymbol{\zeta}$ is assumed to vanish in the following.

The electric enthalpy H is assumed to be the sum of the bulk enthalpy H^{bulk}, the non-convex phase separation potential H^{sep}, and the interface gradient energy H^{int}:

$$H=H^{\mathrm{bulk}}(\boldsymbol{\varepsilon},\boldsymbol{E},\boldsymbol{P})+H^{\mathrm{sep}}(\boldsymbol{P})+H^{\mathrm{int}}(\nabla\boldsymbol{P}) \tag{8}$$

with

$$H^{\mathrm{bulk}}=\frac{1}{2}\left(\boldsymbol{\varepsilon}-\boldsymbol{\varepsilon}^{0}\right)\cdot\left[\mathbb{C}\left(\boldsymbol{\varepsilon}-\boldsymbol{\varepsilon}^{0}\right)\right]-\left(\boldsymbol{\varepsilon}-\boldsymbol{\varepsilon}^{0}\right)\cdot\mathfrak{e}^{\mathrm{T}}\boldsymbol{E}-\frac{1}{2}\boldsymbol{E}\cdot\boldsymbol{\epsilon}\boldsymbol{E}-\boldsymbol{P}\cdot\boldsymbol{E}\,, \tag{9}$$

$$H^{\mathrm{sep}}=\kappa_{\mathrm{s}}\frac{\gamma}{\epsilon}\tilde{\psi}(\boldsymbol{P})\,, \tag{10}$$

$$H^{\mathrm{int}}=\frac{1}{2}\kappa_{\mathrm{i}}\frac{\gamma\epsilon}{P_0^2}\|\nabla\boldsymbol{P}\|^2\,. \tag{11}$$

The material tensors $\mathbb{C}$, $\mathfrak{e}$, and $\boldsymbol{\epsilon}$ denote the elastic stiffness, the piezoelectric coupling constants, and the dielectric tensor, respectively; these material parameters generally depend on the polarization state, i.e. on the order parameter. The constants γ and ϵ are characteristic energy density and the characteristic width of an interface, respectively [1]. The constant P_0 designates the spontaneous polarization of the unloaded ferroelectric phase and defines the minima of the phase separation potential. The parameters κ_{s} and κ_{i} are dimensionless calibration constants.

In order to obtain the order parameter dependent material tensors, the bulk enthalpy H^{bulk} is expressed by means of an invariant formulation for transverse isotropy. The preferred direction $\boldsymbol{p}$ and the structural tensor $\mathbf{m}$ are defined by

$$\boldsymbol{p}=\frac{\boldsymbol{P}}{P_0}\,,\quad \mathbf{m}=\boldsymbol{p}\otimes\boldsymbol{p}\,. \tag{12}$$

The bulk enthalpy can then be written as

$$H^{\text{bulk}} = \frac{1}{2}\lambda I_1^2 + \mu I_2 + (\omega^{n_1}\alpha_1 + \omega^{n_6}\alpha_6)I_5 + (\omega^{n_2}\alpha_2 + \omega^{n_4}\alpha_4)I_4^2 + (\omega^{n_3}\alpha_3 + \omega^{n_5}\alpha_5)I_1 I_4 + \omega\beta_1 I_1 J_2 + \beta_2 I_4 J_2 + \omega\beta_3 K_1 + (\gamma_1 + \omega\gamma_3)J_1 + \gamma_2 J_2^2 + \gamma' J_2 \tag{13}$$

with $\omega := \operatorname{tr}\mathbf{m} = |\boldsymbol{p}|^2$, $n_i \in \mathbb{N}_0$, and the invariants

$$\begin{aligned} &I_1 = \operatorname{tr}(\boldsymbol{\varepsilon} - \boldsymbol{\varepsilon}^0)\,, && I_2 = \operatorname{tr}[(\boldsymbol{\varepsilon} - \boldsymbol{\varepsilon}^0)^2]\,, && I_3 = \operatorname{tr}[(\boldsymbol{\varepsilon} - \boldsymbol{\varepsilon}^0)^3]\,,\\ &I_4 = \operatorname{tr}[(\boldsymbol{\varepsilon} - \boldsymbol{\varepsilon}^0)\mathbf{m}]\,, && I_5 = \operatorname{tr}[(\boldsymbol{\varepsilon} - \boldsymbol{\varepsilon}^0)^2\mathbf{m}]\,, &&\\ &J_1 = \operatorname{tr}(\boldsymbol{E}\otimes\boldsymbol{E})\,, && J_2 = \operatorname{tr}(\boldsymbol{E}\otimes\boldsymbol{p})\,, && K_1 = \operatorname{tr}[(\boldsymbol{\varepsilon} - \boldsymbol{\varepsilon}^0)(\boldsymbol{E}\otimes\boldsymbol{p})]\,, \end{aligned} \tag{14}$$

where $\operatorname{tr}(\cdot)$ is the trace operator. The spontaneous strain $\boldsymbol{\varepsilon}^0(\boldsymbol{P})$ reflects the tetragonal symmetry of the poled material and is given by

$$\boldsymbol{\varepsilon}^0(\boldsymbol{P}) = \varepsilon_{\text{a}}\mathbf{1}\omega + (\varepsilon_{\text{c}} - \varepsilon_{\text{a}})\mathbf{m} \tag{15}$$

with

$$\varepsilon_{\text{a}} = (a_{\text{tet}} - a_{\text{cub}})/a_{\text{cub}}\,, \quad \varepsilon_{\text{c}} = (c_{\text{tet}} - a_{\text{tet}})/a_{\text{cub}}\,. \tag{16}$$

The parameters a_{cub}, a_{tet} and c_{tet} are the lattice constants of the cubic and the tetragonal phase. The material constants of the invariant formulation are expressed in terms of the "classic" constants by

$$\begin{aligned} &\lambda = c_{12}\,, \quad \mu = \tfrac{1}{2}(c_{11} - c_{12})\,,\\ &\alpha_1 = \begin{cases} 2c_{44} + c_{12} - c_{11} & \text{if } 2c_{44} + c_{12} - c_{11} > 0\\ -c_{11} & \text{if } 2c_{44} + c_{12} - c_{11} < 0 \end{cases},\\ &\alpha_6 = \begin{cases} 0 & \text{if } 2c_{44} + c_{12} - c_{11} > 0\\ 2c_{44} + c_{12} & \text{if } 2c_{44} + c_{12} - c_{11} < 0 \end{cases},\\ &\alpha_2 = \begin{cases} \frac{1}{2}(c_{11} + c_{33}) - 2c_{44} - c_{13} & \text{if } \frac{1}{2}(c_{11} + c_{33}) - 2c_{44} - c_{13} > 0\\ \frac{1}{2}c_{11} - 2c_{44} - c_{13} & \text{if } \frac{1}{2}(c_{11} + c_{33}) - 2c_{44} - c_{13} < 0 \end{cases},\\ &\alpha_4 = \begin{cases} 0 & \text{if } \frac{1}{2}(c_{11} + c_{33}) - 2c_{44} - c_{13} > 0\\ \frac{1}{2}c_{33} & \text{if } \frac{1}{2}(c_{11} + c_{33}) - 2c_{44} - c_{13} < 0 \end{cases},\\ &\alpha_3 = \begin{cases} c_{13} - c_{12} & \text{if } c_{13} > c_{12}\\ -c_{12} & \text{if } c_{13} < c_{12} \end{cases}, \quad \alpha_5 = \begin{cases} 0 & \text{if } c_{13} > c_{12}\\ c_{13} & \text{if } c_{13} < c_{12} \end{cases},\\ &\gamma_1 = \begin{cases} -\frac{1}{2}\bar{\epsilon}_{11} & \text{if } \bar{\epsilon}_{11} < \bar{\epsilon}_{33}\\ -\frac{1}{2}\bar{\epsilon}_{33} & \text{if } \bar{\epsilon}_{11} > \bar{\epsilon}_{33} \end{cases}, \quad \gamma_3 = \begin{cases} 0 & \text{if } \bar{\epsilon}_{11} < \bar{\epsilon}_{33}\\ \frac{1}{2}(\bar{\epsilon}_{33} - \bar{\epsilon}_{11}) & \text{if } \bar{\epsilon}_{11} > \bar{\epsilon}_{33} \end{cases},\\ &\gamma_2 = \tfrac{1}{2}(\bar{\epsilon}_{11} - \bar{\epsilon}_{33})\,, \quad \gamma' = P_0\,, \quad \beta_1 = -\bar{e}_{31}\,, \quad \beta_2 = -\bar{e}_{33} + 2\bar{e}_{15} + \bar{e}_{31}\,, \quad \beta_3 = -2\bar{e}_{15}\,, \end{aligned} \tag{17}$$

where the overbar is used to distinguish between the values of material constants and the respective components of $\boldsymbol{\epsilon}$ and $\mathfrak{e}$. The elastic, piezoelectric, and dielectric moduli are obtained by

$$\mathbb{C}(\boldsymbol{P}) = \frac{\partial\boldsymbol{\sigma}}{\partial\boldsymbol{\varepsilon}} = \frac{\partial}{\partial\boldsymbol{\varepsilon}}\sum_{i=1/3}^{5}\frac{\partial H^{\text{bulk}}}{\partial I_i}\frac{\partial I_i}{\partial\boldsymbol{\varepsilon}} \tag{18}$$

$$= \lambda\mathbf{1}\otimes\mathbf{1} + 2\mu\mathbb{1} + (\omega^{n_1}\alpha_1 + \omega^{n_6}\alpha_6)\boldsymbol{\Xi} + 2\left(\omega^{n_2}\alpha_2 + \omega^{n_4}\alpha_4\right)\mathbf{m}\otimes\mathbf{m} \tag{19}$$

$$+ (\omega^{n_3}\alpha_3 + \omega^{n_5}\alpha_5)(\mathbf{1}\otimes\mathbf{m} + \mathbf{m}\otimes\mathbf{1})\,, \tag{20}$$

$$\mathfrak{e}(\boldsymbol{P}) = \frac{\partial\boldsymbol{D}}{\partial\boldsymbol{\varepsilon}} = \frac{\partial}{\partial\boldsymbol{\varepsilon}}\left(-\frac{\partial H^{\text{bulk}}}{\partial J_2}\frac{\partial J_2}{\partial\boldsymbol{E}} - \frac{\partial H^{\text{bulk}}}{\partial K_1}\frac{\partial K_1}{\partial\boldsymbol{E}}\right) = -\omega\beta_1\boldsymbol{p}\otimes\mathbf{1} - \beta_2\boldsymbol{p}\otimes\mathbf{m} - \omega\beta_3\hat{\mathfrak{e}}\,, \tag{21}$$

$$\boldsymbol{\epsilon}(\boldsymbol{P}) = \frac{\partial \boldsymbol{D}}{\partial \boldsymbol{E}} = -\frac{\partial}{\partial \boldsymbol{E}} \sum_{i=1}^{2} \frac{\partial H^{\text{bulk}}}{\partial J_i} \frac{\partial J_i}{\partial \boldsymbol{E}} = -2(\gamma_1 + \omega\gamma_3)\mathbf{1} - 2\gamma_2 \mathbf{m} \,, \tag{22}$$

where $\mathbb{1}_{ijkl} = \frac{1}{2}(\delta_{ik}\delta_{jl} + \delta_{il}\delta_{jk})$ and $\Xi_{ijkl} = p_i\delta_{jk}p_l + p_k\delta_{il}p_j$ and $\hat{e}_{kij} = \frac{1}{2}(\delta_{ik}p_j + \delta_{jk}p_i)$. For $BaTiO_3$ the following values are used: $n_1 = 1$, $n_2 = 0$, $n_3 = 0$, $n_4 = 1$, and $\alpha_5 = \alpha_6 = 0$.

The 2d version of the dimensionless non-convex potential $\tilde{\psi}(\boldsymbol{P})$ is assumed to take the form

$$\tilde{\psi}(\boldsymbol{P}) = \psi_0 + \frac{\psi_1}{P_0^2}\left(P_1^2 + P_2^2\right) + \frac{\psi_2}{P_0^4}\left(P_1^4 + P_2^4\right) + \frac{\psi_3}{P_0^4}P_1^2P_2^2 + \frac{\psi_4}{P_0^6}\left(P_1^6 + P_2^6\right) \,. \tag{23}$$

This energy is normalized by $\tilde{\psi}(0,0) = 1$, $\partial_{P_i}\tilde{\psi}(\pm P_0, 0) = 0$, and $\partial_{P_i}\tilde{\psi}(0, \pm P_0) = 0$.

2 Simulation results

The following simulation results were obtained with $BaTiO_3$ material data. A polycrystal consisting of five grains with randomly oriented crystal axes and initially random polarization is mechanically constrained ($\boldsymbol{u} = \mathbf{0}$ on the boundary) and electrically charge free. The figure shows the resulting domain structures for the equilibrated state. As the size of the polycrystal increases the domain structures become more complex.

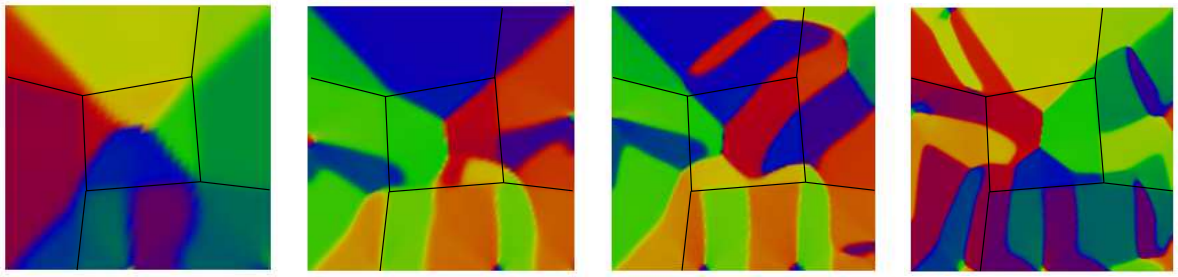

Figure 1: Resulting domain structures for load and charge free polycrystals subject to the b.c. $\boldsymbol{u} = \mathbf{0}$. The edge lengths of the quadratic simulation regions are from left to right: 24 nm, 48 nm, 72 nm, 96 nm.

REFERENCES

[1] D. Schrade, R. Müller, and D. Gross. On the physical interpretation of material parameters in phase field models, *Archive of Applied Mechanics*, 83: 1393–1413, 2013.

[2] M. E. Gurtin. Generalized Ginzburg-Landau and Cahn-Hilliard equations based on a microforce balance, *Physica D*, 92: 178–192, 1996.

[3] J. Schröder and D. Gross. Invariant formulation of the electromechanical enthalpy function of transversely isotropic piezoelectric materials, *Archive of Applied Mechanics*, 73: 533–552, 2004.

[4] B. Völker, P. Marton, C. Elsässer, and M. Kamlah. Multiscale modeling for ferroelectric materials: a transition from the atomic level to phase-field modeling, *Continuum Mech. Thermodyn.*, 23: 435–451, 2011.

[5] D. Schrade, R. Mueller, B. X. Xu, and D. Gross. Domain evolution in ferroelectric materials: A continuum phase field model and finite element implementation, *Comput. Meth. Appl. Mech. Eng.*, 196: 4365–4374, 2004.

QUANTITATIVE PIEZORESPONSE FORCE MICROSCOPY

Elisabeth Soergel

Institute of Physics, University of Bonn
Wegelerstrasse 8, 53115 Bonn, Germany
e-mail: soergel@uni-bonn.de

Abstract. *The impressive performance of piezoresponse force microscopy (PFM) in conjunction with its omnipresence – PFM is a standard operation mode in today's commercial scanning probe microscopy systems – has repeatedly led to an overestimation of its capabilities. PFM, although being decidedly a very powerful technique for investigating ferroelectrics, comes up with a series of difficulties regarding the interpretation of the, unfortunately almost always perfectly looking images. In my contribution, I will give a brief overview on the crucial conditions for reliable PFM-imaging, both from the side of the instrument and of the sample. This will lead me into the discussion of the reliability of PFM imaging and consequently the meaningfulness of a PFM image, may it be ever so beautiful. I will then in particular focus on quantitative PFM-imaging, or in other words: what can one quantitatively learn from a PFM image about the sample investigated. Here, special attention will be drawn on those parameters of ferroelectrics that can, at least to some extend, be answered by PFM, namely the arrangement of the domain pattern, the polarization direction of an individual domain, and the width of domain walls or the values of the coercive field, the piezoelectric coefficients, and the surface charge density. It will turn out, that although PFM-imaging does indeed allow to obtain at least the order of magnitude for some of the parameters listed above, it can not, in general, answer the ambitious expectations based on its otherwise unrivaled precision.*

1 Introduction

Ferroelectrics have recently attained increasing attention because of their widespread potential applications. The full potential of these materials can, however, only be exploited when locally controlling the direction of polarization. i.e. when structuring them with domains. Elaborate techniques for creating large area domain patterns in the mm-range with the individual domains being of the order of few microns only, have enabled real applications. Using periodically poled crystals for efficient frequency conversion using quasi phase matching is certainly the most prominent example.

Firstly, in view of potential applications, a technique for mapping the ferroelectric domain patterns with good lateral resolution was highly desired. Among the wealth of techniques that have been developed over the past fifty years [1], piezoresponse force microscopy (PFM) has taken over basically because of its ease-of-use: without any specific sample preparation, domain patterns can be non-destructively mapped with few 10 nm lateral resolution. This achievement whet the appetite for exploiting PFM imaging, and even more generally scanning force microscopy (SFM) imaging for gaining additional information of the materials properties. In this context, the very recent insights regarding domain wall conductivity, observed by conductive-SFM, is worth to be mentioned [2].

Nowadays, PFM has emerged from a domain-mapping tool towards an elaborated instrument for investigating various material properties of ferroelectrics and multiferroics. PFM has not only an excellent lateral resolution down to 10 nm, but also an unparalleled sensitivity, thus enabling to record domain patterns in materials with piezoelectric coefficients as small as 0.1 pm/V. Quite naturally, the demand for obtaining quantitative answers to a series of open questions of these materials have come to PFM. It has, however turned out, that obtaining quantitatively reliable results by PFM is much more challenging than initially assumed.

2 Experimental

PFM is based on the fact that ferroelectricity entails piezoelectricity, and a ferroelectric domain can thus be identified with a piezoelectric domain. The latter undergoes a shape-change upon the application of an electric field via the converse piezoelectric effect, and it is this very shape-change that is mapped by PFM. The application of the electric field is realized by the application of a small voltage to the tip of the SFM, and in order to increase the sensitivity, an alternating voltage is utilized and the accordingly periodic shape-changes of the sample are detected with the help of a lock-in amplifier. As mentioned above, piezoelectric responses as small as 1 pm can be mapped (with a typical value for the amplitude of the alternating voltage of 10 V). As for the lateral resolution, it is directly correlated to the tip radius, and values of ≈ 50 nm can be routinely achieved.

3 Results and Discussion[3]

At this moment I just want to exemplarily put attention on two points, namely the tininess of the PFM-signals detected and the rotational-symmetric field distribution from the tip, and discuss their consequences on quantitative PFM imaging.

Indeed, the impressive sensitivity of PFM directly calls for determining piezoelectric coefficients with high accuracy. This hope, however, must be given up for a series of reason that will be briefly outlined in the following. Firstly, as a consequence of the rotational symmetric field distribution of the tip, basically all piezoelectric coefficients within a single domain of the sample are excited, and the signal recorded is therefor a superposition of the different individual responses. One might now argue, that by applying a large-area top electrode to a single domain sample, thus realizing a capacitor-like field geometry inside, one could overcome this difficulty. This consideration being basically correct, one encounters however, a different issue, namely a system-inherent background which is superimposed to every PFM-signal. The origin of this frequency-dependent background lies in the mechanics of the setup itself which has a complicated frequency spectrum. Remind that the shape-changes of the sample are of the order of few pm only, which is small when compared to the size of an atom. Every excitation of the instrument's head, howsoever small, might therefor yield a contribution to the piezoresponse signal, thus falsifying any presumably quantitative result. Note that this effect plays only a significant role when investigating materials with small piezoelectric coefficients and thus of comparable magnitude than the contribution from the instrument's head. In case of large coefficients (as they are typical for ceramics), this background contribution is not significant. But, for these materials, the standard techniques can be used for determining the piezoelectric coefficients, and PFM is therefore out of place.

Coming back to the rotational-symmetric electric field distribution from the SFM-tip, there is another important consequence on PFM-imaging to be discussed. As mentioned above, the net movement of the sample surface underneath the tip will be the superposition of the response of

basically all individual piezoelectric coefficients with the appropriate component of the electric field. Consequently, this movement has not only an out-of-plane but also an in-plane component. The direction of the latter, however, is arbitrarily oriented with respect to the cantilever of the probe and will thus lead to both, torsion and buckling of the cantilever. Whereas the torsion signal can be separately read-out with the help of an additional lock-in amplifier, the buckling signal is necessarily recorded together with the out-of-plane signal. As a consequence, for deducing the net movement of the sample surface, one must physically rotate the sample by a known angle (preferably by $90°$) and record a second image of the very same area. Only by doing so, the net movement of the sample surface underneath the tip can be obtained. This can be accomplished by mounting the sample on top of a high-precision rotation stage, whereby the rotation axis must be perfectly aligned with the apex of the tip, a quite cumbersome task which must be repeated each time the probe is changed. Indeed, recording the torsion of the cantilever during sample rotation directly yields the information wanted, a maximum torsion signal of the cantilever indicating the direction of the sample's surface movement (perpendicular to the cantilever axis).

We upgraded our SFM setup with such a rotation stage, mounted on top of a high-precision x/y-translation stage. We could thereby not only perform the rotation-scans described above, but also record PFM images of the very same area at different angles. Such measurement are in particular interesting for non single-crystalline samples such as ferroelectric nanoparticle composites or ceramics since here, the possible directions of polarization vary within the sample.

Finally I would like to address a point which is the most crucial one for quantitative PFM imaging, and which is generally underestimated: the calibration of the microscope. Self-evidently, any attempt for quantitative PFM must start out from a reliable calibration of the experimental setup. Some difficulties can be easily outlined: i) the deflection and the torsion movement of the cantilever must be calibrated, ii) the smallest step-heights of z-calibration standards are some nanometer, which is by three orders of magnitude larger than what is the surface movement of a single-crystalline sample, iii) the calibration must include the total signal path, including also the lock-in amplifier (remind the frequency-dependent background). Indeed, an absolute calibration being obviously difficult, one can however compare data recorded with the signals obtained on a reliable sample. For the latter we use periodically poled lithium niobate. A big advantage is its being commercially available at reasonable price. Furthermore, one can orient the sample in such a way that no buckling contribution occurs, a mandatory requirement for calibrating the deflection of the cantilever. And finally, by using a PFM response for calibration, the total signal path is included. Hence, PFM signals of unknown samples can be quantitatively connected to the PFM signals obtained on lithium niobate. This however is a first step towards quantitatively reliable, although not absolute PFM data.

4 Conclusions

Fully quantitative PFM is still a challenge and might, at least for small signals as they are typical for a series of single crystals, generally not be possible. However the analysis of the possible cantilever movements, together with a detailed knowledge of the pitfalls surrounding PFM-imaging, allows at least to estimate the quantitative reliability of the PFM-data. Given the difficulties described above, it seems at present most appropriate to connect the values obtained to such a ones measured on reliable, intensively investigated, and thus well known samples. Although fully quantitative PFM-imaging continues to be an ambitious dream, a wealth of information on ferroelectrics can be obtained using the varieties of SFM, and thus also PFM among others.

REFERENCES

[1] E. Soergel. Visualization of Ferroelectric Domains in Bulk Single Crystals, *Applied Physics B*, 81: 729–752, 2005.

[2] J. Seidel et al. Conduction at Domain Walls in Oxide Multiferroics, *Natue Materials*, 8: 229–234, 2009.

[3] E. Soergel. Piezoresponse Force Microscopy, *Journal of Physics D: Applied Physics*, 44: 464003/1–17, 2011.

FINITE STRAIN MODELING, HOMOGENIZATION AND EFFECTIVE BEHAVIOR OF MAGNETORHEOLOGICAL ELASTOMERS

C. Spieler, M. Kästner, J. Brummund, and V. Ulbricht

Institute of Solid Mechanics, Chair of Nonlinear Solid Mechanics,
Faculty of Mechanical Science and Engineering, Technische Universität Dresden
George-Bähr-Straße 3c, 01069 Dresden, Germany
e-mail: {Christian.Spieler; Markus.Kaestner; Joerg.Brummund; Volker.Ulbricht}@tu-dresden.de

Abstract. *Magnetorheological elastomers (MRE) feature mechanical moduli that become enhanced by an applied external magnetic field as well as the ability to generate magnetically induced deformations and mechanical actuation stresses. Typically, MRE represent a two-component system, in which micron-sized magnetizable particles are embedded in a cross-linked polymer network. Because the effective coupled magneto-mechanical behavior is of special interest in technical applications, an in-depth understanding of the structure-property relations in MRE as well as suitable theories for computing the effective macroscopic material response are required. To this end, this contribution presents a homogenization approach for coupled magneto-mechanical problems.*

1 Continuum formulation of the problem

In this contribution we present the basic equations of the underlying magneto-mechanical field problem in a continuum based phenomenological way. The kinematic relations are specified in the context of finite deformations, because the MRE matrix material is an elastomer able to undergo large deformations. A detailed description of the field equations, the corresponding jump and boundary conditions (BC) and a constitutive model are presented in [1].

The continuum formulation of the stationary magnetic filed problem is given by the MAXWELL equations with respect to a current configuration. The field equations are completed by their corresponding jump conditions. According to [2] the magnetic field quantities in the reference configuration are given by an appropriate set of pull back operations. There are alternative ways to perform the link between a current the reference configuration. To solve the stationary magnetic filed problem it is convenient to use magnetic vector potential $\mathbf{A}$. Together with an additional condition, namely the COULOMB gauge, the vector potential is well-defined. The considered magnetizable particles possess a experimentally determined nonlinear magnetization curve with negligible hysteresis effects. An appropriate constitutive model is derived in [1].

The coupled mechanical boundary value problem (BVP) is governed by the balance of linear momentum and angular momentum, expressed in terms of the symmetric total stress tensor. We use a magnetic stress tensor which is microscopically motivated by de Groot and Suttorp in [3]. In accordance with the pull back operations of the magnetic field quantities, an alternative split of the total stress tensor is obtained out of the CLAUSIUS-DUHEM inequality, see also [2]. It results in the decomposition of the total stress tensor into two symmetric parts. However, this decomposition is not free of arbitrariness. The constitutive behavior of one stress contribution

is modeled by assuming a compressible form of a neo-HOOKEan material, which is a special case of the OGDEN material. The second part of the stress tensor is computed by the magnetic field variables.

The preceding explanations are used to model the coupled magneto-mechanical behavior and response of magnetoactive heterogeneous material structures, e.g., representative volume elements (RVE) of MRE.

2 Numerical modeling

The numerical solution of the underlying system of partial differential equations is accomplished by the extended finite element method (XFEM). The XFEM [4, 5] offers the possibility to use nonconforming computational meshes which do not have to be adapted to material interfaces. Hence, the meshes are independent of the location of discontinuities. This is advantageous if random particle arrangements are to be discretized. In addition, the implicit interface representation by level sets facilitates the automatic conversion of micrographs or computed tomography (CT) scans into a numerical model of the local material structure, which is one of the essential requirements for a multi-scale analysis. XFEM is therefore used to model the heterogeneous material structure of the problem mentioned above. The implemented higher-order XFEM formulation for the solution of stationary magnetic and coupled mechanical field problems in the context of small deformations is extensively described in [6, 7]. The vector potential $\mathbf{A}$ and the displacement vector $\mathbf{u}$ serve as the primary field variables. Some results of a convergence analysis of a bimaterial inclusion problem with a circular material interface are presented in Figure 1 and prove the ability of the implemented higher-order XFE [8].

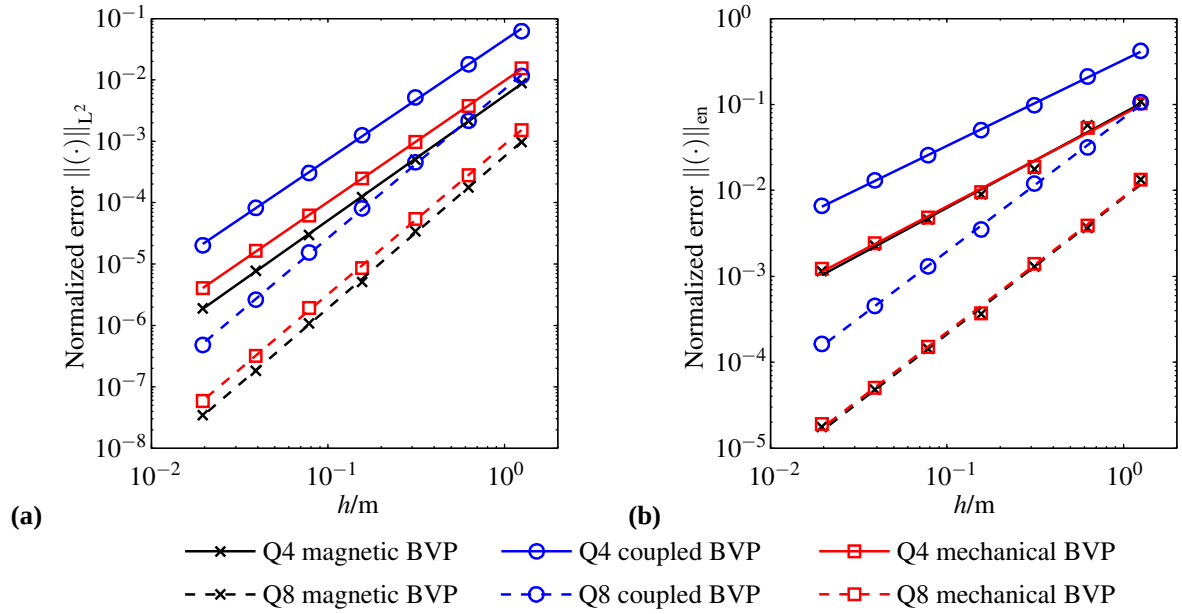

Figure 1: Convergence behavior of bilinear (Q4, solid lines) and biquadratic elements (Q8, dashed lines) for a magnetic, a coupled magneto-mechanical and a mechanical BVP depending on the characteristic element size h by means of normalized errors: **(a)** with respect to the L^2 norm and **(b)** in terms of the energy norm [8].

There are different approaches to treat the coupled field problem numerically. One possibility is a weak numerical coupling, also known as load vector, sequential, partitioned or staggered coupling. The implemented algorithm is schematically presented in Figure 2.

For simplicity and demonstration purposes, only problems homogeneous in the third direction will be considered. In this two-dimensional case $A_1 = A_2 = 0$ is an appropriate choice and the vector potential $\mathbf{A}$ contains only one nonzero component A_3. Since there are no gradients in the third direction, the COULOMB gauge is fulfilled and has not to be considered.
Furthermore a hybrid model of the isogeometric FEM and the isogemetric boundary element method is applicable to solve coupled magneto-mechanical field problems, as it is demonstrated in [9].

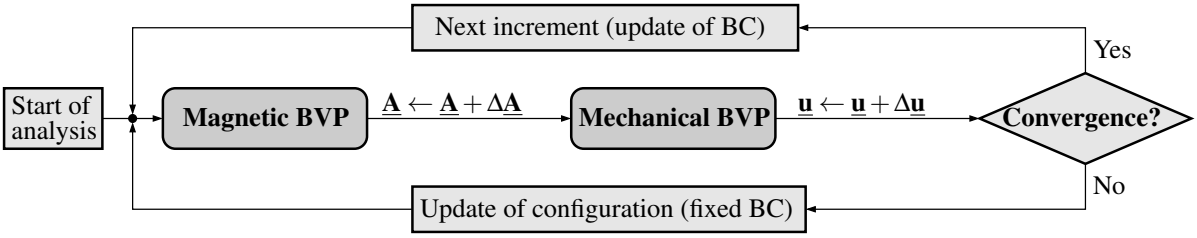

Figure 2: Implemented numerical coupling scheme with staggered solution strategy [1]

3 Homogenization and effective behavior

Based on the simulation of the magneto-mechanical interactions in a microscopic RVE, the effective coupled material behavior has been predicted using periodic boundary conditions for both the magnetic potential and the displacements in the context of small strains. Results obtained from computations are comparable to the analytic findings of Ponte Castañeda and Galipeau [10] and outlined in more detail in [7].

The following example which considers a two-dimensional arrangement of three circular inclusions (Figure 3 (a)) representing an idealized chain-like microstructure. The nonlinear magnetization behavior of the inclusions is modeled by a LANGEVIN function. While the magnetic induction $\bar{\mathbf{B}}$ is gradually increased, the macroscopic deformation was fixed, nevertheless allowing for periodic fluctuations. The effective response is computed in terms of macroscopic mechanical actuation stresses $\bar{\mathbf{t}}$, which result from the magneto-mechanical interactions in the case of fixed marcoscopic deformations. The results shown in Figure 3 (b) and (c) correspond to a load case where the macroscopic induction is applied at an angle of $45°$. In Figure 3 (b) the contour plots of the local magnetic induction with a sigmoidal deformed RVE are displayed. An essential aspect of the results is, that the macroscopic mechanical stress tensor in Figure 3 (c) is nonsymmetric with $\bar{t}_{12} < 0$ and $\bar{t}_{21} > 0$.

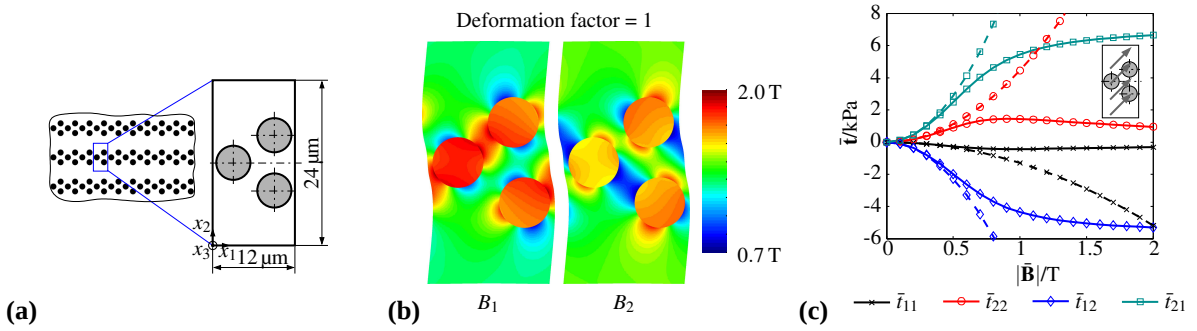

Figure 3: **(a)** Idealized RVE including three circular inclusions, **(b)** local magnetic induction and periodic displacement field and **(c)** macroscopic acutation stresses $\bar{\mathbf{t}}$ obtained from homogenization process [4].

In addition to the small strain results mentioned above, the present contribution will discuss the extension of the approach to account for large deformations and more complex random isotropic and anisotropic particle distributions. This includes the generalization of the continuum model, the implementation of an update-Lagrange XFEM for magneto-mechanical problems, the conversion of CT scans into XFEM models and the formulation of suitable material models as outlined in [1].

Acknowledgement

The present study is funded by the German Research Foundation (DFG), Priority Program (SPP) 1681, grant KA 3309/2-1. This support is gratefully acknowledged.

REFERENCES

[1] C. Spieler, P. Metsch, M. Kästner, and V. Ulbricht: Microscale modeling of magnetoactive composites undergoing large deformations, *Technische Mechanik*, accepted manuscript, 2014.

[2] A. C. Eringen and G. A. Maugin: *Electrodynamics of Continua I*. Springer, New York, 1990.

[3] S. R. de Groot and L. G. Suttorp: *Foundations of Electrodynamics*. North-Holland, Amsterdam, 1972.

[4] N. Moës, J. Dolbow, and T. Belytschko. A finite element method for crack growth without remeshing. *International Journal for Numerical Methods in Engineering*, 46(1): 131–150, 1999.

[5] T. Belytschko, N. Moës, S. Usui, and C. Parimi. Arbitrary discontinuities in finite elements. *International Journal for Numerical Methods in Engineering*, 50(4): 993–1013, 2001.

[6] M. Kästner, S. Müller, J. Goldmann, C. Spieler, J. Brummund, and V. Ulbricht. Higher-order extended FEM for weak discontinuities – level set representation, quadrature and application to magneto-mechanical problems, *International Journal for Numerical Methods in Engineering*, 93(13): 1403–1424, 2013.

[7] C. Spieler, M. Kästner, J. Goldmann, J. Brummund, and V. Ulbricht. XFEM modeling and homogenization of magnetoactive composites, *Acta Mechanica*, 224(11): 2453–2469, 2013.

[8] C. Spieler, M. Kästner, and V. Ulbricht. Analytic and numeric solution of a magneto-mechanical inclusion problem. *Archive of Applied Mechanics*, submitted manuscript, 2014.

[9] S. May, M. Kästner, S. Müller, and Volker Ulbricht. A hybrid IGAFEM/IGABEM formulation for two-dimensional stationary magnetic and magneto-mechanical field problems, *Computer Methods in Applied Mechanics and Engineering*, accepted manuscript, 2014.

[10] P. Ponte Castañeda and E. Galipeau. Homogenization-based constitutive models for magnetorheological elastomers at finite strain, *Journal of the Mechanics and Physics of Solids*, 59(2): 194–215, 2011.

ON THE STRAIN AND POLARISATION SATURATION OF PZT CERAMICS

S. Stark[1] **and H. Balke**[2]

[1] Institute of Solid Mechanics, Technische Universität Dresden
01062 Dresden, Germany
e-mail: Sebastian.Stark@tu-dresden.de

[2] Institute of Solid Mechanics, Technische Universität Dresden
01062 Dresden, Germany
e-mail: Herbert.Balke@tu-dresden.de

Abstract. *Polycrystalline ferroelectric materials like PZT ceramics show a distinct saturation behaviour. The present contribution describes a simple method to compute the theoretical multiaxial saturation states for remanent polarisation and strain. The approach is applied for the purely tetragonal crystal structure as well as for a mixture of the tetragonal and the rhombohedral phase. Thereby, material parameters are chosen, which are typical for PZT ceramics.*

1 Introduction

Any material model of polycrystalline PZT ceramics must adequately capture the bounds of remanent polarisation and strain. For macroscopic phenomenological material models, the boundary of attainable remanent states ("remanent boundary") is usually incorporated by energy barrier functions. One possibility to determine appropriate energy barrier functions is to choose certain ansatz functions and fit them to a previously micro-electromechanically computed data set, which describes the remanent boundary [1]. Efficient determination of this data set for different underlying crystal structures is the main focus here. With the saturation data in hand, fitting can be done based on (simultaneous) invariants of the remanent polarisation vector and the remanent strain tensor.

Initially, restriction is made to the theoretical (kinematic) saturation states. It is noted that, due to domain and grain interactions, it may be impossible to realise these saturation states experimentally. The modelling of such interactions is not discussed here, though it is an important issue. Nevertheless, it is outlined how the remanent states can be determined which are theoretically possible without causing any additional grain interactions with respect to the initial state being free of remanent polarisation and strain.

The present work is primarily an extension of a contribution of Landis et al. [1]. The main difference of our approach is that the determination of the saturation states does no longer require a complete micro-electromechanical material model. Rather, the problem of finding the limiting values of remanent strain and remanent polarisation is formulated in terms of a linear optimisation problem, which can be easily solved by standard algorithms (e.g. the Simplex method or the Interior point method). Therefore, it is a simple task to examine the saturation behaviour for different crystal structures and phase mixtures.

2 Computation of the remanent boundary

For the computation of the remanent saturation states, the polycrystalline aggregrate is described in a simplified way. A representative volume element composed of $n = 1 \dots N$ grains of equal volume is assumed. Each of the grains can contain domains of $\alpha = 1 \dots A$ domain variants (intrinsic dipole directions), where $v_{n,\alpha} \geq 0$ is the volume fraction of the variant α in the grain n. For the mixture of the tetragonal and the rhombohedral phase $A = 14$ and the variants $\alpha = 1 \dots 6$ belong to the tetragonal phase, while the variants $\alpha = 7 \dots 14$ belong to the rhombohedral phase. Furthermore, the following equalities for the volume fractions are assumed to hold for each grain

$$\sum_{\alpha=1}^{6} v_{n,\alpha} = v^{\mathrm{t}} \qquad \sum_{\alpha=7}^{14} v_{n,\alpha} = v^{\mathrm{r}} \qquad v^{\mathrm{t}} + v^{\mathrm{r}} = 1. \tag{1}$$

Here, v^{t} and v^{r} are the volume fractions of the tetragonal and the rhombohedral phase, respectively. The intrinsic dipole direction of a variant α in a grain n is described by the unit vector $\boldsymbol{n}^{n,\alpha}$. For the tetragonal phase, there are six dipole directions, which are oriented from the centre of a cube towards the faces. Similarly, for the rhombohedral phase, there are eight dipole directions, which are oriented form the centre of a cube towards the vertices. The spontaneous polarisation vector is defined by

$$\boldsymbol{P}^{n,\alpha} = P^{\mathrm{s},\alpha} \boldsymbol{n}^{n,\alpha}, \tag{2}$$

where $P^{\mathrm{s},\alpha}$ is the spontaneous polarisation magnitude of the respective variant. Similarly, the spontaneous strain tensor is

$$\boldsymbol{\varepsilon}^{n,\alpha} = 3\varepsilon^{\mathrm{s},\alpha}/2 \left(\boldsymbol{n}^{n,\alpha} \boldsymbol{n}^{n,\alpha} - 1/3 \boldsymbol{I} \right), \tag{3}$$

with $\varepsilon^{\mathrm{s},\alpha}$ being the spontaneous strain magnitude of the respective variant and $\boldsymbol{I}$ the unit tensor.

It is assumed that the macroscopic remanent polarisation vector $\boldsymbol{P}^{\mathrm{r}}$ and the macroscopic remanent strain tensor $\boldsymbol{\varepsilon}^{\mathrm{r}}$ are given by the volume weighted averages of the spontaneous quantities:

$$\boldsymbol{P}^{\mathrm{r}} = \frac{1}{N} \sum_{n=1}^{N} \sum_{\alpha=1}^{A} v_{n,\alpha} \boldsymbol{P}^{n,\alpha} \qquad \boldsymbol{\varepsilon}^{\mathrm{r}} = \frac{1}{N} \sum_{n=1}^{N} \sum_{\alpha=1}^{A} v_{n,\alpha} \boldsymbol{\varepsilon}^{n,\alpha}. \tag{4}$$

To obtain a single point of the saturation boundary, a remanent trial state $\boldsymbol{P}^{\mathrm{r,trial}}$, $\boldsymbol{\varepsilon}^{\mathrm{r,trial}}$ is chosen. Then, this trial state is scaled by the scalar factor $d \geq 0$ and the maximum value $d^{\max}$ is computed, for which the remanent state is kinematically admissible. The resulting remanent state $d^{\max} \boldsymbol{P}^{\mathrm{r,trial}}$, $d^{\max} \boldsymbol{\varepsilon}^{\mathrm{r,trial}}$ is a point on the saturation boundary. The computation of $d^{\max}$ is performed by solving the following linear optimisation problem:

$$\begin{gathered} d \rightarrow \text{Max.} \\ d\boldsymbol{P}^{\mathrm{r,trial}} - \boldsymbol{P}^{\mathrm{r}} = \boldsymbol{0} \qquad d\boldsymbol{\varepsilon}^{\mathrm{r,trial}} - \boldsymbol{\varepsilon}^{\mathrm{r}} = \boldsymbol{0}, \end{gathered} \tag{5}$$

where the independent variables are $d \geq 0$ and $v_{n,\alpha} \geq 0$. The latter are additionally subject to the equality constraints (1). The solution of this problem can be obtained by standard methods. For the results presented below, the interior point method provided by the commercial software Matlab is used. Note that it is also possible to obtain a point on the saturation boundary for a fixed admissible remanent polarisation state or a fixed admissible remanent strain state. This can be achieved by applying the scaling factor d only to $\boldsymbol{\varepsilon}^{\mathrm{r,trial}}$ or $\boldsymbol{P}^{\mathrm{r,trial}}$.

3 Computation of the interaction boundary

It is pointed out by Neumeister and Balke [2] that interactions between the grains have strong impact on the achievable remanent states. Moreover, it is shown in [3] that saturation behaviour occurs as soon as grain interactions begin to play a role. Hence, it is also useful to know the boundary of the remanent states, which can be attained without giving rise to grain interactions. As a first approximation, it is assumed here that grain interactions do not occur as long as all grains have the same remanent polarisation and strain. Consequently, the "interaction boundary" can be obtained by solving (5) individually for each grain n. If the resulting scaling factors are denoted by $d^{\max,n}$, a point on the interaction boundary is described by $d^{\max} = \mathrm{Min}_n(d^{\max,n})$.

4 Results

Saturation data has been obtained by the method described above for the whole space of remanent polarisation and remanent strain. Here, however, restriction is made to the presentation of some important results. All computations are performed with 64 grains. The orientations of these grains are optimised with respect to isotropy by a method, which will be presented elsewhere. The spontaneous polarisations and strains for the tetragonal and the rhombohedral phase of PZT are taken from [2] (tetragonal: $P^{\mathrm{s,t}} = 0.5\,\mathrm{C/m^2}$, $\varepsilon^{\mathrm{s,t}} = 1.91\%$; rhombohedral: $P^{\mathrm{s,rh}} = 0.5\,\mathrm{C/m^2}$, $\varepsilon^{\mathrm{s,rh}} = 0.55\%$). For the phase mixture, $v^{\mathrm{t}} = 0.2$ is assumed. Owing to isotropy and incompressibility, two principal remanent strains $\varepsilon^{\mathrm{r,I}}$, $\varepsilon^{\mathrm{r,II}}$ together with the remanent polarisation values $P^{\mathrm{r,I}}$, $P^{\mathrm{r,II}}$, $P^{\mathrm{r,III}}$ in the principal remanent strain directions are sufficient for the characterisation of the remanent state.

The data presented below is normalised as follows: For $v^{\mathrm{t}} = 1.0$, the maximum attainable remanent polarisation $P^{\mathrm{r,t,max}} = 0.414\,\mathrm{C/m^2} = 0.83P^{\mathrm{s,t}}$ and the maximum tensile remanent strain $\varepsilon^{\mathrm{r,t,max}} = 1.04\% = 0.55\varepsilon^{\mathrm{s,t}}$ are used for normalisation. Accordingly, all curves for $v^{\mathrm{t}} = 0.2$ are normalised by $P^{\mathrm{r,0.2,max}} = 0.429\,\mathrm{C/m^2}$ and $\varepsilon^{\mathrm{r,0.2,max}} = 0.49\%$. Normalised quantities are denoted by an overbar.

Figure 1 (a) shows the remanent strain boundary for $v^{\mathrm{t}} = 1.0$ and $v^{\mathrm{t}} = 0.2$ as well as the interaction boundary for $v^{\mathrm{t}} = 0.2$ in the case of zero remanent polarisation. Note that the interaction boundary reduces to a point at the origin for $v^{\mathrm{t}} = 1.0$. According to the maximum tensile remanent strains $\varepsilon^{\mathrm{r,t,max}}$ and $\varepsilon^{\mathrm{r,0.2,max}}$, the phase mixture allows theoretically for less remanent strain than the purely tetragonal crystal structure (the situation is different if grain interactions are taken into account as discussed in [2]). Nevertheless, it is evident from Figure 1 (a) that the shape of the remanent strain boundary for $v^{\mathrm{t}} = 1.0$ and $v^{\mathrm{t}} = 0.2$ is almost identical. Thus, if a suitable (artificial) spontaneous strain is chosen for the tetragonal phase, the remanent strain boundary of the phase mixture can be described with good approximation by a purely tetragonal model. The curve for the interaction boundary for $v^{\mathrm{t}} = 0.2$ shows that a substantial portion of the theoretically possible remanent strain can be attained without grain interactions for the phase mixture. In contrast, for $v^{\mathrm{t}} = 1.0$, no remanent strain is possible without grain interactions.

Figure 1 (b) and Figure 1 (c) show the achievable remanent polarisation $P^{\mathrm{r,I}}$ in dependence of the remanent strain $\varepsilon^{\mathrm{r,I}}$ in the case of transversally isotropic extension ($\varepsilon^{\mathrm{r,II}} = \varepsilon^{\mathrm{r,III}} = -\varepsilon^{\mathrm{r,I}}/2$) and pure shear ($\varepsilon^{\mathrm{r,II}} = -\varepsilon^{\mathrm{r,I}}$; $\varepsilon^{\mathrm{r,III}} = 0$), respectively. Again, the curves for the remanent polarisation boundary for $v^{\mathrm{t}} = 1.0$ and $v^{\mathrm{t}} = 0.2$ are brought into reasonable agreement by the normalisation, though detail differences are present. It is noted that there are portions of the (normalised) remanent boundary, where the deviations between the purely tetragonal case and the phase mixture are much larger than in the results shown. However, these portions correspond to complicated remanent states, and it is not yet clear whether they are important for

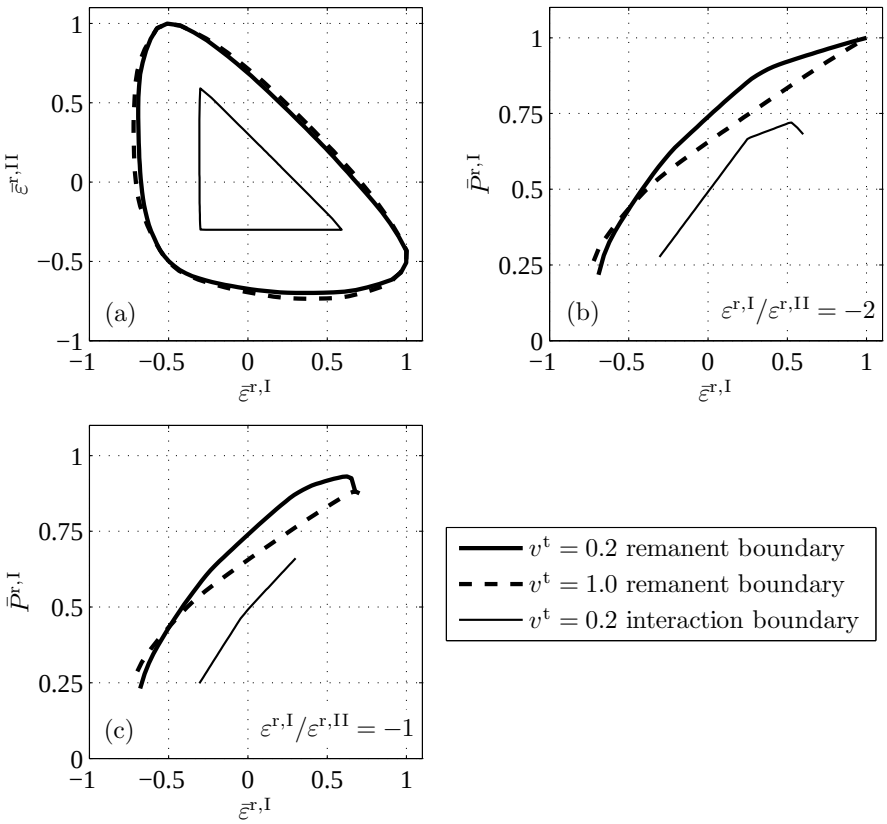

Figure 1: Results for the boundary of remanent states and the interaction boundary

practical examples. As in Figure 1 (a), the interaction boundary in Figure 1 (b) and (c) indicates that substantial parts of the remanent polarisation and strain can be realised without significant grain interactions for the phase mixture.

5 Conclusions

From the results presented above the following main conclusions are drawn: 1) For a coarse approximation, it is valid to describe the saturation behaviour of the phase mixture based on a tetragonal model with artificially chosen spontaneous polarisations and strains and, 2) for the phase mixture, a significant part of the theoretically accessible space of remanent states can be attained without giving rise to additional grain interactions.

REFERENCES

[1] C. M. Landis, J. W. Wang and J. Sheng. Micro-electromechanical Determination of the Possible Remanent Strain and Polarization States in Polycrystalline Ferroelectrics and the Implications for Phenomenological Constitutive Theories, *Journal of Intelligent Material Systems and Structures*, 15: 513–525, 2004.

[2] P. Neumeister and H. Balke. Micromechanical modelling of the remanent properties of morphotropic PZT, *Journal of the Mechanics and Physics of Solids*, 59: 1794–1807, 2011.

[3] P. Neumeister. Mikromechanische Modellierung morphotroper PZT-Keramiken, *Doktorarbeit*, TU Dresden, 2011.

APPLICATION OF ROBUST NUMERICAL DERIVATIVE APPROXIMATIONS TO FINITE STRAIN CONSTITUTIVE MODELS

Masato Tanaka[1], **Masaki Fujikawa**[2], **Daniel Balzani**[3], **and Jörg Schröder**[3]

[1] Toyota Central R&D Laboratories, Inc.
41-1 Yokomichi, Nagakute, Aichi, 480-1192, Japan
e-mail: tanamasa@mosk.tytlabs.co.jp

[2] Faculty of Engineering Department of Mechanical Systems, University of the Ryukyus
1 Senbaru, Nishihara, Okinawa, 903-0213, Japan
e-mail: fujikawa@tec.u-ryukyu.ac.jp

[3] Institute of Mechanics, Faculty of Engineering, Department of Civil Engineering, University Duisburg-Essen
Universitätsstr. 15, 45117 Essen, Germany
e-mail: daniel.balzani@uni-due.de, j.schroeder@uni-due.de

Abstract. *In this work we propose numerical differentiation schemes for an implementation of finite strain material models. The approaches for the numerical differentiation are comparatively analyzed, including the finite difference (FD) scheme and the complex-step derivative approximation (CSDA). While the FD suffers from roundoff errors and is quite sensitive to the choice of perturbation values, the CSDA achieves monotonic improvement with decreasing perturbations. Thereby, the numerical derivatives by the CSDA are almost identical to the analytic ones when choosing perturbations close to machine precision. We compare the results of the numerical approaches using a polyconvex anisotropic hyperelastic material model .*

1 Introduction

Many material models lead to complicated formulations of the exact expressions for their constitutive equations and they might result in tedious and error-prone tensor calculations. In those cases numerical differentiation schemes can provide an alternative in particular for scientific development purposes. The often-used classical finite difference (FD) schemes are highly sensitive with respect to perturbation values and only applicable for a small range of values. To overcome this difficulty of the FD schemes, Lyness [1] devised the complex-step derivative approximation (CSDA) scheme. In this work, we focus on the use of the CSDA for the numerical approximation of the constitutive equations and robust numerical approaches that can be implemented within FE-software are thoroughly investigated.

2 Scheme for numerical derivatives

The CSDA is a powerful technique to avoid the sensitive and unstable choice of the perturbation parameter h which is often observed in the FD scheme. The derivation of the CSDA is accomplished from Taylor series expansion using an imaginary perturbation ih with $i^2 = -1$, i.e.

$$f(x+ih) = f(x) + ihf'(x) - \frac{h^2}{2!}f''(x) - i\frac{h^3}{3!}f'''(x) + \cdots , \tag{1}$$

wherein i denotes an imaginary unit. Taking an imaginary part of both sides of (1) and neglecting higher-order terms yields the CSDA scheme as

$$f'(x) \simeq \frac{\Im[f(x+ih)]}{h}, \tag{2}$$

wherein $\Im$ denotes an operation of taking the imaginary part of the complex function. Note that since the expression (2) does not have any subtraction operation, the roundoff errors never arise.

3 Application to constitutive relations between stress and strain tensors

Spatial setting:

The spatial tangent modulus $\mathbb{c}$ in $\overset{\circ}{\boldsymbol{\tau}} = \mathbb{c} : \boldsymbol{d}$ with the objective Oldroyd rate of the Kirchhoff stress tensor $\overset{\circ}{\boldsymbol{\tau}}$ and the symmetric part of the spatial velocity gradient $\boldsymbol{d}$ can be derived by using the Doyle-Ericksen formula as

$$(\mathbb{c})^{ijkl} = 2\frac{\partial \tau^{ij}(\boldsymbol{F}, \boldsymbol{g})}{\partial g_{kl}}, \tag{3}$$

wherein, $\boldsymbol{F}$ is the deformation gradient tensor and $\boldsymbol{g}$ denotes the metric tensor in the current configuration. With the contravariant base vector in the current configuration $\boldsymbol{g}^{\mathrm{k}}$ the approximation of $(\mathbb{c})^{ijkl}$ using the CSDA scheme is written by

$$(\mathbb{c})^{ijkl} \simeq \lim_{h\to 0} 2\frac{\Im\left[\tau^{ij}\left(\boldsymbol{F}, \boldsymbol{g} + ih\overset{*}{\boldsymbol{g}}{}^{(\mathrm{k})(\mathrm{l})}\right)\right]}{h} \quad \text{with} \quad \overset{*}{\boldsymbol{g}}{}^{(\mathrm{k})(\mathrm{l})} = \frac{1}{2}(\boldsymbol{g}^{(\mathrm{k})} \otimes \boldsymbol{g}^{(\mathrm{l})} + \boldsymbol{g}^{(\mathrm{l})} \otimes \boldsymbol{g}^{(\mathrm{k})}). \tag{4}$$

Nominal setting:

The nominal tangent modulus $\mathbb{A}$ in $\dot{\boldsymbol{P}} = \mathbb{A} : \dot{\boldsymbol{F}}$ with the material time derivative of the first Piola-Kirchhoff stress tensor $\dot{\boldsymbol{P}}$ and deformation gradient tensor $\dot{\boldsymbol{F}}$ can be derived as

$$(\mathbb{A})_i{}^J{}_k{}^L = \frac{\partial P_i{}^J(\boldsymbol{F})}{\partial F^k{}_L}. \tag{5}$$

With the covariant base vector in the current configuration $\boldsymbol{g}_{\mathrm{k}}$ and the contravariant base vector in the reference configuration $\boldsymbol{G}^{\mathrm{L}}$ the approximation of $(\mathbb{A})_i{}^J{}_k{}^L$ using the CSDA scheme is written by

$$(\mathbb{A})_i{}^J{}_k{}^L \simeq \lim_{h\to 0} \frac{\Im\left[P_i{}^J\left(\boldsymbol{F} + ih\overset{*}{\boldsymbol{F}}_{(\mathrm{k})}{}^{(\mathrm{L})}\right)\right]}{h} \quad \text{with} \quad \overset{*}{\boldsymbol{F}}_{(\mathrm{k})}{}^{(\mathrm{L})} = \boldsymbol{g}_{(\mathrm{k})} \otimes \boldsymbol{G}^{(\mathrm{L})}. \tag{6}$$

4 Numerical examples

Model description:

The strain energy density function for the polyconvex anisotropic hyperelastic model reads

$$\psi = \alpha_1\left(\frac{I_1}{I_3^{1/3}} - 3\right) + \epsilon_1\left(I_3^{\epsilon_2} + \frac{1}{I_3^{\epsilon_2}} - 2\right) + \sum_{a=1}^{n_f}\left[\beta_1\left\langle I_1 J_4^{(a)} - J_5^{(a)} - 2\right\rangle^{\beta_2}\right], \tag{7}$$

wherein $\langle\bullet\rangle$ denotes the Macaulay bracket, n_f is a number of fiber families, $\alpha_1 > 0, \beta_1, \beta_2, \epsilon_1 > 0, \epsilon_2 > 0$ are material parameters, I_1, I_2, I_3 are invariants of the right Cauchy-Green deformation

tensor $\boldsymbol{C}$ and the mixed invariants are defined as $J_4^{(a)} = \text{tr}\left[\boldsymbol{C}\boldsymbol{M}^{(a)}\right]$ and $J_5^{(a)} = \text{tr}\left[\boldsymbol{C}^2\boldsymbol{M}^{(a)}\right]$, where $\boldsymbol{M}^{(a)} = \boldsymbol{a}^{(a)} \otimes \boldsymbol{a}^{(a)}$ is the structural tensor governed by the preferred direction $\boldsymbol{a}^{(a)}$.

Convergence behavior in a Cook-type cantilever beam:

To assess the performance of the approximated spatial tangent moduli (4), we analyze a Cook-type cantilever beam. We choose the set of material parameters as $\alpha_1 = 6.0$, $\beta_1 = 100.0$, $\beta_2 = 2.5$, $\epsilon_1 = 100.0$, $\epsilon_2 = 5.0$ with α_1, ϵ_1 and β_1 in unit of stress. The preferred direction is assigned as $n_f = 1$ and $\boldsymbol{a}^{(1)} = 1/\sqrt{3}\begin{pmatrix}1 & 1 & 1\end{pmatrix}^T$. The shear load p is successively increased until the maximum shear load $p = 5.0$ is reached, cf. Figure 1(a). Figure 1 (b-c) show the deformed configurations with the resulting stress distribution σ_{xx}. Figure 1 (d) shows the comparison of CPU time, and Table 1 reports the sensitivity of the rate of convergence. We conclude that the resulting tangent moduli with FD scheme are not accurate enough and the Newton-Raphson method loses its characteristic quadratic convergence. In contrast to that, the CSDA scheme shows robust and highly accurate performance with sufficiently small value of h. Furthermore, the CSDA is not expensive for finer meshes since the computing time associated with the calculation of the stiffness matrices becomes less significant than the time for solving the system of equations.

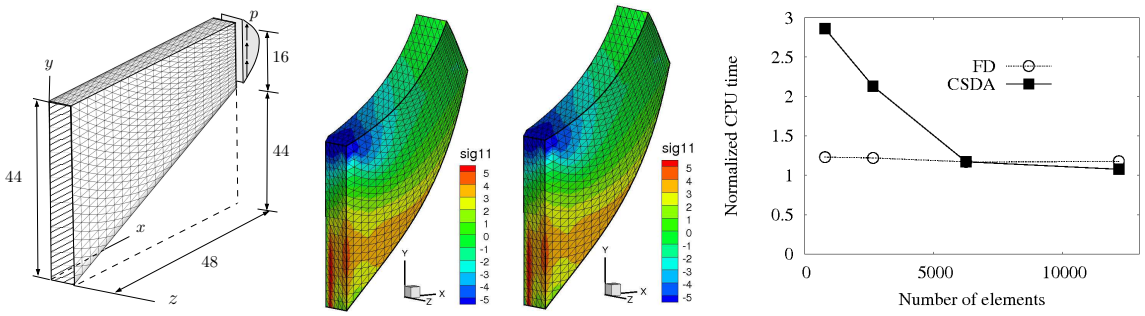

(a) Boundary value problem (b) Analytical (c) CSDA (d) CPU time

Figure 1: The deformed configurations of analytical, FD, CSDA scheme for Cook-type problem and comparison of CPU time for each scheme.

Table 1: Euclidean norm of residual of Cook-type problem with analytical, FD, CSDA computation of tangent moduli tensor.

Analytical	FD			CSDA		
	$h = 10^{-8}$	$h = 10^{-9}$	$h = 10^{-10}$	$h = 10^{-8}$	$h = 10^{-9}$	$h = 10^{-30}$
1.0901×10^{-2}	Failed	1.0901×10^{-2}	Failed	1.0901×10^{-2}	1.0901×10^{-2}	1.0901×10^{-2}
9.3049×10^{-2}	–	3.4733×10^{-2}	–	$4.0149 \times 10^{+1}$	3.8953×10^{-2}	9.3049×10^{-2}
1.0079×10^{-3}	–	3.8899×10^{-2}	–	$8.7424 \times 10^{+0}$	4.0374×10^{-2}	1.0079×10^{-3}
7.1403×10^{-7}	–	4.1916×10^{-4}	–	$8.8939 \times 10^{+0}$	8.1633×10^{-5}	7.1264×10^{-7}
5.0581×10^{-8}	–	1.0431×10^{-5}	–	4.1320×10^{-1}	5.7772×10^{-8}	5.0173×10^{-8}
–	–	5.8564×10^{-7}	–	8.2395×10^{-2}	4.9528×10^{-8}	–
–	–	7.1674×10^{-8}	–	1.4558×10^{-4}	–	–
–	–	5.1623×10^{-8}	–	1.5088×10^{-7}	–	–
–	–	5.0849×10^{-8}	–	5.2052×10^{-8}	–	–

Application to localization analysis:

The investigation of material stability of a constitutive model requires the analysis of the positive definiteness of the acoustic tensor which in turn depends on the nominal tangent moduli $\mathbb{A}$, see [2][3]. Here, we consider the polyconvex anisotropic model (7) with two fiber families ($n_\text{f} = 2$). The set of material parameters is $\alpha_1 = 1.0$, $\epsilon_1 = 1.0$, $\epsilon_2 = 0.1$, $\beta_1 = 1.0$ and $\beta_2 =$

3.0. The preferred directions in the reference configuration are $\boldsymbol{a}^{(1)} = 1/\sqrt{2}\begin{pmatrix}1 & 1 & 0\end{pmatrix}^T$ and $\boldsymbol{a}^{(2)} = 1/\sqrt{2}\begin{pmatrix}1 & -1 & 0\end{pmatrix}^T$. We compute the localization parameter q (see the definition and details in [2]) for a specific deformation gradient ($F^1{}_1 = 1.1$, $F^1{}_2 = 2.$, $F^2{}_2 = F^3{}_3 = 0.9535$, $F^1{}_3 = F^2{}_1 = F^2{}_3 = F^3{}_1 = F^3{}_2 = 0.$). The results of the localization analysis according to the numerical approximations of the tangent moduli are shown in Fig. 2. For the CSDA scheme all of the considered perturbation values lead to the same distribution of q showing only positive values. In contrast to that, the localization analysis based on the FD scheme is rather sensitive regarding the choice of the perturbation value. This means that by using the wrong perturbation value (which is user-defined and therefore not a priori known) the FD scheme may detect material instabilities where there are none. The CSDA scheme instead can efficiently and reliably be used when choosing sufficiently small perturbation values.

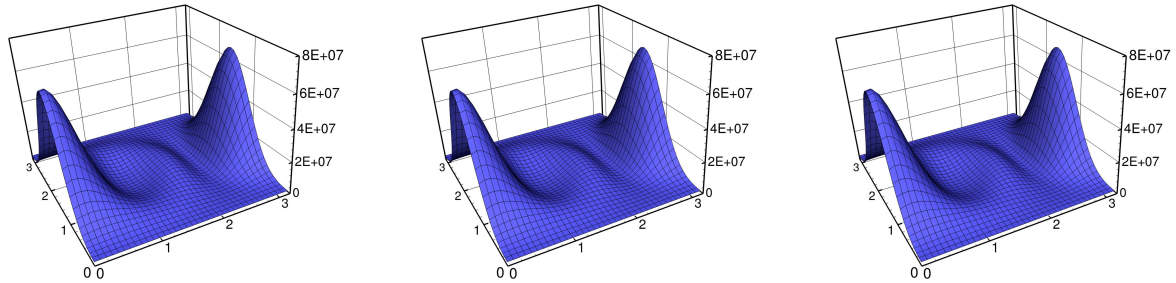

(a) CSDA, $h = 10^{-12}$ (b) CSDA, $h = 10^{-13}$ (c) CSDA, $h = 10^{-14}$

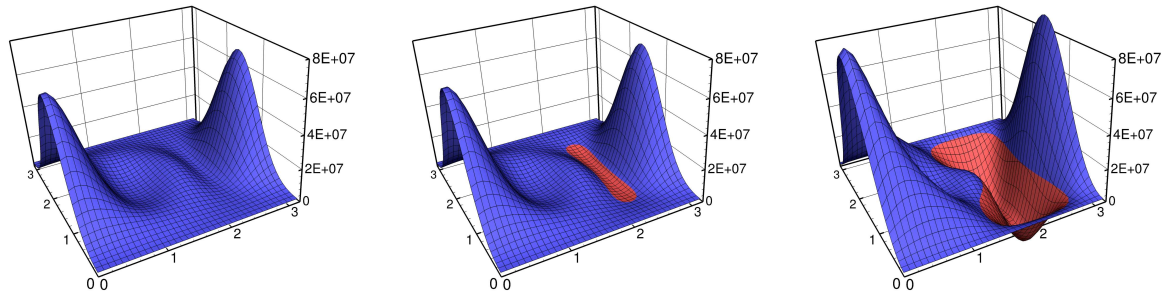

(d) FD, $h = 10^{-12}$ (e) FD, $h = 10^{-13}$ (f) FD, $h = 10^{-14}$

Figure 2: Distributions of localization measure q based on numerical approximations of the tangent moduli. Note that blue and red colors indicate positive and negative values, respectively.

REFERENCES

[1] J. N. Lyness,. Differentiation formulas for analytic functions, *Math. Comput.*, 352–362, 1968.

[2] J. Schröder, P. Neff and D. Balzani. A variational approach for materially stable anisotropic hyperelasticity, *Int. J. Solids Struct.*, 42(15):4352–4371, 2005.

[3] M. Tanaka, M. Fujikawa, D. Balzani and J. Schröder. Robust numerical calculation of tangent moduli at finite strains based on complex-step derivative approximation and its application to localization analysis, *Comput. Methods Appl. Mech. Engrg.*, 269:454–470, 2014.

ON THE PREPARATION, CHARACTERISATION, MODELLING AND SIMULATION OF MAGNETO-SENSITIVE ELASTOMERS

Bastian Walter[1], **Prashant Saxena**[1], **Jean-Paul Pelteret**[1], **Joachim Kaschta**[2]
Dirk W. Schubert[2] **and Paul Steinmann**[1]

[1] Chair of Applied Mechanics, Department of Mechanical Engineering, University of Erlangen-Nuremberg
Egerlandstrasse 5, Erlangen, Germany
e-mail: bastian.walter@ltm.uni-erlangen.de, prashant.saxena@ltm.uni-erlangen.de,
jean-paul.pelteret@ltm.uni-erlangen.de, paul.steinmann@ltm.uni-erlangen.de

[2] Institute of Polymer Materials, Department of Materials Science and Engineering,
University of Erlangen-Nuremberg
Martensstrasse 7, Erlangen, Germany
e-mail: joachim.kaschta@fau.de, dirk.schubert@ww.uni-erlangen.de

Abstract. *Magneto-sensitive elastomers are smart materials that change their mechanical properties under the influence of a magnetic field. The method of preparation and characterisation of MSEs by rheological experiments and imaging techniques are presented. Data, obtained through rheological experiments, is used to validate a material model that couples the theories of viscoelasticity and magnetoelasticity. Using model parameters received by fitting the relaxation tests and shear experiments, the behaviour of MSEs in dynamic mechanical experiments under various experimental conditions can be successfully predicted. The material model is validated for small deformations and magnetic fields up to 0.3 T and has been implemented within an in-house finite element code.*

1 Introduction

Magneto-**S**ensitive (**MS**) or **M**agneto-**R**heological (**MR**) **E**lastomers belong to the class of smart materials that possess the ability to change their shape and/or material properties under the influence of magnetic fields. In general, MSEs are composed of a non-magnetic, rubber-like polymeric matrix (e.g. natural or silicone rubber) filled with magnetically permeable particles (e.g. carbonyl iron powder) typically in a range of one to a few tens of micrometers in diameter. Anisotropic MSEs can be prepared by curing the mixed raw materials in the presence of a magnetic field. The originally randomly distributed particles build up chain-like particle structures oriented in field direction.

On the application of an external magnetic field to MSEs, magnetic dipoles are induced in the magnetisable particles leading to significant particle-particle interactions associated with particle movements. A rapid, continuous and reversible change in the shape and/or material properties are achieved. MSEs are therefore of great interest for application in novel smart sensors, actuators, and adaptive damping systems [1, 2].

The characteristic response of MSEs is affected by the morphology of the composite, the properties of the polymeric matrix and particles (type and composition, aspect ratio, size, and size-distribution), and volume filler fraction (see [2] and several references therein). Addition-

ally, the chemistry of the particle surface and other ingredients (e.g. reinforcing fillers and plasticisers) present in the rubber may have an effect on the resulting MSEs as well [3].

Mathematical modelling of the coupling of electromagnetic fields in deformable continua has been studied extensively in the past (see [4, 5] and several references therein). Based on these works, Dorfmann and Ogden [6] have developed a formulation based on 'total energy' to model soft elastomeric MREs.

From an engineering point of view, the numerical simulation of MSEs under operating conditions provides a powerful tool in the design process. To this end, it is necessary to attain simulation results using material models that best represent the complex composite material behaviour. To achieve this requirement, several steps are vital. Firstly, it is necessary to understand the underlying morphology of the MSE and its particle structure. Secondly, the material response related to the change of the internal structure (i.e. particle network) and particle-particle interactions under different mechanical and magnetic loading conditions has to be characterised. Finally, material models that couple electromagnetic and mechanical phenomena in deformable viscoelastic solids must be developed and implemented within analytical models and finite element codes.

This work is focussed on all these topics. Some selected results are shown below.

2 Material preparation and experimental methodology

The results presented here refer to model systems based on liquid silicone rubber (ELASTOSIL® LR3003/03, Wacker) filled with carbonyl iron powder (type SQ, $d_{50} \approx 5\ \mu m$, BASF). Well defined MSEs are prepared, using a SpeedMixer™ (DAC 150 SP, Hauschild), a desiccator equipped with a vacuum pump (RV3, Edwards) and a two-part custom made casting mould. The MSEs are cured in an oven (VT 6060 M, Thermo Fisher Scientific) at 120°C for 16 hours. Lastly, specimens of 20 mm diameter are punched out of the 50 x 50 x 1.0 mm^3 cast sheet.

SEM and μ-CT imaging techniques are used to gain insight into the homogeneity and structure of the composites. The particles are also characterised by laser diffraction. Oscillatory, quasi-static and transient shear experiments were performed by means of a rheometer equipped with a magneto-rheological device (MCR 502, Anton Paar). The data obtained was used for verification and validation of the material model and simulation.

3 Numerical modelling and simulation

Coupling the theory of magnetoelasticity [6] with that of nonlinear viscoelasticity (see [7] for example), the following formulation for modelling rate-dependent dissipation effects in MREs is used [8].

Consider a finitely deformed magnetoelastic solid on which a magnetic induction $\mathbb{B}$ is applied and the deformation is given by the deformation gradient tensor $\mathbf{F}$. In order to model dissipation, we consider a decomposition of $\mathbf{F}$ into equilibrium and non-equilibrium parts as

$$\mathbf{F} = \mathbf{F}_e \cdot \mathbf{F}_v. \tag{1}$$

The total energy Ω is further decomposed into 'equilibrium' and 'non-equilibrium' parts such that $\Omega = \Omega_e(\mathbf{C}, \mathbb{B}) + \Omega_v(\mathbf{C}, \mathbf{C}_v)$, where we define $\mathbf{C} = \mathbf{F}^t \cdot \mathbf{F}$ and $\mathbf{C}_v = \mathbf{F}_v^t \cdot \mathbf{F}_v$. The second law of thermodynamics leads to the constitutive equations for the second Piola–Kirchhoff stress $\mathbf{S}$, the magnetic field $\mathbb{H}$ and dissipation condition for $\mathbf{C}_v$ as

$$\mathbf{S} = 2\frac{\partial \Omega}{\partial \mathbf{C}}, \quad \mathbb{H} = \frac{\partial \Omega}{\partial \mathbb{B}}, \qquad \frac{\partial \Omega_v}{\partial \mathbf{C}_v} : \frac{d\mathbf{C}_v}{dt} \leq 0. \tag{2}$$

The model is completely defined once we specify the function form for Ω_e, Ω_v as well as the law for evolution of $\mathbf{C}_v$. The development of the total energy function and evolution law are closely linked to the phenomena observed in the experimental data.

This non-linear, rate-dependent phenomenological model has been implemented within an in-house finite element code developed using a modern open-source FEM library [9]. Developed from variational principals [10], a fully-coupled finite-strain formulation was used in the simulation of the experimental conditions. The incompressible nature of the material matrix was accounted for using a mixed approach [11].

4 Material model and simulation validation

The experimental conditions have been simulated using both analytical models and finite element analysis. The material parameters in the equilibrium and non-equilibrium part of the total energy function as well as the evolution parameters are obtained by fitting the experimental data. Figure 1 shows an example of the experimental data (average of at least 5 measurements at 25°C) obtained for a MSE filled with 15 vol.-% carbonyl iron powder. Such data was used to fit the parameters of the material model.

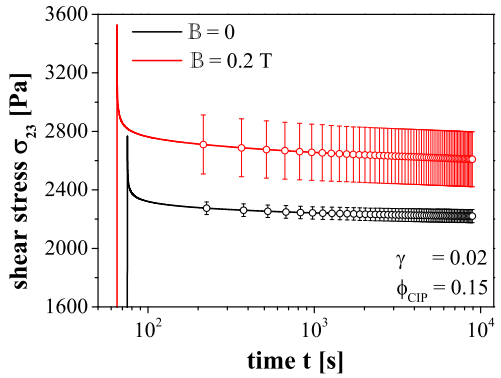

a) Relaxation test ($\gamma = 0.02$) [12]

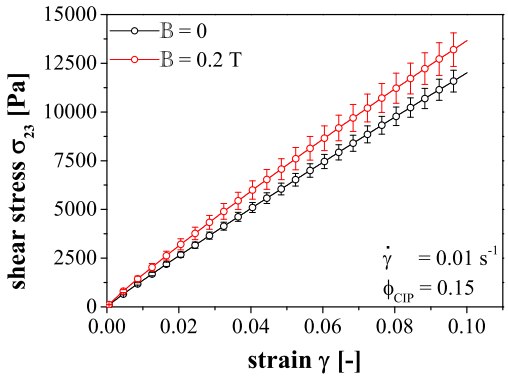

b) Shear experiment ($\dot{\gamma} = 0.01 s^{-1}$) [12]

Figure 1: Example of experimental results obtained with and without magnetic loading ($\phi = 15$ vol.-%).

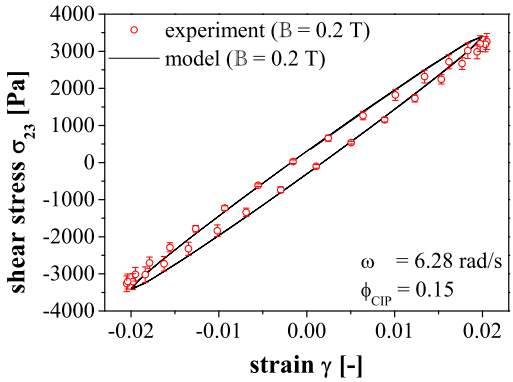

a) Lissajous plot ($\omega = 6.28$ rad/s) [12]

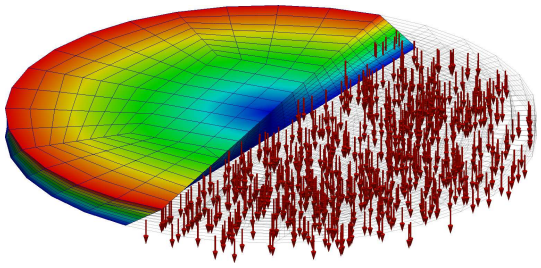

b) Representative FEM simulation

Figure 2: Examples of modelling and simulation results ($\phi = 15$ vol.-%, T=25°C).

The viscoelastic behaviour of MSEs in dynamic mechanical experiments under varying experimental conditions can be successfully predicted for small deformations and low magnetic

fields. Within the scope of the measurement accuracy, the material model and experiment results correlate reasonably well. This is demonstrated in the predicted dynamic stress-strain curves (Lissajous plot) in Figure 2 a). Figure 2 b) illustrates the FEM simulation of a test specimen in the rheometer. The sample is placed in torsion and the magnetic load, shown by the arrows, applied in the axial direction.

ACKNOWLEDGEMENTS

This work is supported by the ERC advanced investigator grant MOCOPOLY. The authors also thank BASF and Wacker Chemie for providing the raw materials free of charge.

REFERENCES

[1] M. R. Jolly, J. D. Carlson, and B. C. Muñoz. A model of the behaviour of magnetorheological materials, *Smart Materials and Structures*, 5(5): 607–614, 1996.

[2] A. Boczkowska and S. Awietjan. Microstructure and properties of magnetorheological elastomers. In A. Boczkowska, editor, *Advanced Elastomers - Technology, Properties and Applications*, 147–180, InTech, 2012.

[3] L. Chen, X. L. Gong, and W. H. Li. Effect of carbon black on the mechanical performances of magnetorheological elastomers, *Polymer Testing*, 27(3): 340–345, 2008.

[4] Y. H. Pao. Electromagnetic forces in deformable continua. In S. Nemat-Nassar, editor, *Mechanics Today*, vol. 4, 209–305, Oxford University Press, 1978.

[5] A. C. Eringen and G. A. Maugin. *Electrodynamics of Continua*. Springer-Verlag, New York, 1980.

[6] A. Dorfmann and R. W. Ogden. Nonlinear magnetoelastic deformations, *Quarterly Journal of Mechanics and Applied Mathematics*, 57(7): 599–622, 2004.

[7] S. Reese and S. Govindjee. A theory of finite viscoelasticty and numerical aspects, *International Journal of Solids and Structures*, 35(26-27): 3455–3482, 1998.

[8] P. Saxena, M. Hossain and P. Steinmann. A theory of finite deformation magneto-viscoelasticity, *International Journal of Solids and Structures*, 50 (24): 3886–3897, 2013.

[9] W. Bangerth, R. Hartmann and G. Kanschat. deal.II A general-purpose object-orientated finite element library, ACM Transactions on Mathematical Software, 33 (4): 24/1–24/27, 2007.

[10] D. K. Vu and P. Steinmann. Nonlinear Electro- and Magneto-Elastostatics: Material and Spatial Settings, *International Journal of Solids and Structures*, 44 (24): 7891–7905, 2007

[11] J. Simo and R. Taylor. Quasi-incompressible finite elasticity in principal stretches. Continuum basis and numerical algorithms, *Computer Methods in Applied Mechanics and Engineering*, 85 (3): 273–310, 1991.

[12] B. Walter, P. Saxena, J. Kaschta, D. W. Schubert and P. Steinmann. Characterisation of magneto-sensitive elastomers: Material modell meets experimental results, *13^{th} Biennial Bayreuth Polymer Symposium*, Poster PI (12), 2013.

COMPARISON OF DIFFERENT APPROACHES FOR THE NUMERICAL HOMOGENIZATION IN MAGNETO-ELECTRO-ELASTIC COMPOSITES

Z. Wang[1], A. Avakian[2], and A. Ricoeur[3]

[1,2,3] Institute of Mechanics, Chair of Engineering Mechanics / Continuum Mechanics, University of Kassel
Moenchebergstr. 7, 34125 Kassel, Germany
e-mail: zhibin.wang@uni-kassel.de

Abstract. *This work is restricted to linear material behavior, i.e. the structure is considered to be in a perfectly poled state. Different numerical homogenization methods are investigated and used to calculate effective properties of a 0-2 composite modelled in representative volume elements. Bariumtitanate (BT) and cobaltferrite (CFO) are employed in the Finite Element model, where the roles of matrix and particle are mutable. As a third variant, BT and CFO are included as functional particles in a non-functional matrix. Mixed magnetoelectromechanical boundary conditions based on different homogenization theories are applied to the model. The calculated macroscopic behaviors described by the different approaches are compared and presented in the paper. The special focus is on the prediction of coefficients of magnetoelectric coupling with respect to an optimization of the structural arrangement of the composite.*

1 Introduction

Multiferroic materials in consequence of the special atomic structure provide properties e.g. ferroelectricity and magnetostriction, which connect behaviors of different fields [2]. The coupling of magnetic and electrical fields due to the constitutive behavior of a material is commonly denoted as magnetoelectric effect (ME-effect). During the last years, increasing research activities are observed in this area because of potential application in industry. This effect, however, is only possible in a few crystal classes and is very weak. Larger coupling coefficients are obtained in composite materials, in which the ferroelectric and ferromagnetic constituents are embedded [2, 3]. Here, the (inverse) magnetostrictive and (in-) direct piezoelectric effects are coupled by the deformation of the composite, producing the macroscopic ME-effect.

On the other hand, numerical homogenization is widely used to obtain effective properties of composite structures. The homogenization as well as numerical approaches for mechanical properties have been investigated for many years and different methods have been developed. In this research area not only pure mechanical structures but also multifunctional composites with different ferroic effects are involved. Thus, classical approaches have to be extended for application to multiferroic composites revealing ambiguities which have to be investigated.

2 Theoretical framework

2.1 Linear constitutive equations

The scalar electric and magnetic potentials are motivated from the Maxwell equations for the electrostatical and magnetostatical case, such that $E_i = -\varphi^{\mathrm{el}}_{,i}$ and $H_i = -\varphi^{\mathrm{m}}_{,i}$. With the help of

these equations, the constitutive law of magnetoelectroelasticity is formulated on the basis of the thermodynamic potential

$$\Phi(\varepsilon_{ij}, E_i, H_i) = (\sigma_{ij}\varepsilon_{ij} - D_i E_i - B_i H_i)/2. \tag{1}$$

The constitutive equations in compressed notation are then obtained as

$$\sigma_q = C_{qp}\varepsilon_p - e_{iq}E_i - q_{jq}H_j, \quad D_i = e_{ip}\varepsilon_p + \kappa_{ij}E_j + g_{ij}H_j, \quad B_i = q_{ip}\varepsilon_p + g_{ij}E_j + \mu_{ij}H_j, \tag{2}$$

where σ_q, D_i, B_i, ε_p, E_i and H_i, denote stress, electric displacement, magnetic induction, strain, electric and magnetic fields. Moreover, the tensors C_{qp}, κ_{ij}, μ_{ij}, e_{ip}, q_{ip} and g_{ij} characterize elastic properties, electric and magnetic permeabilities, piezoelectric and magnetostrictive properties as well as magnetoelectric constants. The latter three tensors take the responsbilities of connecting the behaviors crossing the fields, i.e. multiferroic properties.To calculate the members of the material tensors in Eq. (2), partial differentials are introduced with quantities behind the vertical bar being constant [1]:

$$\begin{aligned}
C_{qp} &= \left.\frac{\partial \sigma_q}{\partial \varepsilon_p}\right|_{E_i,H_j}, & e_{ql} &= -\left.\frac{\partial \sigma_q}{\partial E_l}\right|_{\varepsilon_q,H_l} = \left.\frac{\partial D_l}{\partial \varepsilon_q}\right|_{E_l,H_l}, \\
\kappa_{ij} &= \left.\frac{\partial D_j}{\partial E_i}\right|_{\varepsilon_p,H_j}, & q_{lq} &= -\left.\frac{\partial \sigma_q}{\partial H_l}\right|_{\varepsilon_p,E_l} = \left.\frac{\partial B_l}{\partial \varepsilon_q}\right|_{E_l,H_l}, \\
\mu_{ij} &= \left.\frac{\partial B_j}{\partial H_i}\right|_{\varepsilon_p,E_j}, & g_{ij} &= \left.\frac{\partial D_j}{\partial H_i}\right|_{\varepsilon_p,E_j} = \left.\frac{\partial B_i}{\partial E_j}\right|_{\varepsilon_p,H_i}.
\end{aligned} \tag{3}$$

2.2 Homogenization procedures

The relationship of effective properties and the averaged fields can be given in the form $\langle\Sigma\rangle = L^* \langle Z\rangle$, where the Σ stands for (σ_{ij}, D_i, B_i) and Z for $(\varepsilon_{kl}, E_k, H_k)$, while L is the compressed tensor with all components of effective material properties. For the purpose of calculating L^* from the definitions in Eq. (3), appropriate boundary conditions are needed.

2.2.1 Voigt- and Reuss-approximation

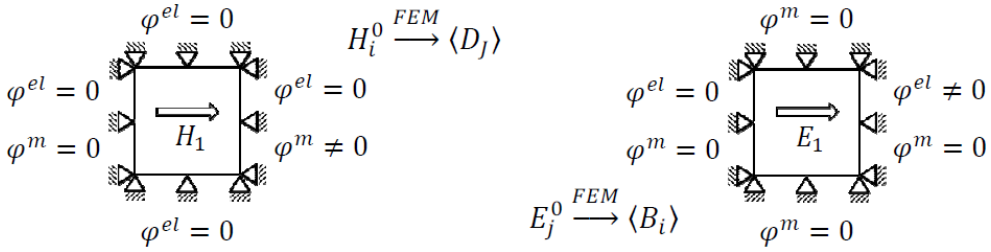

Figure 1: Boundary conditions for the calculation of the effective magnetoelectric tensor, generalized Voigt approximation

The problem of calculating elastic constants is often treated within the framework of Voigt- and Reuss-approximation, in which simple boundary conditions are applied. For Voigt-approximation the displacements as well as strain are assumed as constant and for Reuss the stress

is controlled. Here, the approaches have to be extended to multifields [4], which means the boundary conditions are formulated as:

$$\langle Z \rangle = Z^0 \qquad \text{or} \qquad \langle \Sigma \rangle = \Sigma^0 \tag{4}$$

where the superior 0 denotes the constant quantity. In these generalized approaches, constant fields are applied at the boundaries of the RVE. For example, the corresponding magnetoelectric constant in x_1-direction g_{11} is calculated as shown in Fig. 1.

2.2.2 Periodic boundary conditions (PBC)

In some composites the arrangment of particles in the matrix is ordered neatly. Each single unit (RVE) looks exactly like the neighboring units around it. From this postulate, the following equations are derived to guarantee that the structure is periodic:

$$u_i^+ - u_i^- = \varepsilon_{ij}^0 (x_i^+ - x_i^-), \quad \phi^{el+} - \phi^{el-} = -E_i^0 (x_i^+ - x_i^-), \quad \phi^{m+} - \phi^{m-} = -H_i^0 (x_i^+ - x_i^-). \tag{5}$$

Here, constant strains, electric and magnetic fields are applied to the RVE. The displacements as well as electric and magnetic potentials of upper and lower, left and right bounds (+, -) are corresponding. It has to be noticed that these requirements are implicit. Although the relationship of fields in Eq. (5) must be obeyed, the concrete quantites of displacements, electric and magnetic potentials are unknown. For example, the corresponding magnetoelectric constant in x_1-direction g_{11} is calculated as shown in Fig. 2.

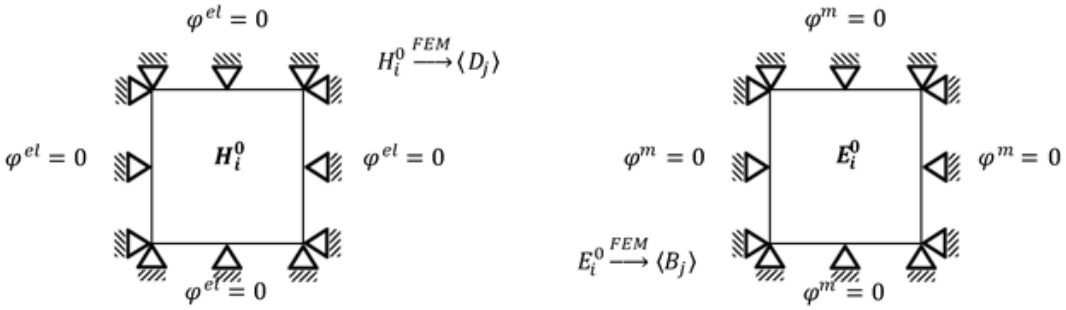

Figure 2: Periodic boundary conditions for the calculation of the effective magnetoelectric tensor

3 Results

In this paper two- (BT-CFO) and three- (BT-CFO-epoxy) phase composites are considered, where epoxy is a non-functional matrix material. The materials of matrix and particles in two-phase composites are commutable. The RVE models, see Fig. (3), are generated automatically. The coordinates as well as particle sizes and shapes are statisticaly distributed for a given volume fraction (Gaussian distribution). The simulations are performed for different volume fractions using an Abaqus USER-subroutine [1]. The calculated effective properties for each homogenization method mostly approach to similar values. This holds in particular, if the volume ration of one particle and the whole RVE is small. If the particle size increases, results of the different methods diverge. Further, the different definitions of coupled properties in Eq. 3 yield small differences.

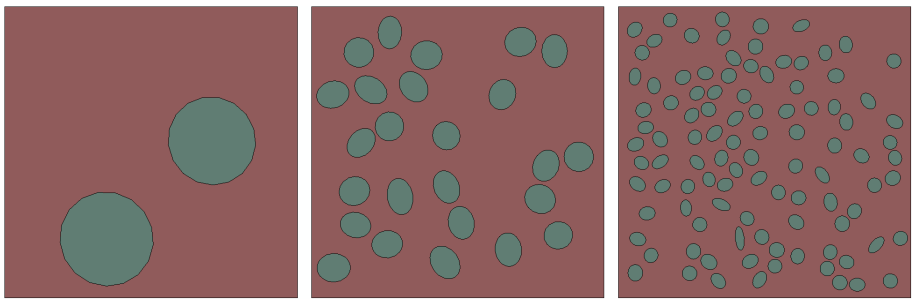

Figure 3: Different RVEs of multiferroic composite. All models have equal volume fraction of particles

A BT-CFO-epoxy composite is taken as numerical example and the effective properties are compared. In this model, each kind of particles (BT and CFO) has a volume fraction of 10%. The ratio between the volume of a single particle and the RVE is $0.2 \cdot 10^{-3}$. The RVE and particle distributions are those of the right sketch in Fig. 3. Tab. 1 presents the effective properties of the composite, where the coupled effective properties according to Eq. (3) have two different definitions of which the averaged values are taken. The results show the accordance of numerically calculated properties based on different approaches. Larger differences are only observed at C^*_{66} and g^*_{22}.

	VOIGT	REUSS	PBC		VOIGT	REUSS	PBC
C^*_{11}[GPa]	7.341	7.332	7.324	$e^*_{11}(\times 10^6$[N/GVm])	1.202	1.192	1.195
C^*_{22} [GPa]	7.402	7.393	7.389	$e^*_{12}(\times 10^5$[N/GVm])	-3.710	-3.700	-3.627
C^*_{12} [GPa]	3.667	3.647	3.741	$e^*_{26}(\times 10^5$[N/GVm])	8.630	9.069	9.051
C^*_{66} [GPa]	1.792	1.192	1.796	$q^*_{11}(\times 10^4$[GVfs/m^2])	3.826	3.784	4.289
$\kappa^*_{11}(\times 10^8$[N/GV^2])	1.157	1.156	1.156	$q^*_{12}(\times 10^4$[GVfs/m^2])	2.743	2.723	2.925
$\kappa^*_{22}(\times 10^8$[N/GV^2])	1.146	1.144	1.145	$q^*_{26}(\times 10^4$[GVfs/m^2])	-1.496	-1.561	-1.923
$\mu^*_{11}(\times 10^6$[GV^{2}fs^2/m^2])	1.442	1.440	1.440	g^*_{11}[Nfs/VC]	-2.989	-2.942	-3.224
$\mu^*_{22}(\times 10^6$[GV^{2}fs^2/m^2])	1.430	1.428	1.429	g^*_{22}[Nfs/VC]	4.609	4.668	6.982

Table 1: Effective properties of a 0.1BT-0.1CFO-0.8epoxy composite

REFERENCES

[1] A. Avakian, A. Ricoeur. Enhancement of magnetoelectric coupling in multiferroic composites via FEM simulation, Proceedings in *Advances in Structural Engineering and Mechanics*, 2013.

[2] C. W. Nan, M. I. Bichurin, S. Dong, D. Viehland and G. Srinivasan. Multiferroic magnetoelectric composites: Historical perspective, status, and future directions, *Journal of Applied Physics*, 103, 3, 031101–031101–35, 2008

[3] V. V. Shvartsman, F. Alawneh, P. Borisom, D. Kozodaev and D. C. Lupascu. Converse magnetoelectric effect in $CoFe_2O_4$–$BaTiO_3$ composites with a core–shell structure, *Smart Materials and Structures*, 20, 075006, 2011

[4] H. Qing, S. Qing. *Macro–Micro Theory on Multifield Coupling Behavior of Heterogeneous Materials*. Higher Education Press, Beijing and Springer–Verlag GmbH Berlin Heidelberg, 2008

THE INFLUENCE OF FIELD-INDUCED PHASE TRANSITIONS ON THE MECHANICAL AND ELECTRICAL BEHAVIOR OF PEROVSKITE FERROELECTRICS

Kyle G. Webber, Yo-Han Seo, Florian H. Schader, Daniel J. Franzbach, and Jurij Koruza

Institute of Materials Science, Technische Universität Darmstadt
Alarich-Weiss-Straße 2, Darmstadt, Germany
email: webber@ceramics.tu-darmstadt.de

Abstract. *During the application of an external electrical or mechanical field, ferroelectric perovskite ceramics display nonlinear, hysteretic constitutive behavior. In addition to the ferroelectric and ferroelastic response, due to the nucleation and growth of domains, field-induced phase transitions have also been observed that can lead to large jumps in polarization and strain. In the following, various characterization and simulation techniques have been employed to elucidate the role of external fields on the phase stability in polycrystalline and single crystal perovskite ferroelectrics.*

1 Introduction

Due to their excellent electromechanical coupling, ferroelectric materials are widely used in numerous transduction applications. In addition to piezoelectricity, it is understood that external electrical and mechanical fields are capable of both nucleating domains and moving domain walls, which results in an intrinsic and extrinsic contribution to the piezoelectric response [1]. The most commercially important of these materials is the $Pb(Zr,Ti)O_3$ (PZT) system, which is typically used in the compositional range around the morphotropic phase boundary (MPB) that separates the ferroelectric rhombohedral phase (R) from the ferroelectric tetragonal phase (T) [2]. In addition to a relatively temperature stable piezoelectric response, PZT can also be easily tuned through chemical doping and microstructure modification [2]. Recently, however, legislation in Europe and elsewhere has lead to an intensive search for a lead-free alternative [3]. A number of possible candidates have been found, with $K_{0.5}Na_{0.5}NbO_3$ (KNN) [4] and $Bi_{1/2}Na_{1/2}TiO_3$ (BNT) –based [5] materials showing the most promise. As part of this research, there has been a renewed interest in field induced phase transitions, as they have been shown to be the origin of the large unipolar strain observed in $Bi_{1/2}Na_{1/2}TiO_3$–$BaTiO_3$– $K_{0.5}Na_{0.5}NbO_3$ (BNT-BT-KNN). During loading it has been shown that the material undergoes a reversible relaxor→ferroelectric (RE→FE) phase transition, which is modulated by the KNN content that destabilizes the long–range ferroelectric order [6]. Recent investigations have also attempted to tailor this behavior through inclusion of second phase ferroelectric seeds in a matrix material undergoing a RE→FE phase transition [7].

In the following work, the influence of stress and electric field on the macroscopic constitutive behavior of perovskite ferroelectrics will be discussed for polycrystalline $Pb(Zr_{1-x}Ti_x)O_3$ across the MPB. The experimental data are contrasted with X-ray powder diffraction results, which give insight into the influence of applied fields on the stable phase. The results provide indirect evidence of field-induced phase transitions in polycrystalline ferroelectrics.

2 Experimental Methodology

The ferroelastic and ferroelectric behavior of Ba and Nb modified $Pb(Zr_{1-x}Ti_x)O_3$ solid solution ceramics $Pb_{0.98}Ba_{0.01}(Zr_{1-x}Ti_x)_{0.98}Nb_{0.02}O_3$ with varying $PbTiO_3$ content (x = 0.40, 0.47, 0.49, 0.51, 0.53, 0.55, and 0.60) has been characterized. In the following discussion, the composition is referred to by the $PbTiO_3$ content, e.g., PZT45 for x = 0.45. The powders were prepared by mixed-oxide method using PbO

(Sigma, 99.9%), TiO_2 (Alfa, 99.8%), ZrO_2 (TZ-0, Tosoh), Nb_2O_5 (Sigma, 99.9%), and BaCO3 (Alfa, 99.8%) as precursors. Powder mixtures were homogenized in isopropyl alcohol in a planetary mill and calcined twice at 900 °C for 1 h with a heating/cooling rate of 5 °C/min and milling after each calcination step. After drying and sieving, the powder mixtures were pressed into pellets and sintered at 1275 °C for 2 h with a heating/cooling rate of 5 °C/min.

X-ray powder diffraction was performed using PANalytical X'Pert PRO diffractometer (Cu Kα1/Kα2 radiation) at room temperature. For the XRD analysis of the sintered samples, the pellets were crushed into powders. The data were collected in the 2θ range from 15° to 80° with a step size of 0.026°/100 s. The cell parameters of the PZT samples were obtained from the Rietveld analysis. The chosen space groups for these refinements were P4mm (SG no 99) and R3m (SG no 160) for the tetragonal and rhombohedral PZT phases, respectively. Additional experimental details are available elsewhere [8].

The ferroelectric behavior was characterized at room temperature for each composition on disk samples with diameter of 4.2 mm and a thickness of 1 mm. Prior to electrical characterization the samples were annealed at 600 °C to ensure that each sample was unpoled prior to testing. Following annealing, silver electrodes were sputtered on the ground circular faces. During measurement a triangular wave electrical load was applied to the sample at a frequency of 50mHz with a high voltage amplifier (Trek Model 20/20C) and a function generator (Agilent 33220A). The maximum electric field was 6 kV/mm. The unipolar strain and polarization were measured during testing with a linear variable differential transducer and a Sawyer-Tower circuit, respectively.

Ferroelastic samples had a diameter of □5.8 mm and a height of □6 mm. Prior to measurement the samples were annealed at 600 °C to ensure that each sample was unpoled prior to testing. The ferroelastic behavior was characterized at room temperature with a screw-type load frame fitted with a linear variable differential transformer. A maximum mechanical compressive stress up to − 390 MPa with a loading and unloading rate of −3.7 MPa/s was applied to the specimen.

3 Results

XRD Measurements

The structural investigation using XRD revealed that PZT 47, 49, 51, 55, and 60 were tetragonal at room temperature, while PZT 40 and 45 were rhombohedral. It is important to note, however, that PZT 45 and 47, the two compositions closest to the MPB, also contained a minority tetragonal and rhombohedral phase, respectively. The amount of the minority phase was, however, too small to accurately determine the lattice parameters. From the XRD analysis, the MPB at room temperature is located between PZT 45 and 47. This is further from the $PbTiO_3$-rich side of the phase diagram than in the undoped PZT system [2]. The cell parameters determined during the XRD refinements were used to calculate the tetragonal (δ_T) and rhombohedral (δ_R) spontaneous lattice distortion for each composition with the following equations:

$$\delta_T = \frac{c}{a} - 1 \tag{1}$$

$$\delta_R = \frac{d_{111}}{d_{11\bar{1}}} - 1 \tag{2}$$

where c and a are the tetragonal lattice parameters and d_{111} and $d_{11\bar{1}}$ are the rhombohedral lattice spacings. The resultant lattice distortion values are shown in Figure 1.

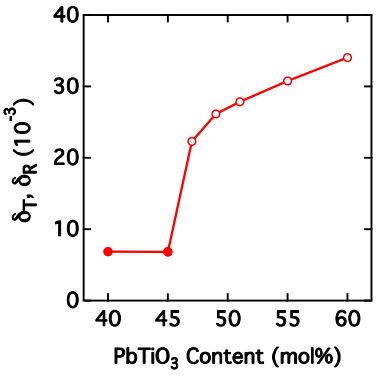

Figure 1. Lattice distortion of $Pb(Zr_{1-x}Ti_x)O_3$ in the vicinity of the MPB. The filled symbols represent the rhombohedral phase and the open symbols represent the tetragonal phase.

Ferroelectric Measurements

The macroscopic strain-electric field behavior for PZT 40, 45, 47, 49, 55 and 60 during the initial poling cycle from the virgin state is shown in Figure 2. These measurements show the initial poling of the material, which gives information on the development of remanent strain ($\boldsymbol{\varepsilon_r}$) and the poling field, i.e., the electric field required to ferroelectrically switch domains from the unpoled state, which is defined at the inflection point during electric loading. From these measurements the influence of the MPB, located between PZT 45 and PZT 47, can be clearly observed. In the vicinity of the MPB there is an increase in the remanent and maximum strain that corresponds to a decrease in the poling field. In addition, the overall form of the hysteresis changes are well, where an increasing $PbTiO_3$ content results in a more continuous strain evolution during electrical loading.

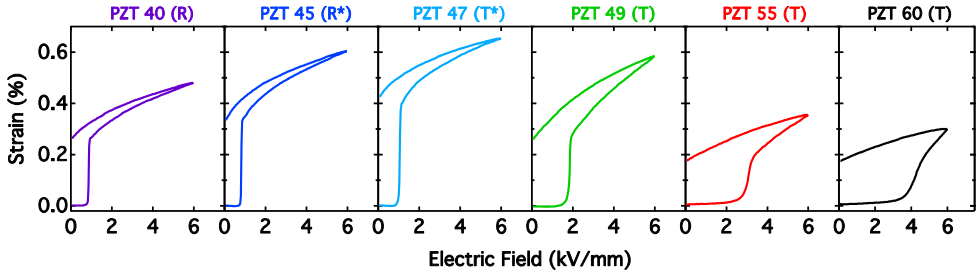

Figure 2. Strain-electric field behavior of $Pb(Zr_{1-x}Ti_x)O_3$ during poling from the virgin state. The stars denote the presence of a minority phase.

Ferroelastic Measurements

Figure 3 shows the room temperature stress-strain behavior of unpoled PZT 40, 45, 47, 49, 55 and 60. Similarly to the ferroelectric measurements, it can be clearly observed that the proximity to the MPB influences the macroscopic constitutive behavior significantly, resulting in a decreasing coercive stress, defined at the inflection point during mechanical loading, and an increasing hysteresis with increasing $PbTiO_3$ content. Interestingly, in contrast to the electrical measurements, the largest remanent strain was not observed near the MPB, rather on the tetragonal side of the MPB.

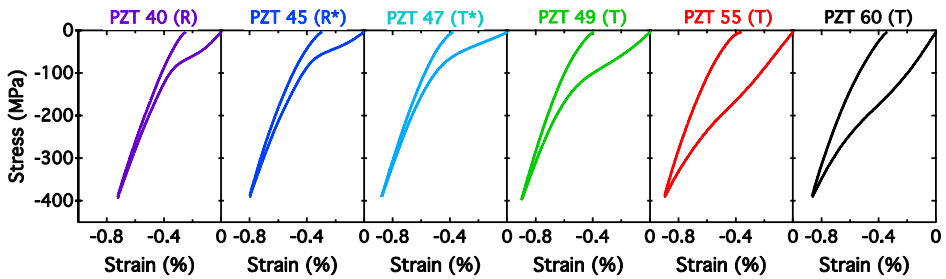

Figure 3. Ferroelastic behavior of unpoled $Pb(Zr_{1-x}Ti_x)O_3$. The stars denote a minority phase.

4 Discussion

From the observed ferroelectric and ferroelastic behavior, the resulting remanent strains as a function of PZT composition were determined, shown in Figure 4a. For both loading conditions, an increase in the remanent strain can be found in the vicinity of the MPB, which indicates that external electrical and mechanical fields can reorient more domains. In the case of high $PbTiO_3$ content compositions, this is partially due to the maximum fields applied in relation to the coercive electric field and stress. For example, the coercive stress of PZT 47 was found to be approximately –50 MPa, while PZT 60 displayed a value of nearly –200 MPa. It is expected that the applied –390 MPa compressive stress has a larger influence on PZT 47 than PZT 60. However, if we normalize the observed remanent strain values by the switching strains ($\boldsymbol{\varepsilon_s}$) of the untested material (Fig. 1), we find a much different picture. Namely, the $\boldsymbol{\varepsilon_r/\varepsilon_s}$ ratio was maximum in the rhombohedral composition. Interestingly, in both the electrical and mechanical case, the observed $\boldsymbol{\varepsilon_r/\varepsilon_s}$ ratio is larger than the theoretical value allowed for by ferroelectricity or ferroelasticity. During ferroelectric and ferroelastic loading, the maximum $\boldsymbol{\varepsilon_r/\varepsilon_s}$ ratio for the rhombohedral phase is 0.424 and –0.285, respectively. This finding strongly indicates the presence of hysteretic processes in addition to domain wall motion during electrical and mechanical loading, such as field induced phase transitions that have been observed in other perovskite ferroelectric materials.

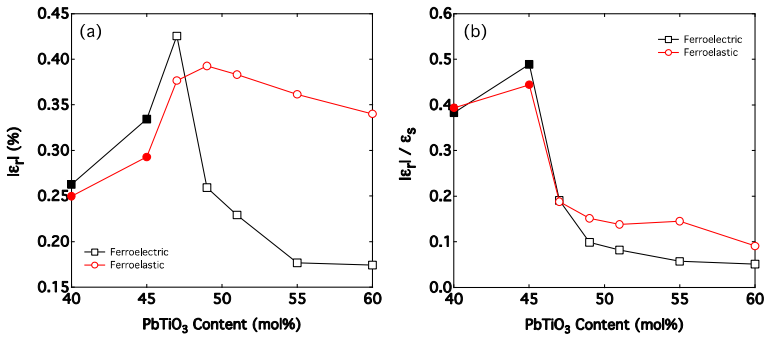

Figure 4. The remanent strain (a) and the remanent strain normalized by the switching strain (b). Filled symbols represent the rhombohedral phase and open symbols represent the tetragonal phase.

5 Conclusions

Macroscopic ferroelectric and ferroelastic constitutive behavior has been characterized for a various PZT compositions in the vicinity of the MPB. Together with lattice parameters determined with and XRD analysis, it was found that the observed remanent strain was larger than theoretically allowed by domain wall motion alone. This indicates the presence of additional mechanisms, such as field induced phase transitions, that contribute to the remanent strain.

REFERENCES

[1] D. Damjanovic. *Physical Review B,* 55(2):R649-R652, 1997.
[2] B. Jaffe, W.R. Cook, and H. Jaffe. *Piezoelectric Ceramics*. Academic Press, London, 1971.
[3] EU-Directive 2011/65/EU: *Restriction of the use of certain hazardous substances in electrical and electronic equipment (RoHS)*. Off. J. Eur. Union, 88, 2012.
[4] Y. Saito, H. Takao, T. Tani, T. Nonoyama, K. Takatori, T. Homma, T. Nagaya, and M. Nakamura. *Nature,* 432(7013):84-87, 2004.
[5] S.T. Zhang, A.B. Kounga, E. Aulbach, H. Ehrenberg, and J. Rödel. *Applied Physics Letters,* 91(11):112906, 2008.
[6] W. Jo, R. Dittmer, M. Acosta, J. Zang, C. Groh, E. Sapper, K. Wang, and J. Rödel. *Journal of Electroceramics,*; 29(1): 71-93, 2012.
[7] C. Groh, D.J. Franzbach, W. Jo, K.G. Webber, J. Kling, L.A. Schmitt, H.J. Kleebe, S.J. Jeong, J.S. Lee, and J. Rödel. *Advanced Functional Materials,* 24(3):356–362, 2014.
[8] Y.H. Seo, D.J. Franzbach, J. Koruza, A. Benčan, B. Malič, M. Kosec, J.L. Jones, and K.G. Webber. *Physical Review B*. 87(9):094116. 2013.

THERMAL DIFFUSION IN POLYMER BLENDS

Kerstin Weinberg

Chair of Solid Mechanics, University of Siegen
Paul-Bonatz-Straße 9-11, 57068 Siegen, Germany
e-mail: kerstin.weinberg@uni-siegen.de

Abstract.

In this contribution a model of segregation of temperature sensitive binary blends triggered by non-uniform local heating is presented. Capturing the microstructural evolution results in a phase-field model of Cahn-Hilliard type extended by contributions originated from thermophoresis. The diffusion problem constitutes a partial differential equation involving spatial derivatives of fourth order. Consequently, the variational formulation of the problem mandates approximation functions which are at least piecewise smooth and globally C^1-continuous. In order to fulfill these requirements a spline-based finite element scheme is provided.

Numerical simulations of phase separation subjected to non-uniform temperature field within a binary polymer blend consisting of poly(dimethylsiloxane) and poly(ethyl-methylsiloxane) will illustrate the presented approach.

1 Introduction

Applications of polymers blend may be found in plenty of applications, ranging from polymer solutions in adhesives over cosmetics to industrial manufacturing processes such as the production of microelectronic components. In order to combine beneficial characteristics of single components specific multiphase mixtures are established. In general, such polymer mixtures are subjected to a great variety of microstructural changes such as separation of phases and coarsening processes. However, comparatively little studies have been performed for phase behavior of polymer blends subjected to local non-uniform temperature fields.

2 Modeling thermal diffusion and phase decomposition

Thermal diffusion comprises that different particle types move differently under the force of the temperature gradient which, therefore induces a diffusive mass flux $\mathbf{J}_T$.

$$\mathbf{J}_T = -\rho D_T c\,(1-c)\,\nabla T. \tag{1}$$

In a pure phase it is not possible to achieve thermal diffusion since $\mathbf{J}_T$ vanishes for $c = 0$ and $c = 1$. Usually the thermally activated diffusive mass current may occur in either direction, dependent on the materials involved. Thermophilic substances diffuse up the temperature gradient. Thermophobic materials diffuse down the temperature gradient. Typically the heavier/larger species in a mixture exhibits a thermophobic behavior while the lighter/smaller species exhibit thermophilic behavior. In addition to the sizes of the various types of particles and the steepness of the temperature gradient, the heat conductivity and heat absorption of the

particles play a role in thermal diffusion. However $\mathbf{J}_T$ leads to a buildup of a concentration gradient, which is accompanied by a generalized Fickian type mass diffusion current.

$$\mathbf{J}_D = -\rho \mathbf{M} \nabla \mu \tag{2}$$

Inserting entire diffuse mass flux $\mathbf{J} = \mathbf{J}_D + \mathbf{J}_T$ into the general diffusion equation (for a detailed derivation see [1]) we obtain a modified Cahn-Hilliard equation, i.e., in its strong formulation the problem reads: Find $c : \Omega \times \left(0, \overline{t}\right) \to \mathbb{R}$ such that

$$\frac{\partial c}{\partial t} = \nabla \cdot \left(\mathbf{M} \nabla \left(\partial_c \Psi^{\text{con}} - \lambda \Delta c\right) + D_T c \left(1 - c\right) \nabla T\right) + \xi \left(\mathbf{x}, t\right) \quad \text{in } \Omega \times \left(0, \overline{t}\right) \tag{3}$$

holds. The initial concentration is given, $c\left(\mathbf{x}, 0\right) = c_0\left(\mathbf{x}\right)$ in Ω and, in order to account for the conservation of mass, homogeneous Neumann boundary conditions are prescribed.

$$\mathbf{j} \cdot \mathbf{n} = -\left(\mathbf{M} \nabla \mu + D_T c \left(1 - c\right) \nabla T\right) \cdot \mathbf{n} = 0 \quad \text{in } \partial\Omega \times \left(0, \overline{t}\right) \tag{4}$$

$$\nabla c \cdot \mathbf{n} = 0 \quad \text{in } \partial\Omega \times \left(0, \overline{t}\right) \tag{5}$$

Additionally, the temperature field T must comply with the heat equation

$$\frac{\partial T}{\partial t} = D_{\text{th}} \Delta T + \frac{\alpha}{\rho c_p} I. \tag{6}$$

Here D_{th} denotes the thermal diffusivity. Eq. (6) shows that the heat source term is proportional to the laser intensity I, where ρ is the average density of the heated medium, α is the optical absorption coefficient and c_p is the specific heat capacity at constant pressure.

3 Numerical approximation in space and time

For the spatial discretization of the diffusion problem at hand we employ a Galerkin method basing on the concept of isogeometric finite element analysis. To this end the space of test/ansatz functions $H^2\left(\Omega\right)$ is approximated by a finite dimensional subspace $\mathcal{V}^h \subset H^2\left(\Omega\right)$ which is regarded to be a span of C^1-continuous B-spline basis functions. These basis functions offer high-order accuracy and numerical robustness, cf. [2,4]. In this setting the employed B-spline basis functions are deduced from the classical de Boor recursion formula on element level. The construction of multivariate B-splines is realized by the usual tensor-product formalism considering univariate B-splines.

Let n be the dimension of $\mathcal{V}^h$ then the discrete solution c^h and the discrete testfunctions δc^h can be depicted as linear combinations of basis functions N_i in $\mathcal{V}^h$:

$$\delta c^h = \sum_{i=1}^{n} a_i N_i \quad \text{and} \quad c^h = \sum_{j=1}^{n} b_j N_j \tag{7}$$

Note that the applied basis functions are non-interpolatory at nodes as it is usual for standard Lagrangian basis functions. Therefore the values of the solution coefficients b_j cannot be assigned directly with the function values at the nodes. In fact, the function values arise from a linear combination of adjacent basis functions.

The temporal discretization is straightforward. The considered time interval $\mathcal{T}$ is divided into n_t subintervals $I_n = [t_n,\, t_{n+1}]$. The first order time derivative is approximated by finite differences

$$\frac{\partial c}{\partial t} = \frac{c_{n+1} - c_n}{\Delta t} \tag{8}$$

with (equidistant) time step $\Delta t = t_{n+1} - t_n$. The time integration is performed by an implicit Crank-Nicholson scheme, known to be second-order accurate.

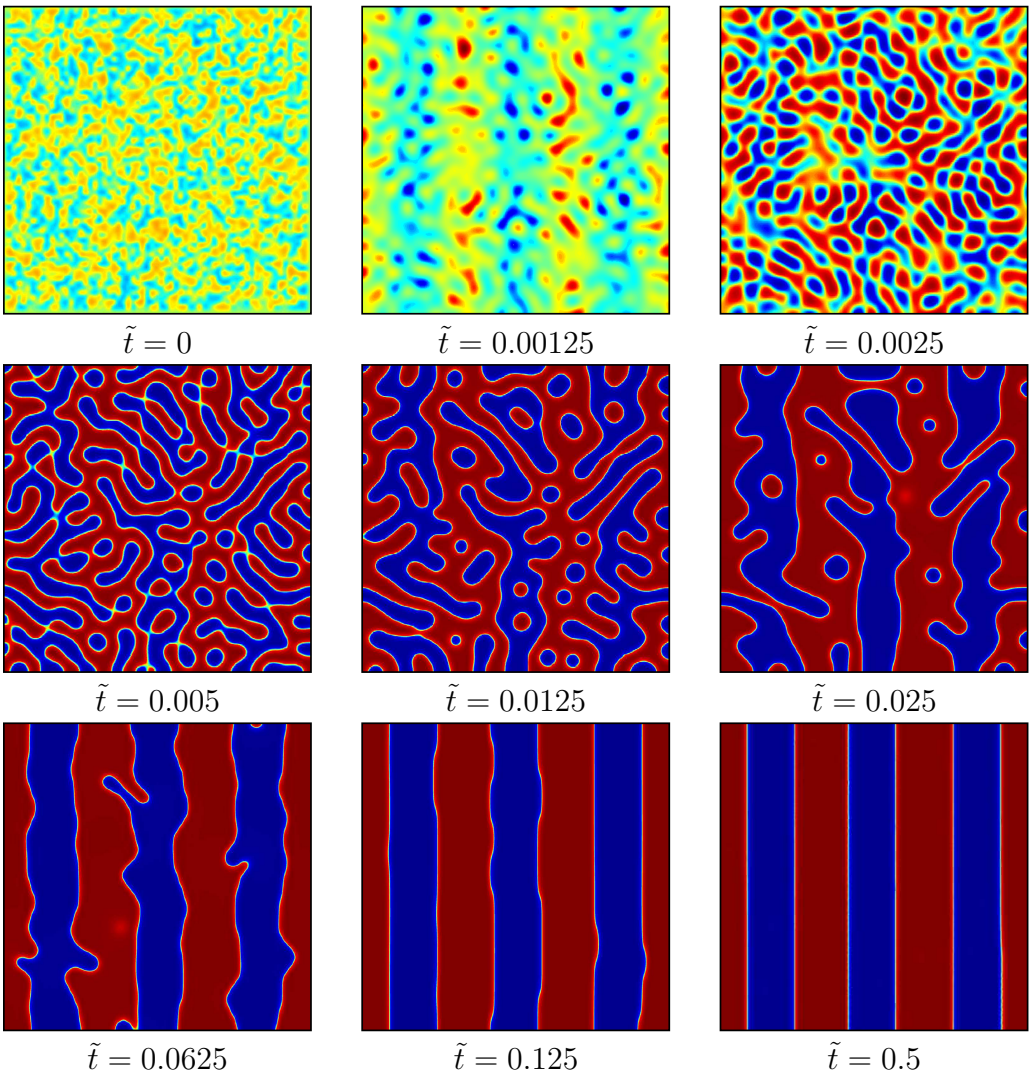

Figure 1: Simulation results for a critical PDMS/PEMS polymer blend subjected to a periodic forcing.

4 Thermal decomposition of a critical PDMS/PEMS system

In the following we present a numerical simulation of phase separation in the presence of local temperature fields within a real binary polymer blend consisting of polydimethylsiloxane (PDMS) and polyethylmethylsiloxane (PEMS). Both are terminated with trimethylsiloxane endgroups, one methyl respectively ethyl group in the repeating unit makes the only difference.

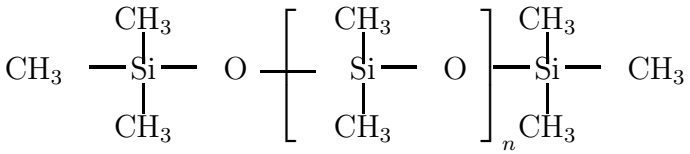

(PDMS)

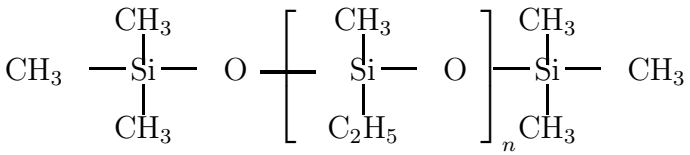

(PEMS)

A polymer blend in a critical composition of 55% polydimethylsiloxane and 45% polyethylmethylsiloxane, which has been investigated experimentally, see Fig. 2, will be simulated. Start-

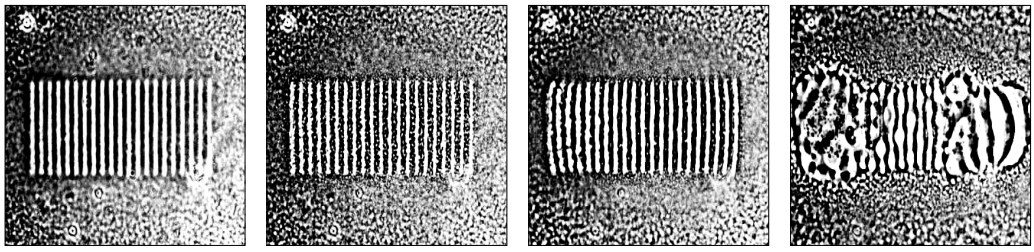

$t = 442\,\mathrm{s}$ $t = 802\,\mathrm{s}$ $t = 1524\,\mathrm{s}$ $t = 3407\,\mathrm{s}$

Figure 2: Micrographs from optical grating experiments of a PDMS/PEMS blend. The specimen size is about $300\,\mu\mathrm{m} \times 200\,\mu\mathrm{m}$. Subfigures are adapted from [3].

ing from a homogeneous one-phase configuration the early stages of microstructural evolution are driven by spinodal decomposition of phases. Only gradually the periodic forcing asserts itself against the suppression of phase decomposition. Over time the inhomogeneous temperature gradient increasingly coins the microstructure. A periodic stripe pattern evolves and destroys the typical coarsening scenario as customary for standard Cahn-Hilliard systems.

These results are displayed in Fig. 1 and fit nicely to the optical grating experiments illustrated in Fig. 2. The PEMS-rich phases appear here as darker regions. The second micrograph of Fig. 2 shows that horizontal lamellea-shaped phases are present between the evolving periodic stripe patterns. This phenomenon is clearly reproduced during simulation in Fig. 1. Due to the fact that PDMS is thermophilic, the laser light generates locally heated domains where a PDMS enrichment takes place. During the experiment ($t = 0\,\mathrm{s}$ - $2366\,\mathrm{s}$) there are sequences where the laser is turned on and later turned off in order to study the interplay between thermal diffusion and coarsening effects, cf. [3]. In addition, the stability of the evolved structure is investigated. At $t = 2366\,\mathrm{s}$ the laser illumination is completely turned off and the system is left on its own devices. At $t = 3407\,\mathrm{s}$ a steady decay of the periodic microstructure can be observed. Due to the surface energy of the single phases the outer lines crook to reach a configuration of constant curvature that is achieved in a circular structure.

References

[1] D. Anders and K. Weinberg, Thermophoresis in binary blends. Mechanics of Materials, 47:33-50, 2012.

[2] D. Anders and K. Weinberg. Variational approach to the decomposition of unstable viscous fluids and its consistent numerical approximation. ZAMM - Journal of Applied Mathematics and Mechanics, 91(8):609–629, 2011

[3] A. Voit. Photothermische Strukturierung binärer Polymermischungen. Ph.D. thesis. University of Bayreuth, 2007.

[4] D. Anders, K. Weinberg and R. Reichardt. Isogeometric analysis of thermal diffusion in binary blends. Computational Materials Science, 52(1), 182188, 2012.

TUNING THE ELECTRIC POLARIZATION IN $CoFe_2O_4/BaTiO_3$ NANOCOMPOSITES BY MAGNETIC FIELDS

H. Wende[1]

[1]Faculty of Physics and Center for Nanointegration Duisburg-Essen (CENIDE),
Universität Duisburg-Essen, Lotharstr. 1, D-47048 Duisburg, Germany
e-mail: heiko.wende@uni-due.de
web: http://www.uni-due.de/physik/wende/

Abstract. *Multiferroic materials showing both magnetic and electric ordering allow an additional degree of freedom in the design of actuators, transducers and storage devices and thus have attracted scientific interest from the technological perspective as well as from basic research. Because the choice of single-phase multiferroic materials being suitable at room temperature is limited, the use of magnetoelectric two-phase composites has proven to be more promising [1]. Here we study ferrimagnetic $CoFe_2O_4$ (CFO) nanopillars embedded in a ferroelectric $BaTiO_3$ (BTO) matrix (Fig. 1 a)). They operate at room temperature and are free of any resource-critical rare-earth element, which makes them interesting for potential applications. Prior studies succeeded in showing strain-mediated coupling between the two subsystems. In particular, the electric properties can be tuned by magnetic fields and the magnetic properties by electric fields. Here we take the analysis of the coupling to a new level utilizing soft X-ray absorption spectroscopy and its associated linear dichroism [2]. We demonstrate that an in-plane magnetic field breaks the tetragonal symmetry of the (1,3)-type $CoFe_2O_4/BaTiO_3$ structures (Fig. 1 b)) and discuss it in terms of off-diagonal magnetostrictive-piezoelectric coupling. This coupling creates staggered in-plane components of the electric polarization, which are stable even at magnetic remanence due to hysteretic behaviour of structural changes in the $BaTiO_3$ matrix. The competing mechanisms of clamping and relaxation effects are discussed in detail. The effect in the electric in-plane polarization of BTO obtained in this work extends over a large area. Under the constraint of completely regular arrays of CFO nanopillars, one might even envisage data-storage concepts by encoding the local polarization patterns of single nanopillars via external current-controlled local magnetic fields.*

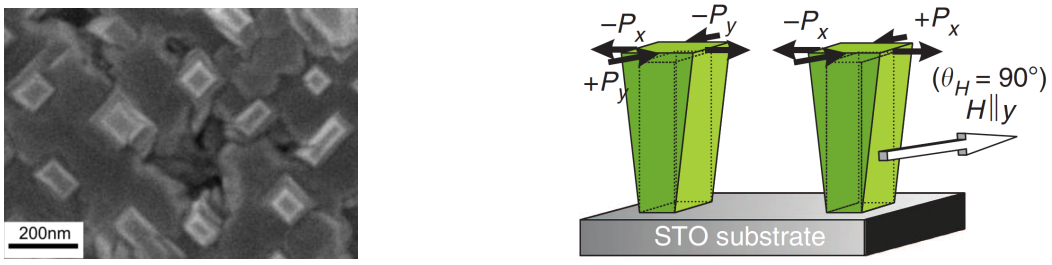

a) b)

Figure 1: a) Scanning electron microscopy image of the sample corresponding to a top view on the nanopillar structure. b) Schematic presentation of the strained CFO nanopillars in the BTO matrix (not shown) when applying a magnetic field perpendicular to the pillars [2].

Acknowledgment

This work is carried out in collaboration with Carolin Schmitz-Antoniak, Pavel Borisov, Sven Stienen, Anne Warland, Bernhard Krumme, Wolfgang Kleemann (University of Duisburg-Essen), Detlef Schmitz, Ralf Feyerherm, Esther Dudzik (Helmholtz-Zentrum Berlin für Materialien und Energie) and Frank M. F. de Groot (Universiteit Utrecht).

REFERENCES

[1] H. Zheng, J. Wang, S. E. Lofland, Z. Ma, L. Mohaddes-Ardabili, T. Zhao, L. Salamanca-Riba, S. R. Shinde, S. B. Ogale, F. Bai, D. Viehland, Y. Jia, D. G. Schlom, M. Wuttig, A. Roytburd, R. Ramesh, Multiferroic $BaTiO_3$-$CoFe_2O_4$ nanostructures, *Science* **303**, 661663 (2004).

[2] C. Schmitz-Antoniak, D. Schmitz, P. Borisov, F.M.F. de Groot, S. Stienen, A. Warland, B. Krumme, R. Feyerherm, E. Dudzik, W. Kleemann and H. Wende, Electric in-plane polarization in multiferroic $CoFe_2O_4$/$BaTiO_3$ nanocomposite tuned by magnetic fields, *Nature Communications* **4**, 2051 (2013).

PHASE FIELD STUDY ON DOMAIN STRUCTURE STABILITY AND DOMAIN WALL CONDUCTIVITY BY SCREENING CHARGE IN FERROELECTRICS WITH POINT DEFECTS

Yinan Zuo[1], Yuri A. Genenko[1], and Bai-Xiang Xu[1]

[1] Institute of Materials Science, Department, Technische Universität Darmstadt
Jovanka-Bontschits-Strasse 2, Darmstadt, Germany
e-mail: zuo@mfm.tu-darmstadt.de

Abstract. *Doping in ferroelectrics can influence their properties significantly. The bound charges appear at domain wall for head-to-head or tail-to-tail domain structures and they give rise to an electric field, making the domain structure unstable. For ferroelectrics with semiconducting feature, the electrons and holes can accumulate near the domain wall and screen the bound charges. Domain structures can be stabilized by those free charges and the domain wall conductivity is enhanced. A phase field model is applied to study two defect systems. One is an ideal defect system where the only point defects are oxygen vacancies and the other is a realistic defect system where doping of manganese generates multiple kinds of point defects. It is shown that the domain wall conductivity enhanced by electrons or holes depends on many factors (domain configuration, type of defect system, concentration of certain point defects etc). The simulation results can help to explain some corresponding experimental results on conductivity of domain walls.*

1 Introduction

Ferroelectric materials are widely used in electronic industry. "Up-down", "head-to-head" and "tail-to-tail" domain walls are three possible 180 degree domain walls. The "head-to-head" and "tail-to-tail" domain walls are not stable in ferroelectrics without semiconducting feature because of the electric field generated by the bound charges. The driving force has been studied quantitatively [1]. After doping ferroelectrics can contain point defects which can give rise to ionic and free space charges. Then the materials can be treated as semiconductors. Head-to-head and tail-to-tail domain configurations can be stabilized by the screening charge [2]. There are experimental verifications on head-to-head and tail-to-tail domain wall conductivity [3][4].

2 Phase field model of ferroelectrics with semiconducting feature

The equilibria for mechanical stress and electric displacement are fulfilled,

$$\sigma_{ij,j} = 0, \qquad \text{in } \Omega, \tag{1}$$

$$D_{i,i} = \rho(\phi), \qquad \text{in } \Omega. \tag{2}$$

The Landau-Ginzburg equation is

$$\frac{\partial P_i}{\partial t} = -M\frac{\delta H}{\delta P_i}, \tag{3}$$

where P_i is the spontaneous polarization vector and H is the Gibbs free energy. This equation describes the domain structure evolution in ferroelectrics.

In Mn-doped barium titanate, six possible sources can make contribution to the local space charge: oxygen vacancies, titanium vacancies, oxygen-titanium di-vacancies, manganese-titantium substitutions, electrons and holes. Oxygen vacancies act as donors, whereas titanium vacancies, oxygen-titanium di-vacancies and manganese-titanium substitutions act as acceptors according to their valency. The space charge then has the expression [5]

$$\begin{aligned}\rho(\phi) = -qN_C F_{1/2}\left(\frac{E_F - E_C + q\phi}{kT}\right) + qN_V F_{1/2}\left(\frac{E_V - E_F - q\phi}{kT}\right)\\ +qz_{V_O}N_{V_O}t_{V_O}(\phi) - qz_{V_{Ti}}N_{V_{Ti}}t_{V_{Ti}}(\phi) - qz_{[V_{Ti}-V_O]}N_{[V_{Ti}-V_O]}t_{[V_{Ti}-V_O]}(\phi)\\ -qz_{Mn_{Ti}}N_{Mn_{Ti}}t_{Mn_{Ti}}(\phi).\end{aligned} \tag{4}$$

We apply the scheme suggested by van Halen et al. for estimation of the Fermi integral [6].

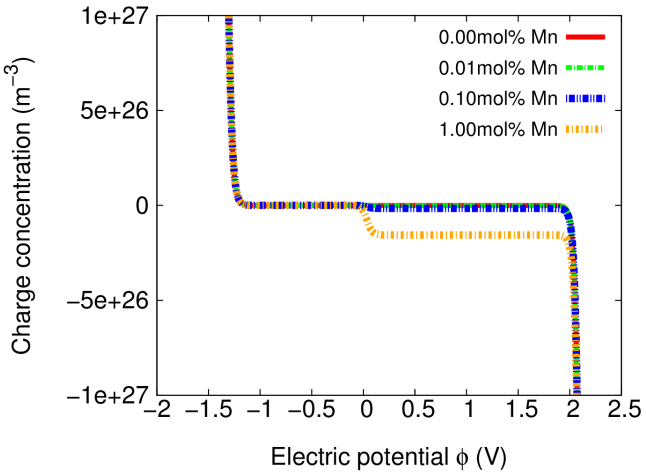

Figure 1: Variation of the space charge with respect to the electric potential in ferroelectrics with a realistic defect system according to Eq.(4).

3 Simulation results

A barium titanate sample with its left and right edge short circuited is studied by the phase field model. It can be shown that the head-to-head or tail-to-tail domain configurations in non-semiconducting ferroelectrics can not maintain their initial state, evolving into a multidomain configuration [7]. For semiconducting ferroelectrics, two kinds of defect systems are studied: ideal and real defect systems. In ideal defect system, for a head-to-head configuration, an electric field is built up in the middle and electrons are accumulated there which compensate the bound charge and make the domain wall conductive. Similarly, for tail-to-tail domain configuration, holes at the domain wall also give rise to domain conductivity.

It can be seen that the head-to-head domain conductivity is not influenced by donor concentration. But the tail-to-tail domain wall does: the higher the donor concentration is, the less conductive the domain wall becomes. Because the more space charge which compensate the

bound charge come from ionized donors, less holes appear at the domain wall. When the concentration of the donors exceed certain value, the domain wall conductivity becomes as low as that of the bulk.

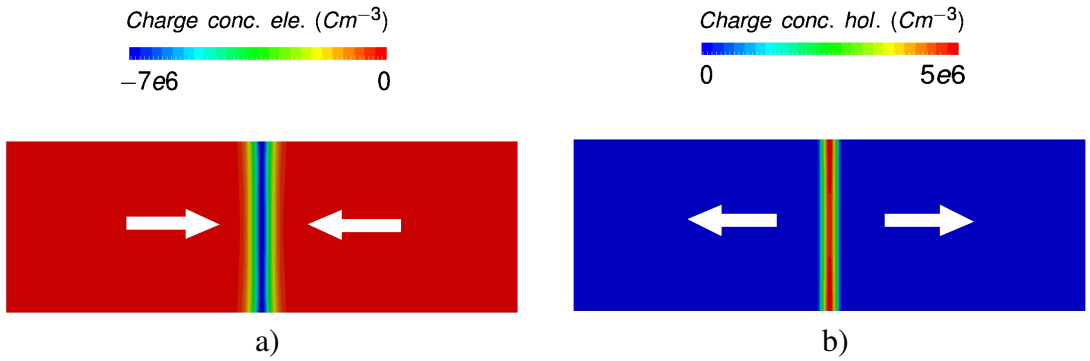

Figure 2: In a ideal defect system: (a) Distribution of space charge from electrons for head-to-head domain configuration. (b) Distribution of space charge from holes for tail-to-tail domain configuration

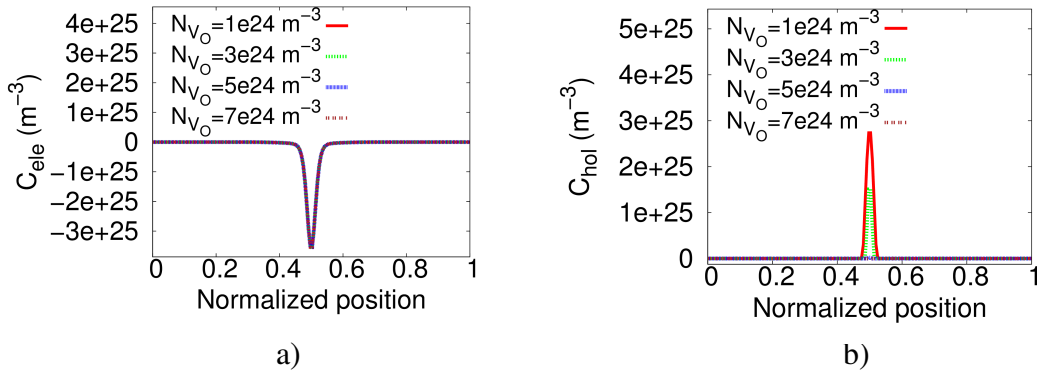

Figure 3: In a ideal defect system: (a) Distribution of space charge from electrons for head-to-head domain configuration. (b) Distribution of space charge from holes for tail-to-tail domain configuration for different oxygen vacancy concentrations

In a realistic defect system, for head-to-head configuration, most of the space charge which compensate the bound charge stems from the electrons for small concentration of manganese-titanium substitutions (0.01mol%). The proportion of compensating charge coming from electrons decreases as the concentration of manganese-titanium substitutions gets larger. The conductivity vanishes as the concentration of Mn-Ti substitutions exceeds certain value. For tail-to-tail domain configuration, the compensation of the bound charge is mostly undertaken by the holes and the ionized oxygen vacancies also make a small contribution. However, the space charge from the ionized oxygen vacancies is smaller than that from the holes by several orders of magnitude. The influence of manganese concentration on the tail-to-tail domain wall concentration is rather insignificant.

It is shown that for different metals used as electrode, the electric potential profile in the sample is merely shifted over the same value as the work function of metals. Therefore the type

of metals as electrode has no influence on the domain wall conductivity.

For the case that the oxygen vacancies are able to diffuse, the simulation show that for head-to-head or tail-to-tail domain configurations, the domain wall conductivity decreases or even vanishes after some time of diffusion.

REFERENCES

[1] M. Y. Gureev, P. Mokry, A. K. Tagantsev, and N. Setter. Ferroelectric charged domain walls in an applied electric field, *Physical Review B*, 86(10): 104104, 2012

[2] M. Y. Gureev, A. K. Tagantsev, and N. Setter. Head-to-head and tail-to-tail 180 degrees domain walls in an isolated ferroelectric, *Physical Review B*, 83(18): 184104, 2011

[3] T. Sluka, A. K. Tagantsev, P. Bednyakov, and N. Setter. Free-electron gas at charged domain walls in insulating BaTiO3, *Nature Communications*, 4: 1808, 2013

[4] D. Meier, J. Seidel, A. Cano, K, Delaney, Y. Kumagai, M. Mostovoy, N. A. Spaldin, R. Ramesh, and M. Fiebig. Anisotropic conductance at improper ferroelectric domain walls, *Nature Materials*, 11(4): 284-288, 2012

[5] S. M. Sze and K. K. Ng. *Physics of Semiconductor Devices*. Wiley, 2007.

[6] P. van Halen and D. L. Pulfrey. Accurate, short series approximations to Fermi-Dirac integrals of order - 1/2, 1/2, 1, 3/2, 2, 5/2, 3, and 7/2,Domain wall stability in ferroelectrics with space charges *Journal of Applied Physics*, 57(12) :5271-5274, 1985

[7] Y. N. Zuo, Y. A. Genenko, A. Klein, P. Stein, and B. X. Xu. Domain wall stability in ferroelectrics with space charges, To be published.

In dieser Schriftenreihe bisher erschienene Berichte:

Nr. 1 (2004) *Ein Modell zur Beschreibung finiter anisotroper elasto-plastischer Deformationen unter Berücksichtigung diskreter Rissausbreitung*, J. Löblein, Dissertation, 2004.

Nr. 2 (2006) *Polyconvex Anisotropic Energies and Modeling of Damage applied to Arterial Walls*, D. Balzani, Dissertation, 2006.

Nr. 3 (2006) *Kontinuumsmechanische Modellierung ferroelektrischer Materialien im Rahmen der Invariatentheorie*, H. Romanowski, Dissertation, 2006.

Nr. 4 (2007) *Mehrskalen-Modellierung polykristalliner Ferroelektrika basierend auf diskreten Orientierungsverteilungsfunktionen*, I. Kurzhöfer, Dissertation, 2007.

Nr. 5 (2007) *Proceedings of the First Seminar on the Mechanics of Multifunctional Materials*, J. Schröder, D.C. Lupascu, D. Balzani (Ed.), Tagungsband, 2007.

Nr. 6 (2008) *Zur Modellierung und Simulation diskreter Rissausbreitungsvorgänge*, O. Hilgert, Dissertation, 2008.

Nr. 7 (2009) *Least-Squares Mixed Finite Elements for Solid Mechanics*, A. Schwarz, Dissertation, 2009.

Nr. 8 (2010) *Design of Polyconvex Energy Functions for All Anisotropy Classes*, V. Ebbing, Dissertation, 2010.

Nr. 9 (2012) *Modeling of Electro-Mechanically Coupled Materials on Multiple Scales*, M.-A. Keip, Dissertation, 2012.

Nr. 10 (2012) *Geometrical Modeling and Numerical Simulation of Heterogeneous Materials*, D. Brands, Dissertation, 2012.

Nr. 11 (2012) *Modeling and simulation of arterial walls with focus on damage and residual stresses*, S. Brinkhues, Dissertation, 2012.

Nr. 12 (2014) *Proceedings of the Second Seminar on the Mechanics of Multifunctional Materials*, J. Schröder, D.C. Lupascu, M.-A. Keip, D. Brands (Ed.), Tagungsband, 2014.